



Universiteit
Leiden
The Netherlands

Optical manipulation and study of single gold nanoparticles in solution

Ruijgrok, P.V.

Citation

Ruijgrok, P. V. (2012, May 10). *Optical manipulation and study of single gold nanoparticles in solution*. *Casimir PhD Series*. Casimir PhD Series, Delft-Leiden. Retrieved from <https://hdl.handle.net/1887/18933>

Version: Corrected Publisher's Version

License: [Licence agreement concerning inclusion of doctoral thesis in the Institutional Repository of the University of Leiden](#)

Downloaded from: <https://hdl.handle.net/1887/18933>

Note: To cite this publication please use the final published version (if applicable).

Cover Page



Universiteit Leiden



The handle <http://hdl.handle.net/1887/18933> holds various files of this Leiden University dissertation.

Author: Ruijgrok, Paul Victor

Title: Optical manipulation and study of single gold nanoparticles in solution

Date: 2012-05-10

Optical manipulation and study of single gold nanoparticles in solution

PROEFSCHRIFT

ter verkrijging van
de graad van Doctor aan de Universiteit Leiden,
op gezag van Rector Magnificus prof. mr. P.F. van der Heijden,
volgens besluit van het College voor Promoties
te verdedigen op donderdag 10 mei 2012
klokke 15.00 uur

door

Paul Victor Ruijgrok
geboren te Ubbergen, Nederland

in 1981

Promotiecommissie:

Promotor:	Prof. Dr. M. A. G. J. Orrit	(Universiteit Leiden)
Copromotor:	Dr. P. Zijlstra	(Universiteit Leiden)
Overige Leden:	Prof. Dr. L. B. Oddershede	(Københavns Universitet)
	Dr. E. J. G. Peterman	(Vrije Universiteit Amsterdam)
	Prof. Dr. E. R. Eliel	(Universiteit Leiden)
	Dr. M. P. van Exter	(Universiteit Leiden)
	Prof. Dr. J. W. M. Frenken	(Universiteit Leiden)
	Prof. Dr. E. J. J. Groenen	(Universiteit Leiden)

The work reported in this thesis was carried out at the 'Leids Instituut voor Onderzoek in de Natuurkunde (LION)' and is part of the research program of the 'Stichting voor Fundamenteel onderzoek der Materie (FOM)'.



An electronic version of this dissertation is available at the Leiden University Repository (<https://openaccess.leidenuniv.nl>)

Casimir PhD Series, Delft-Leiden, 2012-10
ISBN : 978-90-8593-122-5

voor mijn ouders

Contents

Preface	ix
1 Introduction	1
1.1 Nanoparticles: bridging the world between atoms and bulk matter	1
1.2 Why study single metal nanoparticles	4
1.3 Study of a single nanoparticle in solution	6
1.4 Optical manipulation of single gold nanoparticles in a liquid: the use of nanoparticles as a tool	9
1.5 This thesis	12
2 Pushing the detection limits of photothermal microscopy	15
2.1 Introduction	16
2.2 Method	17
2.3 Experimental	20
2.4 Photothermal imaging of gold nanoparticles	22
2.5 Improvements of SNR in photothermal detection of gold NP .	24
2.6 Smallest detectable dissipated power in photothermal detection	27
2.7 Conclusions	28
3 Optical trapping apparatus, and characterization of optical trapping of single gold nanorods	31
3.1 Introduction	31
3.2 Methods and materials	32
3.3 Theory of optical forces and torques on gold nanorods	35
3.4 Thermal stability of trapped nanorods	41
3.5 Gold nanorods align with the trap polarization	43
3.6 Characterization of trapping forces by position fluctuations . .	46

Contents

3.7	Translational and rotational dynamics observed by photon correlation spectroscopy	48
3.8	Conclusions	50
4	Brownian fluctuations and heating of an optically aligned gold nanorod	53
4.1	Introduction	54
4.2	Experimental Methods	55
4.3	Torsional stiffness quantified by the time averaged distribution of orientations	56
4.4	Torsional stiffness quantified by the orientational relaxation time	58
4.5	Temperature dependent dynamics of Brownian fluctuations in the trap	58
4.6	Discussion	61
4.7	Conclusions	61
5	Measuring the temperature of a single metal nanoparticle by changes of the plasmon spectral width	63
5.1	Introduction	63
5.2	Experimental	65
5.3	Modeling of plasmon damping	67
5.4	Results and discussion	69
5.5	Conclusions	75
6	Acoustic vibrations of single gold nanoparticles optically trapped in water	77
6.1	Introduction	78
6.2	Methods	79
6.3	Damping of acoustic vibrations of optically trapped gold nanoparticles	81
6.4	Higher order vibrational modes of gold nanospheres	90
6.5	Vibration modes of gold nanorods	90
6.6	Conclusions	93
7	Conclusions and perspectives	95
7.1	Thesis conclusion	95
7.2	Perspectives	100
	Appendices	103

A Thermal and optical constants for selected materials	105
B Optical microscope	107
C Optical constants of bulk gold	111
D Hydrodynamic friction coefficients	113
E Calculation of the orientational trap stiffness from a measured spectral intensity ratio	117
F Correlation functions in a potential	119
G Heat dissipation of metal spheres and ellipsoids in water	123
H Model of temperature dependent dynamics in the optical trap	127
Bibliography	135
Samenvatting	157
Curriculum Vitae	167
List of Publications	169
Acknowledgments	171

Preface

This thesis reflects four years of research in the MoNOS group at the physics institute in Leiden on the optical trapping of gold nanoparticles, in particular on the use of an optical trap to study single gold nanoparticles in a homogeneous liquid environment.

I started this project with the design and construction of an optical trap, and its integration with the pulsed laser system and confocal microscopy setup already present in the lab, under the guidance of dr. Anna Tchebotareva. During the initial period of construction of the setup we had to wait for new equipment to arrive. We decided to use this time to improve the sensitivity of an optical technique to detect gold nanoparticles. In this technique, a small object that absorbs light can be detected through the refractive effect of the heat that is released in its environment. This technique had been known for many years in analytical chemistry and had been reinvented for single particle detection in far-field optical microscopy by Michel Orrit and colleagues in 2002 in Bordeaux. Since then, the technique had been steadily improved in sensitivity and has been applied in a growing number of applications. Based on recent experiments using photothermal detection in the group in Leiden, we had ideas to significantly improve the signal-to-noise ever further. Our hope was that we could not just detect even smaller gold nanoparticles, but that we would be able to detect single organic dye molecules. With dr. Alexander Gaiduk, we set out to see whether this could be done. After a systematic optimization of every part of the experiment, we managed to obtain the expected improvement in signal-to-noise ratio, as we will describe in detail in Chapter 2. The first experiments on organic molecules were not immediately successful. As the experiment had taken much more time than the originally scheduled two weeks, we decided to stop the experiment on the current setup. Alexander Gaiduk would build a new setup in an adjacent lab, guided by the experience obtained in our experiment. When that setup was

finally in working order –and with the help of the newly arrived PhD student Mustafa Yorulmaz– he could continue the trials on organic molecules and they finally succeeded to detect a single non-fluorescent molecule at room temperature, a challenge that had been open for 20 years.

When all the equipment had finally arrived in working order, we continued work on the optical trap, with the help of the newly arrived dr. Peter Zijlstra. Since there was no experience in optical trapping of metal nanoparticles in Leiden, this was not an easy task. Many days were spent in the lab before we finally realized how we could achieve stable trapping of single nanoparticles. During the struggle to optimize the trap, we developed new methods to characterize particles in the trap, based on our previously gathered expertise on methods to characterize particles immobilized on a substrate. When the optical trap finally worked properly, this provided us with unique possibilities to characterize the trapped particle, as we will describe in Chapter 3. During the construction of the trap, we embraced the opportunity to work on gold nanorods, gold nanoparticles with exciting new possibilities that could be synthesized in the Leiden lab by the expertise brought by Peter Zijlstra. Throughout the remainder of the PhD project, we have used both gold nanospheres and nanorods, taking advantage of their different properties in ways most suitable to the requirements of the various experiments.

With a working optical trap and the methods to characterize trapped particles, we could finally start exploring the properties of the nanoparticle in an homogeneous liquid environment. We decided to study the acoustic vibrations of the gold nanoparticles, as had previously been done in the group for particles immobilized on a glass substrate. This experiment involved a complex pulsed laser setup, and required the co-localization of three or more highly focused optical beams. With the optical trap working properly, and all the experience gained in the process, this turned out to be not too great a challenge. The results of this experiment and the surprising finding about the damping of the acoustic vibration can be found in chapter 6.

Introduction

In this thesis we aim to investigate the optical trapping of gold nanoparticles, both as an approach to study single gold nanoparticles in solution, as well as to explore the use of single gold nanoparticles as a tool for mechanical manipulations on the nanoscale. In this chapter we will motivate the subject and the chosen approach, and outline the contents of the thesis.

1.1 Nanoparticles: bridging the world between atoms and bulk matter

Consider a cube of solid gold with sides of 1 m, and imagine that we cut it into eight equal pieces. Apart from their reduced dimensions, the resulting smaller cubes will have the same intensive properties as the original in every sense: they will have the same elastic moduli, the same heat capacity per unit volume, the same thermal conductivity, the same melting temperature, the same density. If the original cubes looked shiny and yellowish-orange, the smaller cubes look shiny and yellowish-orange as well. You may say that this is obvious: the smaller cubes are still made out of gold, with the intrinsic material properties that belong to it.

However, knowing that matter is made out of atoms, we realize that we can not keep dividing the cubes of gold into smaller and smaller pieces and expect their material properties to remain constant; at some point we will

notice the discrete nature of matter. In this range, material properties will depend on the size and shape of the object, and may become very different from the bulk material properties. Clusters of matter in this size range –roughly 1 nm to 100 nm– are called nanoparticles.

It is one of the big challenges of science today to understand the properties of these nanoparticles as functions of their size and shape. Besides fundamental interest, the progress in this field has many real world applications. An example is the structure of computer chips that have steadily reduced in dimensions since their introduction in the early 1950s. The elements in computer chips are now reaching dimensions where the effects of deviations from bulk matter behavior are becoming important. Besides overcoming technical hurdles to allow the making of ever smaller devices, the study and engineering of nanoparticles and nanostructures allows for an entirely different approach: using the size and shape dependence of the properties to create novel materials with tailor-made functions, opening a wide range of exciting new applications. In recent years, technical developments have made it possible to have an ever increasing control over the size and shape of nanoparticles, and nanostructures of ever increasing complexity are fabricated. The science of nanoscale matter is characterized by a continuing exchange between fundamental insights and the development of new applications. This thesis serves as an example; we will investigate both the intrinsic properties of nanoparticles and their interaction with light, and we will explore the applications that are enabled by these properties.

Optical properties of noble metal nanoparticles

This thesis is about metal nanoparticles, and in particular about their optical properties. Among the various curious material properties of metal nanoparticles, their optical properties take a special place. Gold nanoparticles were already used by the Romans to give a ruby-red color to glass, the most famous example being the Lycurgus cup from the 4th century AD, on display in the British museum in London.¹ The production of gold-ruby glass was rediscovered in Europe only in 17th century by Andreas Cassius and Johann Kunckel.² The fact that the ruby-red color was due to colloidal gold particles was probably not known to either the Romans or the 17th century Europeans, and was only recognized clearly after the first scientific studies on the optical properties of metallic films and colloids by Michael Faraday³ in 1857. The precise mechanism of the coloration was not understood until the beginning of the 20th century, when Gustav Mie developed the general theory to calcu-

late the absorption and scattering of light by spherical particles.^{4-6 †}

The special optical properties of gold nanoparticles are due to the collective oscillation modes of the conduction electrons in the particle, known as localized surface plasmons. Upon excitation by light, the conduction electrons in the metal will collectively shift with respect to the immobile ions. The shift of the electrons with respect to the immobile ions creates a restoring electric field at the particle's surface, that tends to restore electrical neutrality in the particle. Combined with the electron mass, this restoring force leads to harmonic oscillations. For spherical gold particles of sizes below about 100 nm, the resonance occurs at the frequency corresponding to green light for particles embedded in water or glass. Due to the strong absorption and scattering of light at this wavelength, colloidal solutions and glasses with gold particles appear greenish in scattering, and red when observed in transmission.

Because of the resonant character of the oscillation, gold nanoparticles are very efficient scatterers and absorbers of light. This property can be exploited in numerous applications. One example is the use of gold nanoparticles as labels in biological studies, where the nanoparticle is attached to a protein of interest that would be invisible otherwise.⁸⁻¹⁶ An important advantage of metal nanoparticles in these kinds of applications is that they are photostable. Alternative labels as organic fluorophores or semiconductor quantum dots display an erratic on-off switching of their fluorescence known as blinking and eventually photobleach. In contrast, the many electrons in metal nanoparticles never stop interacting with light. The Lycurgus cup may serve as a vivid illustration; after more than two millennia it is still as brightly colored as when it was made. In other applications, the strong absorption of nanoparticles is used to heat the particles, that can then act as a very local heat source. In combination with specific labeling to certain cells, this heating can be used to selectively destroy certain cells, for example in cancer therapy.¹⁷

The restoring force on the electrons – and thereby the plasmon resonance frequency – depends on the material of the particle, on its shape, and the dielectric constant of its environment. The sensitivity of the plasmon resonance to the environment can be exploited to sense the specific binding of molecules that have a different refractive index than the buffer solution, and provides new avenues to detect analytes in very low concentrations or in very small

[†]The solution for scattering of light by a sphere is generally referred to as Mie theory, after Gustav's Mie's seminal work⁴ from 1908. Several important contributions had been made by Thomson, Rayleigh, Lorenz, Love and others, going back to the work of Clebsch in 1863, and an independent derivation has been given by Debye (1909). For a historical overview, see Kerker (1969).⁷

devices.^{18,19} The shape dependence is most clearly presented in nanorods, where the plasmon resonance frequency decreases with increasing particle aspect ratio, and can be shifted from the green all the way to the near infrared. This tunability of the optical properties provides exciting options to tailor the optical properties to the demands of the experiment at hand.

Another property of the localized surface plasmon in particles is that the local electric field at the surface of the particle can be much larger than the electric field of the light exciting the plasmon. This property has various uses. In much the same way as antennas for radio-frequency waves, metal nanostructures can be used as antennas for optical frequency waves, for light. This can be used to enhance the coupling between molecular scale objects and light,²⁰ as has been exploited in surface enhanced Raman scattering.^{21–23} Also the fluorescence of molecules can be modified, and can be either enhanced or quenched^{24–26} or directed,²⁷ depending on the details of the used geometry.

1.2 Why study single metal nanoparticles

In this thesis we study gold nanoparticles with far-field optical microscopy, and focus on experiments on *single* gold nanoparticles. It is important to motivate why we make these restrictions.

Far-field optical studies of metal nanoparticles

A major advantage of optical microscopy is that it can access objects in solid or liquid matrices far away (up to hundreds of microns) from surfaces, with the only restriction that the matrix is (at least partly) transparent at the used wavelength. This opens the possibility of studying nanoparticles live in action in matrices of interest. Relevant examples are biological tissue or cells, or colloidal solutions. With optical microscopy, we can make use of a rich toolbox of time-resolved and frequency-resolved techniques. This thesis itself is an example of the possibilities available; we use powerful infrared continuous wave lasers for optical trapping, broad-band thermal light sources for nanoparticle characterization and ultra-fast wavelength-tunable pulsed lasers for investigation of nanoparticle dynamics on the picosecond timescale.

The biggest disadvantage of far-field optical microscopy is its limited spatial resolution. As with any wave phenomenon we are limited by diffraction, and light can not be focused to a spot smaller than about half its wavelength. For optical studies in the visible region of the electromagnetic spectrum, this limits the spatial resolution to several hundred nanometers. Tech-

niques based on electrons -scanning electron or scanning tunneling microscopy- or atomic forces can achieve much higher spatial resolution, and even resolve single atoms. However, these techniques are much more restrictive in the types of environments that can be studied, and either require vacuum conditions or are restricted to work very close (within nanometers) to the surfaces of materials.

Single particles

During many decades, metal nanoparticles have been studied on large ensembles of particles,^{2,9,28-38} and until today, the bulk of studies on nanoparticles is performed on ensembles.³⁹ The reason that ensemble studies remain a popular choice is that optical studies can reveal a wealth of information, and studies of ensembles can be performed with relatively simple equipment, such as a spectro-photometer present in every (physical)- chemistry laboratory, and with straightforward sample preparation.

Recently, it has become possible to perform studies on single metal nanoparticles. Since the first reports on the detection of single particles about a decade ago,^{8,10,40-42} the field has rapidly developed, expanding the range of particle sizes that can be detected,⁴³⁻⁴⁶ either by scattering, absorption, the generation of new wavelengths by higher harmonics⁴⁷ or fluorescence, and a range of new applications has opened up.⁴⁸⁻⁵¹ While the experimental methods become more challenging, single-particle experiments present several important advantages:

Sample inhomogeneity is suppressed – Even the best synthesis methods yield ensembles with a distribution of particle sizes and shapes. In single-particle studies this inhomogeneity due to the distribution of particle properties in an ensemble is removed, and intrinsic particle properties can be directly observed. Especially valuable is the correlation of several properties on the same particle, and the correlation of the optical properties of the particle to the exact particle morphology by electron microscopy. This is only possible in single-particle studies.

Time dependent fluctuations are accessible – Using single particles, time dependent processes can be studied without the need for synchronization. For ensembles, synchronization is often difficult, or only possible within limits, as particles of different sizes and shapes react differently to a synchronized external perturbation. Another example is

the study of processes that are intrinsically random, such as fluctuating two (or more) level systems. For single particles these fluctuations can be directly observed, whereas in ensembles these fluctuations are averaged out.

Rare configurations can be observed – Particles with rare properties within a sample -or rare configurations of particles- can be studied without the requirement to reliably produce these configurations in large numbers, an often impossible task in the preparation of samples.

Single particle as local reporter or actuator – With single particles, qualitatively new types of experiments are possible. As labels of single entities in cells, they can report not only on their position, but on their three-dimensional trajectories in time. Single particles can become local actuators with optical control, acting either as highly localized sources of heat, or as transducers of force and torque.

1.3 Study of a single nanoparticle in solution

The majority of single particle measurements thus far have met a fundamental limitation: to enable detection of the particle with sufficient signal-to-noise ratio, it had to be immobilized on a solid substrate, such as a microscope coverslip. The underlying reason is that to visualize single particles, typically light has to be focused to a small spot using a high-numerical-aperture objective, and the nanoparticle needs to be immobilized with respect to this tiny focal volume for the duration of the desired experiment. In solution, the nanoparticle will drift away from the focus due to Brownian motion. The time for a nanoparticle to pass the focal volume is on the order of milliseconds (in water), too short for many experiments of interest.

The proximity of the substrate provides a perturbation to the optical, mechanical and thermodynamical properties of the particle. This perturbation complicates modeling of experiments, making it more difficult –or simply impossible– to acquire the desired information. In addition, some experiments inherently take place in solution. For these reasons, it would be highly desirable to perform experiments on single nanoparticles in a homogeneous liquid environment. Some examples of experiments that would benefit from this geometry:

-The particle's plasmon resonance is influenced by the proximity of the substrate, whenever the index of refraction of the substrate differs from that

of the environment. Mie theory^{4,6} qualitatively describes the optical properties of spherical particles embedded in an isotropic medium with an analytical expression, but no such solution exists for a particle on the boundary between two media. Usually the influence of the substrate on the plasmon is simply included as an effective refractive index –the average index of the substrate and the environment. It has not been possible so far to directly measure the influence of the substrate.

-The acoustic vibrations of nanoparticles are influenced by the boundary conditions between the particle and the environment. For a single spherical particle embedded in a homogeneous medium both the frequencies⁵² and damping⁵³ of the vibration modes can be calculated exactly, but a direct experimental test has been lacking. Experiments on ensembles are plagued by the distribution of particle sizes that is inherent to nanoparticles; synchronously launched vibrations quickly get out of phase as particles of different sizes vibrate with different frequencies. The resulting inhomogeneous damping limits the resolution with which the vibration frequencies can be measured and makes it impossible to investigate the loss of vibrational energy to the environment by a measurement of the vibrational damping time. In single-particle measurements the vibrational damping time can be directly accessed. However, here the presence of the substrate provides a perturbation that is very difficult to quantify in experiments. In Chapter 6 we describe our approach to this problem, with a single gold nanoparticle in solution.

Besides these examples, we could think of a whole class of experiments in thermodynamics on the nanoscale, probing heat conduction, nano-bubble formation, particle-reshaping, surface melting, solution based catalysis, etc.

Approach in this thesis: immobilization in solution by optical trapping

In this thesis we achieve the effective immobilization of a single particle in solution, by confining it to the focal volume of a high-numerical-aperture objective with an optical trap. We will discuss the physical principles underlying the trapping in more detail in Section 1.4 and Chapter 3, for now it suffices to say that the optical forces in an intense focused light beam can localize a particle to the focus, enabling the study of single particles in an homogeneous liquid environment. Even though optical trapping of metal nanoparticles was introduced more than 15 years ago and the field has expanded considerably since then (see section 1.4), optical trapping has thus far not been much exploited as a means to study single gold nanoparticles.

1 Introduction

The use of an optical trap has several advantages. In optical trapping no feedback is needed to keep the particle in focus. Once the particle is trapped, it can be followed and studied at leisure for extended periods of time, provided that the trap potential is deep enough. This is an important practical advantage, especially when the complexity of the experiments performed on the particle increases. Furthermore, optical trapping requires no special micro-fluidic devices; any chamber with a liquid between microscope coverslips can be used. Lastly, with the optical trap the particle can be brought from the solution to a substrate to systematically investigate the influence of the substrate.

A further advantage of the optical trap is that it enables a range of other exciting applications for active local manipulation. The ability to locally exert a true force and/or torque on a particle enables applications not accessible with either the passive tracking or trapping by manipulation of solvent flows. We will discuss these possibilities in section 1.4.

Alternative methods for immobilization in solution

In recent years, several methods have been developed that could serve as alternatives to optical trapping as a means to immobilize nanoparticles in solution.

The first possibility is a form of particle tracking.^{54–59} Here, the movement of the particle away from the focus is deduced from an optical signal, for example the light scattered by the particle. This information is inserted in a feedback loop, that moves the complete sample chamber to bring the particle back in the focus (or moves the laser focus back to the particle).

The second possibility is a combination of particle tracking and the use of the feedback signal to induce a flow in a micro-fluidic device to counteract the Brownian motion, a configuration known as the Anti Brownian Motion Electrokinetic trap or ABEL trap.^{60,61} With the ABEL trap, single molecules⁶² and particles down to 1 nm in size⁶³ can be trapped in two dimensions.

A third possibility is geometry-induced electrostatic trapping, where charged objects can be trapped in solution in the vicinity of tailored micro-fluidic slits and pits.⁶⁴ In this method, a spatially modulated electrostatic potential is formed in an ionic solution, by the distribution of charges around the slit. The properties of the trap can be tuned by tuning the ionic strength of the solution, and the precise topography of the slit.

The possibilities above may be complementary methods for the study of single gold nanoparticles in solution. In particular, they may be used to study

particles of sizes too small to be optically trapped. As we shall see, inherent to optical trapping of metal nanoparticles is heating due to absorption of the trapping laser. Single-particle-tracking or the ABEL trap provide avenues to study single particles in solution for experiments when such heating would pose a problem. However, three-dimensional trapping is difficult with the ABEL trap, and the need for a specialized micro-fluidic device restricts its applicability. Both particle tracking and the ABEL trap require a dedicated fast feedback system, with highly optimized optical and electronic components of the setup, adding significantly to the overall complexity of the experiment. The electrostatic trap requires charged particles, trapped in close vicinity (up to several hundred nanometers) of a solid substrate. This restricts its use for thermodynamic and mechanical study of single particles in an homogeneous liquid environment.

1.4 Optical manipulation of single gold nanoparticles in a liquid: the use of nanoparticles as a tool

With control over particle position and the possibility to exert forces on particles, the metal nanoparticle is not only a study object, but it can be used as a tool to manipulate an investigate matter on a nanometer scale.

Optical trapping

Light carries both momentum and angular momentum and can be used to exert forces and torques on matter. For macroscopic objects and the light intensity of most thermal light sources, these forces and torques are so minute that their effects are hardly measurable. For a microscopic particle in an intense laser beam, however, these effects can be substantial, as first realized by Arthur Ashkin.^{65,66} When such a laser beam is strongly focused, these forces can act to localize a particle to the focus, a configuration known as optical tweezers. The ability to exert forces on microscopic particles and manipulate matter on the microscopic scale has been tremendously valuable in physics, biology and chemistry, in a wide variety of applications, ranging from the measurement of the mechanical properties of single (bio-)molecules,⁶⁷⁻⁷⁰ to micro assembly,^{71,72} to nano-surgery.

Most applications to date have used dielectric objects as trapping handles, typically glass or polymer beads, with a size typically one to several micrometers in diameter. Gold nanoparticles can also be trapped, and enable

exciting new possibilities. Due to the higher polarizability of metals, gold nanoparticles can be trapped down to smaller sizes than dielectric objects. The small volume of the particle opens up potential applications of optical manipulation in environments that exclude micron-sized trapping handles. An exciting application would be the optical trapping in living cells, to study the mechanical properties of single bio-molecules in living cells.⁷³

Due to the smaller size, the hydrodynamic friction of nanoparticles is smaller than for micron-sized dielectric particles. This gives rise to shorter relaxation times, and provides access to dynamics of objects attached to the particle on shorter timescales. This holds in particular for rotational motions, for which the friction scales as the particle volume.

Optical trapping of metal nanoparticles

The optical trapping of metal nanoparticle was pioneered by Svoboda and Block in 1994.⁷⁴ Since then, several groups have demonstrated optical trapping of metal nanoparticles. The range of particle sizes that can be trapped has been expanded to particles up to 250 nm in diameter⁷⁵ and down to 10 nm in diameter.⁷⁶ Stable three dimensional optical trapping has been reported for gold^{75,77} and silver⁷⁸ nanospheres, and gold nanorods⁷⁹ with off-resonant trapping with a near-infrared continuous trap laser. Trapping has also been demonstrated using near-resonance geometries,⁸⁰⁻⁸² and with pulsed lasers.⁸³ Also, anisotropic nanoparticles and nanowires have been shown to align -and rotate- with the polarization of the trap laser,⁸⁴ and the optical forces between two trapped particles have been studied,⁸⁵ characterized by their scattering spectra.⁸⁶

However, compared to the rich toolbox of techniques that has been developed for dielectric trapping objects, and the wide variety of applications trapping has been used for, optical trapping of metal nanoparticles is still very much in an early stage,⁸⁷ and many of the unique possible applications of trapping metal nanoparticles are thus far unexplored.

Challenges and open questions in optical trapping of metal nanoparticles

The trapping of metal nanoparticles raises several interesting technical issues and poses new physical questions.

Firstly, a technical issue arises due to the particle volume. Whereas micron-sized dielectric trapping objects have a size comparable to the focal size, or

1.4 *Optical manipulation of single gold nanoparticles in a liquid: the use of nanoparticles as a tool*

larger, metal nanoparticles that can be used for trapping are much smaller in size than the trap focus. The metal nanoparticle may explore inhomogeneities and fine structure in polarization and intensity in the trap focus, that are averaged out for the larger dielectric particle. Methods to detect the motion of the particle in the trap are optimized for particles of a size comparable to the focal volume. Are the same methods still optimal for particles much smaller than the focus?

Secondly, an issue inherent to metal nanoparticles is the absorption of photons of the trapping laser, and the resulting heating.^{77,88,89} For nanoparticles the absorption at a wavelength far off-resonance with the trapping laser can be very small, but it is not zero. Due to the high intensities required for trapping, absorption may be significant. How much light is absorbed? How hot will the particle become? How can we measure the temperature of the nanoparticle in the trap?

Furthermore, the motion of the trapped particle is strictly speaking not Brownian motion. Rather, the hot particle diffuses in an inhomogeneous temperature and viscosity profile.^{90,91} Here the question becomes: can an effective temperature and an effective viscosity be found that describe the motion of the particle subject to the fluctuations of the bath? If so, what are they? More interestingly still, are rotational and translation movements described by the same effective temperature?⁹²

The heating that is inherent to the optical trapping of nanoparticles can be considered a nuisance, or an opportunity. For biophysical experiments, the heating of the nanoparticles is certainly of concern. The health of living cells as a whole is most likely not influenced by a single hot nanoparticle, as the heat is very much localized. Molecules directly attached to the surface of the particle may be more significantly affected. This provides a challenge to the common use of trapped particles as a way to measure the mechanical properties of single (bio-)molecules. This challenge is probably the reason why thus far no single-molecule force measurement using a metal nanoparticle has been reported. However, it is not a priori clear that the challenge of heating is an insurmountable obstacle. For example, one property that may be used to work around this obstacle is that the temperature around the metal nanoparticle falls off rapidly with distance, with a characteristic length scale given by the particle radius. A few radii away from the particle, the temperature is close to the temperature of the bath. If a bio-molecule can be kept at this distance from the particle surface by a heat-resistant spacer that still allows for transduction of forces and torques, it may not be significantly affected. We may also turn around the problem entirely and decide to

use the heating of the particle. Having the ability to control the motions of a hot nanoparticle in space and time, we may envision performing a new type of laser surgery on the nanoscale.

1.5 This thesis

In this thesis, we will address the physics and applications of optical trapping of single gold nanoparticles in solution. We explore this general theme by addressing several inter-related topics in individual chapters: single particle detection, optical manipulation of single particles and study of single-particle properties in solution.

In the topics that will be discussed, one common theme is heat. We will use heat explicitly as a way to detect gold nanoparticles and as a way to excite ultra-fast mechanical vibrations. Wherever heat arises we will try to quantify it, by its effects on the optical properties of the particle or its environment, or on the motions of the particle in solution. A second common theme is (an)isotropy. We will use both spherical and rod-like gold particles when appropriate, and characterize and use their isotropic or anisotropic properties; either optical, thermal or mechanical.

The chapters in this thesis can be read largely independently. To facilitate the reader's choice, we provide here a short description of each chapter, highlighting the main results.

Chapter 2 – A prerequisite to working with single nanoparticles is that you are able to detect them. In this chapter we investigate the detection limits of photothermal microscopy. In this far-field optical detection method absorbing particles are detected by the refractive effects of the heat dissipated into their environment upon illumination. This technique had been shown previously to be able to detect gold nanoparticles of only 67 gold atoms,⁴⁴ a record sensitivity. We show in this chapter how the sensitivity can be pushed even further, enabling the detection of even smaller particles, or smaller amounts of dissipated heat. An important improvement was the realization of how to make optimal use of the optical and thermal properties of the liquid medium surrounding the particle. The achieved improvement in sensitivity of the photothermal method enabled us to detect single non-fluorescent organic dye molecules at room temperature, by the refractive effects of the heat released in their environment upon light absorption. This achievement had been an outstanding challenge since the first far-field

optical detection of single molecules at liquid helium temperatures in 1989.

Chapter 3 – We introduce the optical trapping setup that was built during this thesis. We demonstrate the capabilities of the setup by showing stable three-dimensional trapping of single gold nanorods and perform an experimental characterization of the particles in the trap, with a close look at the thermal stability of the nanorods in the trap, their alignment with respect to the polarization of the trap laser, and the dynamics of their rotational and translational fluctuations in the trap.

Chapter 4 – We quantify the optical torque acting on a single gold nanorod in an optical trap, and show that this torque would be large enough to twist single (bio-)molecules. With the optical force acting on the rod at the same time, the single gold nanorod in the trap could be used as an ultra-small simultaneous transducer of forces and torques. In addition, we quantify the laser-induced heating of the gold nanorod, and we report on the first observation of the combined translational and rotational Brownian motion of a hot object.

Chapter 5 – We study the spectral width of the plasmon resonance of gold nanorods, as a method to measure the temperature of the nanoparticle. We apply the method to the particle in the trap, where the temperature is varied by variation of the trapping power, and for particles immobilized on a substrate, where the temperature of the sample chamber is varied by a known amount.

Chapter 6 – As a demonstration of the advantage of studying single particles in a homogeneous liquid environment, we study the acoustic vibrations of a single gold nanoparticle in the optical trap. With the particles embedded in a homogeneous liquid environment, the damping of acoustic vibration can be directly compared to established theory. Surprisingly, we find that the acoustic vibrations are not only damped by dissipation into the liquid, but damping mechanisms intrinsic to the particle are a significant fraction of the overall damping.

Pushing the detection limits of photothermal microscopy

Abstract – We show how to push the detection limits in photothermal microscopy towards weaker single absorbers, by a systematic optimization of signal and noise sources. In particular, we (i) maximize the power of the probe laser beam, (ii) select optimal optical and thermal properties for the medium embedding the absorber, (iii) thermally isolate the absorber from the glass substrate. These different experimental conditions are optimized in turn with single immobilized gold nanoparticles. We demonstrate the detection of a dissipated power of 3 nW with a signal-to-noise ratio of 8, and an integration time of 10 ms. This corresponds to less than 0.1 K surface temperature rise for a 20 nm-diameter gold nanosphere (0.4 K for 5 nm).

The contents of this chapter are based on:
A. Gaiduk, P. V. Ruijgrok, M. Yorulmaz and M. Orrit, “Detection limits in photothermal microscopy”, *Chem. Sci.* **1**, 343-350 (2010)

2.1 Introduction

Photo-thermal, photo-acoustic and photo-optical (photo-refractive and photo-chromic) effects are widely used in physics, analytical chemistry and medicine.⁹³ Photothermal spectroscopy is a two-color nonlinear optical technique, in which a heating (pump) beam is absorbed by the species to be detected, causing heat release and a local change of refractive index. The propagation of a second beam at a different wavelength, the probe, will thus be modified by the produced heat. These changes produce the observed signal.⁹⁴ Photothermal spectroscopy provides a number of ultra-sensitive methods to measure optical absorbance and estimate concentrations of nanometer-sized particles and non-fluorescent molecules in solvents.^{41,95} Photothermal detection has two main advantages. First, the signal is free from background and not sensitive to weak scattering, because the signal only arises from absorbing centers that dissipate heat. Second, because the probe only reacts to refractive index changes, the probe wavelength can be chosen outside of the absorption range of the centers. Therefore, the probe power can be increased to very high values, for which photon noise in the probe detection may become extremely small. The maximum probe power applicable is ultimately limited by sample damage.

Recent developments based on the combination of photothermal effects and interferometric detection have opened up absorption properties of individual labels to optical detection with a high signal-to-noise ratio. Such absorbing labels do not need to fluoresce and have been small (< 40 nm diameter) noble metal nanoparticles, quantum dots, or single-walled carbon nanotubes.^{43,44,96–101} In contrast to the organic molecules used in fluorescence detection, these labels generally show neither photobleaching nor photoblinking, which makes them attractive for many applications, such as DNA microarrays,¹⁰² gold-labeled protein detection in cells,¹⁰³ optical tracking in live cells¹⁰⁴ and high-throughput screening.¹⁰⁵

Recently, the dynamic range of photothermal microscopy experiments has expanded and new applications have been suggested. Photothermal correlation spectroscopy has been proposed to study the diffusion of single gold nanoparticles in fluid media, and was demonstrated with protein-gold complexes and gold-labeled bacteriophage viruses.^{106–108} The selectivity and sensitivity of photothermal detection was demonstrated for direct imaging of mitochondria in live cells, without need for any labeling.¹⁰⁹ The origin of the photothermal contrast of mitochondria is still not well understood, for the abundant inter-membrane protein cytochrome c was excluded as the source

of the photothermal signal. The anisotropic absorption properties of small (25×75 nm) gold nanorods have been probed with polarization-sensitive photothermal microscopy.¹¹⁰ The authors of that work propose to use plasmon resonances of rods to probe orientation and dynamics of macromolecules in highly scattering environments. A photothermal excitation combined with digital heterodyne holography¹¹¹ provides wide-field (up to $100 \mu\text{m}^2$ area) photothermal detection of 50 nm and smaller gold particles. The method involves a trade-off between large observation areas, video rate acquisition speed, and a large radius of heat diffusion.¹¹² Compared to single-point detection, the signal-to-noise of wide-field detection is about an order of magnitude lower.

To further expand the performance and applications of single-point photothermal detection, it is important to look for its detection limits. To our knowledge, the best signal-to-noise ratio measured in single-point photothermal detection⁹⁷ was about 10 for a 5 nm gold nanoparticle (NP) heated with a power of $500 \mu\text{W}$ (514 nm), with unspecified probe power, and with an integration time of 10 ms.[†] We estimate the absorbed power in these experiments to 20 nW. It is important to know how far this result is from the theoretical limit.^{100,106} In the several publications following this early work, little attention has been paid to the various factors which may influence the signal-to-noise ratio in photothermal detection.

In this Chapter, we examine how the probe power, the thermal properties of the medium, and thermal isolation of the absorber from the glass substrate influence the signal-to-noise ratio in photothermal detection.

2.2 Method

Photothermal detection is sensitive to the amount of energy absorbed by a nanoobject and dissipated as heat into its local environment. We define as the dissipated power P_{diss} the power provided by a heating beam (with power P_{heat}), which is dissipated as heat by the absorber. Because the heating beam intensity is modulated at an angular frequency Ω , we call P_{diss} the maximum instantaneous value of this power during the modulation period. The time-averaged dissipated power is therefore $P_{\text{diss}}/2$. For a spherical gold particle

[†]The same group reported detection of gold NP as small as 1.4 nm (67 atoms) with a signal-to-noise ratio of about 10, achieved with integration of 10 ms and a temperature rise of ~ 2 K.⁴⁴ However, some of the parameters of the experiment are unspecified. Our calculation of the dissipated power for these particles in these conditions is 4 nW

2 Pushing the detection limits of photothermal microscopy

of radius R placed in a homogeneous medium with thermal conductivity κ , the maximum temperature increase $\Delta T(r, t) = \Delta T_{\text{surf}}$ scales as R^2 , because the cross-section σ_{abs} scales as R^3 .^{6,49,113} The thermal radius $r_{\text{th}} = \sqrt{2\kappa/\Omega C_p}$ is the characteristic length of heat diffusion in the medium, where C_p is the heat capacity per unit volume of the photothermal medium. Dissipation of the absorbed energy into the medium results in a temperature profile $\Delta T(r, t)$, which in steady conditions with sinusoidal modulation is given by:⁴³

$$\Delta T(r, t) = \frac{P_{\text{diss}}}{4\pi\kappa r} [1 + \exp(-r/r_{\text{th}}) \cos(\Omega t - r/r_{\text{th}})] \quad (2.1)$$

Assuming the response to be instantaneous, this temperature profile in turn causes a refractive index profile $\Delta n(r, t) = \Delta T(r, t) \partial n / \partial T$ in the medium, acting as a modulated thermal nanolens.⁹⁴ A probe beam is used to detect that nanolens. In the usual photothermal geometry^{44,94,95} the scattered probe field $E_{\text{sc}}(t)$ interferes with a reference probe field E_{ref} (usually the transmitted beam or a reflection), and the resulting intensity $I_{\text{det}} \propto |\vec{E}_{\text{ref}} + \vec{E}_{\text{sc}}|^2$ is detected. In this discussion, we neglect the difference in spatial modes of the two fields, which are supposed to be similar. The lock-in amplifier filters out the weak contribution to the interference signal $2\text{Re}[E_{\text{ref}}^* E_{\text{sc}}]$ modulated at the same frequency as the heating beam. The contribution of the modulated scattered intensity $|\vec{E}_{\text{sc}}|^2$ is neglected for small particles (typically < 60 nm diameter).⁴⁹ For larger particles, a non-negligible static scattered field acts as an additional in-phase reference field. Its contribution to the interference intensity I_{det} is reported in photothermal correlation spectroscopy experiments for 80 nm diameter gold particles.¹⁰⁶ The photothermal signal S is proportional to the field scattered by an effective volume V where the refractive index is modulated. The refractive index change Δn depends on the absorption cross-section σ_{abs} of the nanoobject and the heating beam with intensity I_{heat} focused into a diffraction-limited spot with area A . Δn is proportional to the power dissipated by the nanoobject $P_{\text{diss}} = I_{\text{heat}} \sigma_{\text{abs}} = \sigma_{\text{abs}} P_{\text{heat}} / A$. The field scattered by the thermal lens can be approximated by that of an equivalent dipole $|\vec{p}| \approx 2n \Delta n \cdot V |\vec{E}_{\text{probe}}|$, where $\Delta n \cdot V$ stands for the volume integral of the position-dependent refractive index change of the lens. The scattered field is radiated by this dipole: $|\vec{E}_{\text{sc}}(t)| \approx |\vec{p}| / (4\pi\epsilon_0\omega_0\lambda^2)$, and the photothermal signal can then be written as an optical power:

$$S \approx \frac{1}{\pi\omega_0} n \frac{\partial n}{\partial T} \frac{1}{C_p \lambda^2 \Omega} \frac{\sigma_{\text{abs}}}{A} P_{\text{heat}} P_{\text{probe}} \Delta t \quad (2.2)$$

where ω_0 is the probe beam focal radius (beam waist), λ and P_{probe} are the wavelength and power of the probe beam, and Δt is the integration time of

the lock-in amplifier. We assume the thermal conductivity of metal nanoparticles to be much larger than that of the surrounding media (for example, $\kappa_{\text{gold}} = 310 \text{ W m}^{-1} \text{ K}^{-1}$, $\kappa_{\text{water}} = 0.6 \text{ W m}^{-1} \text{ K}^{-1}$).

The noise in actual experiments arises from the detector, from fluctuations of the probe laser power, and from photon noise of the detected optical power. In practice, the experimental noise is always larger than the photon noise, but can be close to it for an optimized setup. Here, assuming an ideal detector and a shot-noise limited detection, the noise on the photothermal signal N would be:

$$N \propto \sqrt{\frac{P_{\text{probe}} \Delta t}{h\nu}} \quad (2.3)$$

where h is Plank's constant and ν is the frequency of the probe light. Combining the expressions for the signal and the noise, we see that the signal-to-noise ratio SNR for the shot-noise-limited photothermal detection is given by:

$$SNR \approx \frac{1}{\pi\omega_0\lambda^2\Omega} n \frac{\partial n}{\partial T} \frac{1}{C_p} \frac{\sigma_{\text{abs}}}{A} P_{\text{heat}} \sqrt{\frac{P_{\text{probe}} \Delta t}{h\nu}} \quad (2.4)$$

We now discuss how the SNR can be optimized by tuning all factors in Eq. 2.4, and the practical limits to optimization.

1. Increase the dissipated power up to the allowed maximum, usually fixed by saturation. For gold nanoparticles, the applicable powers are very high (the bulk melting temperature of gold is about 1300 K, and the temperature rise to reshape gold nanorods, although significantly lower^{114,115} is still some hundreds of K). The allowed temperatures in biological samples, however, will be much lower. The melting intensity for a spherical particle with diameter 20 nm in water is around 20 MW/cm^2 at 514 nm (about 20 mW focused on a spot), and scales with R^2 . For a non-fluorescent molecule, the saturation intensity is determined mostly by the excited state lifetime τ , typically 0.1 ns, which leads to a dissipated power of a few nW.
2. Increase P_{probe} as much as possible. Practical limits are set by the maximum available laser power and by residual absorption of the probe beam by the sample. For example, the probe power can be increased until the probe-induced and pump-induced heating are comparable. For small gold NPs in glycerol, for example, we can use up to 170 times more probe power at 800 nm than heating power at 532 nm, as given by the ratio of the absorption cross-sections.

2 Pushing the detection limits of photothermal microscopy

3. Match the heat diffusion length r_{th} with the spot size, by choosing the right modulation frequency Ω .^{43,100} A lower modulation frequency generally leads to a higher photothermal signal, until the thermal lens exceeds the size of the focused probe beam. The optimal value of the modulation frequency also depends on the experimental noise spectrum.
4. Optimize the optical and thermal properties of the photothermal medium, including refractive index, its derivative with respect to temperature, heat capacity and conductivity (see Section 2.5.2 and Appendix A).
5. Increase the integration time of the lock-in amplifier. This parameter can be increased arbitrarily, provided the mechanical stability of the experimental setup and the photostability of a sample allow it.

2.3 Experimental

2.3.1 Sample preparation

Samples of gold colloids with diameters of 5 nm and 20 nm (British Biocell International, EM.GC5 and EM.GC20) were prepared by dilution in ultra-pure water at the ratios of 1:40 and 1:8, respectively. Approximately 50 μL of the suspension were deposited on the surface immediately after the filtration through a 450 nm porous membrane and spin coated at 2000 rpm for 5 s, followed by drying at 4000 rpm for 90 sec. Glass coverslides (Menzel, Germany) were cleaned by sonication for 20 min in the following solvents: 2 % Hellmanex (Hellma) solution in water, acetone (96% purity), ethanol (96% purity). Additional sonication in water was performed prior to each cleaning step. The glass coverslides were then dried and treated in a UV-ozone cleaner for at least 30 min prior to following sample preparation steps. PMMA, poly(methyl-methacrylate) with $M_W = 96.7$ kDa (Sigma-Aldrich) was used to prepare a thermal isolation layer on top of clean substrates. About 50 μL of PMMA solution in toluene at 30 g/L concentration was spin coated. The thickness of the resulting PMMA layer was measured by AFM and found to be 100-120 nm. For preparation of nanoparticles (NP) on PMMA, a 2 % PVA solution (polyvinyl alcohol, $M_W = 130$ kDa, Fluka) in water was mixed with NPs to provide the desired concentrations of gold colloids and 1 % concentration of PVA. The sample was prepared via spin coating, resulting in PVA layer thickness of approximately 20 nm. The thin PVA film was found

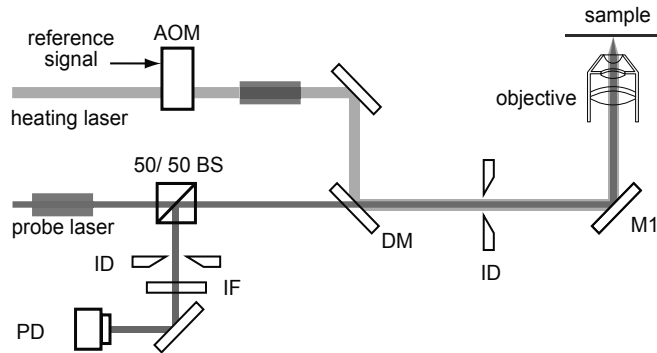


Figure 2.1: Scheme of the experimental setup for simultaneous photothermal and fluorescence detection. The heating light for photothermal microscopy also excites fluorescence at the same time. AOM - acousto-optical modulator, M - mirror, BS - beam splitter, DM - dichroic mirror, ID - iris diaphragm, IF - interference filters, APD - avalanche photodiode, PD - photodiode. Polarizer, spatial filters are not shown in this scheme. Grey boxes schematically indicate the positions of the telescopes and beam expander.

to be dissolved after several hours in glycerol. NPs remain adsorbed on the PMMA surface. The measurements were performed in a fluid cell with $\sim 50 \mu\text{L}$ photothermal medium. The cell was assembled from two glass coverslips and a rubber o-ring attached to the bottom one. Clean glycerol ($>99.5\%$, spectrophotometric grade), ethanol (spectroscopy grade), chloroform (spectroscopy grade), dichloromethane, pentane, and hexane (all AR grade) were used as photothermal media.

2.3.2 Photothermal detection setup

The experimental setup is based on a home-built microscope equipped with an Olympus $60\times$ oil immersion objective ($\text{NA} = 1.4$ or $\text{NA} = 1.45$) and is sketched in Fig. 2.1. The heating beam is provided by either a laser diode at 532 nm (Shanghai Lasers, power 150 mW) or by an Ar-ion laser (Coherent, max. output 10 W). The heating light passes an acousto-optical modulator (AOM) which is operated typically at $\Omega = 740 \text{ kHz}$. The beam is expanded in a spatial filter (60 mm and 100 mm lenses, with a $30 \mu\text{m}$ pinhole,) and a telescope (100 mm and 200 mm) to about 20 mm , and overfills the entrance pupil of the microscope objective (approximately 10 mm). The expanded beam is sent towards the microscope objective by a dichroic mirror (BS 669, AHF) on which heating and probe beams are combined. The probe beam at 790 nm

or 800 nm is provided by a Ti:sapphire laser (either Mira, Coherent, pumped with Coherent Verdi V10; or Spectra Physics, 3900 S, pumped by 90% of the power of the Ar-ion laser). The near-infrared light (NIR) passes a polarizer and a spatial filter (two 75 mm lenses with a 30 μm pinhole). A variable beam expander 2-5 \times provides the continuous adjustment of the diameter of the probe light to ensure the optimal overfilling of the objective lens with the desired probe power. A 50/50 beam splitter (Halle) is used to reflect half the power of the probe laser to the microscope and transmit half the back-scattered probe light towards the detector. The spectrally filtered probe light is focused with a 100 mm lens onto a photodiode (Femto DHPKA-100-F, Germany) or optionally monitored by a CCD camera (Ganz, Germany). A wave generator (33250A, Agilent) provides the modulation signal for the AOM and the reference of the lock-in amplifier (SR844, Stanford Research Systems) analyzing the photodiode output. All data acquisition and processing is performed by an acquisition card (ADWin Gold, Germany) linked to a computer. The sample is scanned with a 3-axis piezostage (NanoCube, Physik Instrumente).

2.4 Photothermal imaging of gold nanoparticles

We first demonstrate the performance of our setup with photothermal microscopy on 5 nm and 20 nm diameter gold nanoparticles. A photothermal microscopy image (Fig. 2.2 A) shows about 30 particles with 20 nm diameter (density $<1 \text{ NP}/\mu\text{m}^2$) and 3 particles with 5 nm diameter (density $<0.1 \text{ NP}/\mu\text{m}^2$). Cross-sections of the spots of some 20 nm NP and of the 5 nm NP indicate an intensity ratio of 35, not too far from the expected ratio $(20/5)^3 = 64$ (Fig. 2.2 B). The difference is explained by deviations from the nominal average NP diameter provided by the manufacturer. Indeed, we found by AFM and SEM that the diameters of the nominal 20 nm NPs varied between 14 nm and 18 nm. Moreover, some particles, for example triangles, were found to deviate significantly from the spherical shape. The results of the photothermal imaging and SNR analysis of 73 particles of 20 nm and 119 particles of 5 nm are presented in Fig. 2.2 C and summarized in Table 2.1.

We detect 20 nm NPs with a SNR of 420 and an integration time of 1 ms with 260 μW of heating power and 20 mW of probing power at the sample's position. These values correspond to 810 nW of dissipated heating power and to 170 nW of dissipated probe power. The total power absorbed corresponds to a temperature rise of about 28 K at the surface of a 20 nm NP. A SNR of

2.4 Photothermal imaging of gold nanoparticles

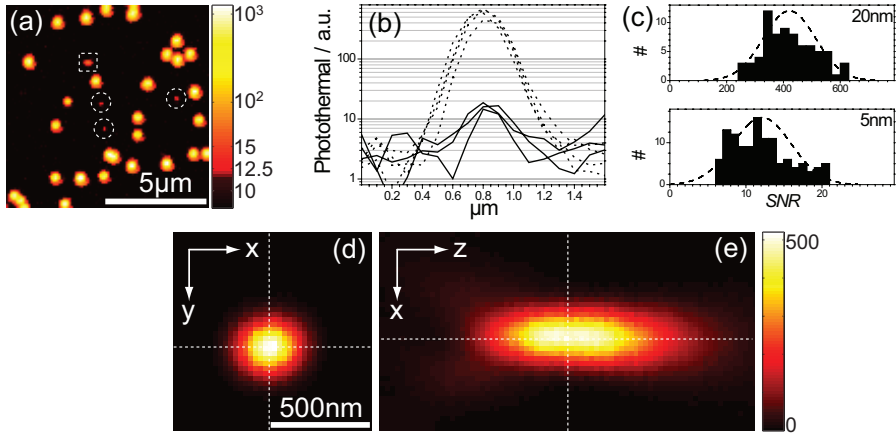


Figure 2.2: a) Photothermal microscopy image of a sample with gold nanoparticles of 20 nm and 5 nm diameter immobilized on a glass slide in glycerol. The photothermal signal is color-coded on a logarithmic scale. Circles mark the positions of 5 nm NPs. The NP in the square box may be an aggregate. $P_{\text{heat}} = 0.26 \text{ mW}$, $P_{\text{probe}} = 20 \text{ mW}$, $\Delta t = 1 \text{ ms}$, $T_{\text{surf}} \sim 28 \text{ K}$. (b) Several cross-sections of 20 nm (dashed lines) and 5 nm (solid lines) NP along the slow scan axis (horizontal in the image) present relative signals for particles of different sizes. (c) Histograms of the photothermal SNRs for gold NP of 20 nm (top, 73 NP) and 5 nm (bottom, 119 NP). The population of 5 nm particles has $SNR = 12 \pm 4$, while the population of 20 nm particles has $SNR = 421 \pm 92$. Experimental data are presented in histograms. (d) Photothermal image of a single 20 nm gold colloid. (e) Photothermal image of a single 20 nm gold NP taken along the vertical z-axis, perpendicular to the glass surface. Gaussian fits of the shape of the signal along the z-, y- and x-axes gives FWHM values of 730 nm, 250 nm, and 220 nm, respectively. Vertical dashed lines indicate the position of the glass-glycerol interface (glass on the right-hand side).

12 is achieved with the same integration time, heating, and probe powers for 5 nm NPs. For the 5 nm particles, the dissipated powers are 12.6 nW for the heating beam and 2.6 nW for the probing beam, and the respective surface temperature rise about 0.5 K. The spatial overlap of heat and probe beam in photothermal microscopy provides optical sectioning and defines the spatial resolution. The photothermal detection volume is defined by the product of the point spread functions of heating and probe beams. By focusing both beams into overlapped diffraction-limited spots, we achieve a lateral spatial resolution of about 240 nm, and an axial resolution of 730 nm (Fig. 2.2 D,C).

Table 2.1: Experimentally obtained signal-to-noise ratios (SNR) in photothermal detection of gold nanoparticles on glass in glycerol ^a

Diameter	$P_{\text{diss}}^{\text{pump}}$ (nW)	$P_{\text{diss}}^{\text{probe}}$ (nW)	$\Delta T_{\text{surf}}^{\text{pump}}$ (K)	$\Delta T_{\text{surf}}^{\text{probe}}$ (K)	SNR
20 nm	810	170	23	4.8	421
5 nm	12.6	2.6	0.4	0.08	12

^a Heating with 532 nm ($I_{\text{heat}} = 130 \text{ kW cm}^{-2}$), probing with 790 nm ($I_{\text{probe}} = 4.5 \text{ MW cm}^{-2}$). Integration time Δt is 1 ms. $P_{\text{diss}}^{\text{pump}}$ ($P_{\text{diss}}^{\text{probe}}$) and $\Delta T_{\text{surf}}^{\text{pump}}$ ($\Delta T_{\text{surf}}^{\text{probe}}$) are the dissipated power due to the pump (probe) laser and the corresponding particle surface temperature, respectively.

2.5 Improvements of SNR in photothermal detection of gold NP

Hereafter, we discuss several possible ways to increase the photothermal SNR, and verify them experimentally with 20 nm gold NPs.

2.5.1 Reduce photon noise with higher probe powers

As follows from Eq. 2.4, the SNR in ideal photothermal experiments should be proportional to the square root of the probe power. The measurements of SNR are presented in Fig. 2.3 A. The good agreement with the expected power law (Eq. 2.4) indicates that the noise in our photothermal detection is mainly determined by photon noise. In particular, for the range of probe powers detected in our experiments, laser noise is negligible. At low probe powers, the SNR deviates from the square-root dependence because of detector noise, which is independent of power. To achieve maximum sensitivity in the photothermal detection, we want to keep the photodetector gain maximal. This gain is limited by the total power reaching the detector. Apart from its weak time-dependent component encoding the photothermal signal, the detected probe power has a strong static contribution, which arises from reflection by the glass-liquid interface. The reflected power, determined by the refractive index mismatch between the BK7 glass ($n = 1.52$) and the medium, varies from $4.4 \cdot 10^{-3}$ for the glass-water ($n = 1.33$) to $2.5 \cdot 10^{-4}$ for the glass-glycerol ($n = 1.473$) interfaces, as given by Fresnel's equations for normal incidence. We chose a maximum detected probe power of $18 \mu\text{W}$, corresponding to a gain of 10^5 A/V , which is a trade-off between high probe power and low photodetector noise. Then, the maximal incident probe power varies from

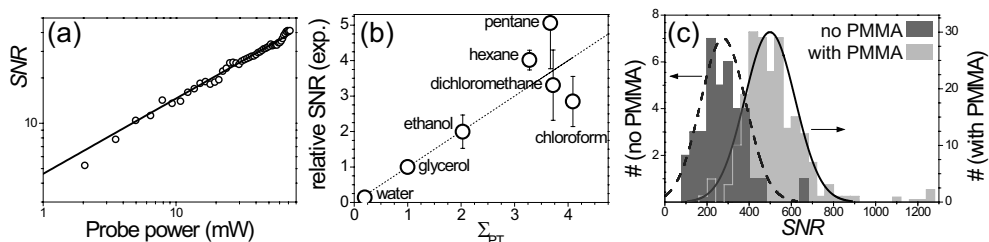


Figure 2.3: (a) Photothermal signal-to-noise ratio as a function of the incident probe power ($\lambda = 790$ nm) measured for 20 nm gold NPs in water on glass. The fit shows the square root dependency of the SNR. (b) Photothermal SNR measured for 20 nm NPs in different fluids as a function of calculated photothermal strength for these fluids Σ_{PT} , scaled with respect to glycerol. Measurements were done on a few NPs in water, 116 NPs in glycerol, 92 NPs in ethanol, 60 NPs in dichloromethane, 41 NPs in hexane, 63 NPs in chloroform and 30 NPs in pentane. The error bars give the standard deviation of the distribution. (c) Normalized histograms of SNR for 20 nm gold NP in glycerol: (dark grey) deposited on glass, $SNR = 272 \pm 110$ over 38 particles; (light grey) deposited on a 100 nm thick thermal isolation layer of PMMA, $SNR = 502 \pm 128$ over 211 particles. Among them, 6 particles show SNR values twice the mean distribution value (>1000) indicating a few aggregates ($<3\%$) in the area of $1000 \mu\text{m}^2$. Experimental parameters: heating with 0.27 mW incident power at 514 nm, probe at 800 nm with 23 mW incident power, corresponding to a total $T_{\text{surf}} \sim 28$ K (due to heat and probe), integration time 3 ms

4 mW for water to 72 mW for glycerol. Note that achieving photon-noise limited detection in the forward direction is more difficult than in the backward direction for two reasons. First, it is difficult to find fast and sensitive detectors for powers larger than 20 mW. Second, photon-noise limited detection of higher powers requires a lower laser noise.

2.5.2 Solvent

As has been known for many years, the thermal properties of the solvent are crucial for photothermal spectroscopy and its applications to analytical chemistry.⁹⁴ An obvious step to enhance the photothermal signal is to select a solvent with a high sensitivity of its refractive index to a temperature change, ($\partial n / \partial T$). Note, however, that this (usually negative) quantity is only a crude figure of merit characterization of the heating-induced change of refraction for small enough temperature raises. To account for the full space- and time-dependent changes of refractions around the heated object, the full

function $n(r, T)$ should be considered. In addition to its optical properties, the thermal properties of a medium determine the magnitude of the photothermal signal. We selected several organic fluids based on their expected value for a parameter we call 'photothermal strength' (See Appendix A):

$$\Sigma_{\text{PT}} = n \left| \frac{\partial n}{\partial T} \right| \frac{1}{C_p}. \quad (2.5)$$

This parameter characterizes the refractive index change that is produced by a given energy density (heat/unit volume) stored in the photothermal medium. However, because the thermal radius r_{th} must be fixed in relation to the probe wavelength, it may be more physical to define an alternative figure of merit of photothermal media *FOM*:

$$\text{FOM} = n \left| \frac{\partial n}{\partial T} \frac{1}{\kappa} \right|, \quad (2.6)$$

which is equivalent to $\Sigma_{\text{PT}}/r_{\text{th}}^2$. These two characterizations do not differ much in their predictions for selected fluids. We have measured the photothermal signals of 20 nm NPs in equivalent conditions. The results are presented in Fig. 2.3 B and correlated with the expected photothermal strength Σ_{PT} . The agreement with the expected signal is only approximate for the highest photothermal strengths. As indicated, the SNR can be improved by up to 5 times by performing experiments in pentane, as compared to glycerol. Glycerol itself gives 5 times higher SNR than water at 20 °C. Clearly, fluid media with a large sensitivity of their refractive index to temperature (large thermal expansion coefficients) will be interesting for photothermal detection. These are fluids close to their critical points or to phase transitions, as well as mixtures close to demixing points, presenting a large Soret effect. However, the temporal response of a medium is slowed down dramatically close to a critical point, and the sensitivity only appears in a small temperature range close to the critical point. For strong heating, the enhancement of the refractive response would be essentially destroyed by averaging over space and time.

2.5.3 Thermal isolation

The thermal conductivity of glass ($1.05 \text{ W m}^{-1} \text{ K}^{-1}$) is more than 3 times larger than that of most organic liquids ($0.28 \text{ W m}^{-1} \text{ K}^{-1}$ for glycerol). Therefore, a large part of the generated heat will be lost to glass, where the associated

refractive index change is very small. The thermal conductivity of the glass support, which acts as a heat sink, thus reduces the photothermal effect. A thermal isolation layer introduced between the absorber and its solid substrate will reduce the 'leak' of heat into the glass. We chose to prepare a thin PMMA film (heat conductivity $0.2 \text{ W m}^{-1} \text{ K}^{-1}$) on the top of glass substrate prior to gold NP deposition. The film deposited via spin coating was found by AFM measurements to have a homogeneous thickness of 100-120 nm. An alternative way to achieve thermal isolation is to use a PMMA substrate, however available substrates have poor optical quality and are too thick compared to the working distance of high NA microscope objectives. A comparison of photothermal SNR for 20 nm gold particles on glass and on PMMA on glass, both in glycerol, is shown in Fig. 2.3 C. We demonstrate a signal increase by 1.8 times in the presence of the thermal isolation layer, as measured on 38 NPs on glass and 211 NPs on PMMA on glass. This number is smaller than 4, the expected ratio of heat leaks based on the assumption of a perfect isolation. Heat diffusion simulations in this complex geometry would be needed for a more quantitative comparison.

2.6 Smallest detectable dissipated power in photothermal detection

To compare the efficiencies of photothermal detection of different point-like objects in different conditions, it is sufficient to compare the powers P_{diss} they dissipate in their environment. In the following, we probe the limits of photothermal detection in experiments with 20 nm gold NPs in glycerol, which serve as test objects with a well-defined absorption cross-section. We experimentally estimate the smallest P_{diss} and temperature rise T_{surf} which we can detect with a reasonable SNR. Typical results for the photothermal detection of dissipated powers down to 2.6 nW on glass and in glycerol are demonstrated in Fig. 2.4. Here, heating powers of $9 \mu\text{W}$ (Fig. 2.4 A) and $1 \mu\text{W}$ (Fig. 2.4 B) at 514 nm were used. The dissipated powers were 24 nW (Fig. 2.4 A) and 2.6 nW (Fig. 2.4 B) corresponding to temperature rises of 0.7 K (A) and 80 mK (B). These are detected with an average $\text{SNR} = 20$, with a 3 ms integration time (Fig 2.4 A), and $\text{SNR} = 8$, with a 10 ms integration time (Fig 2.4 B).

According to our previous discussion, there are several ways to increase the SNR compared to Fig. 2.4. We can win a factor of 2 by increasing P_{probe} from 68 mW to 280 mW. Another factor of 10 can be gained by increasing the

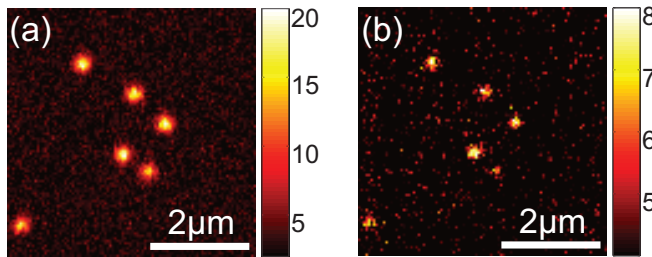


Figure 2.4: Photothermal images of 20 nm gold NPs in glycerol with (a) $P_{\text{heat}} = 9 \mu\text{W}$, $P_{\text{probe}} = 23 \text{ mW}$, $\Delta t = 3 \text{ ms}$, and with (b) $P_{\text{heat}} = 1 \mu\text{W}$, $P_{\text{probe}} = 68 \text{ mW}$, $\Delta t = 3 \text{ ms}$. Dissipated powers (P_{diss}) and temperature rises (T_{surf}) are 24 nW and 2.6 nW, and 0.7 K and 80 mK, with average SNR of 20 and 8, respectively. Heating and probing wavelengths 514 nm and 800 nm.

integration time of the lock-in amplifier (Δt) from 10 ms to 1 s. A further enhancement factor of 5 can be gained with a better photothermal medium (pentane instead of glycerol), and one of about 2 with thermal isolation of the particle from the substrate (with PMMA layer). Overall, the SNR can be increased by a factor of 200. Thus, with the achieved sensitivity and proposed experimental conditions we would be able to detect dissipated powers lower than 15 pW within 1 s, with a SNR of 8.

2.7 Conclusions

We have proposed several ways to increase the signal-to-noise in photothermal detection. We demonstrate that (i) our SNR is very close to limited by photon noise, in particular laser noise is negligible, (ii) the choice of photothermal medium is very important to achieve a high sensitivity (e.g., pentane gives a 5 times higher signal than glycerol), (iii) a significant signal increase can be achieved by introducing a thin layer of polymer between the glass substrate and the photothermal medium (here, 100 nm of PMMA led to an improvement of the signal by a factor of about 2). The sensitivity of photothermal detection can further be improved by (i) better focusing of the heat and probe beams (for example using radially polarized light¹¹⁶ or immersion in higher indices¹¹⁷); (ii) using a photothermal medium with even larger refractive index changes with temperature, for example fluids close to phase transitions. Furthermore, we have demonstrated the photothermal detection of 3 nW of dissipated power with a $SNR \sim 8$ in 10 ms.

Acknowledgments

We thank Anna Pezzarossa and Prof. Thomas Schmidt for help with wide-field fluorescence microscope, BioAFM lab for providing access to AFM, and Peter Zijlstra for SEM images of gold NP.

3

Optical trapping apparatus, and characterization of optical trapping of single gold nanorods

3.1 Introduction

In this chapter we discuss the optical trapping apparatus that was built during this project. We demonstrate the capabilities of the setup by a detailed characterization of the optical trapping of single gold nanorods. We will discuss the experimental methods used to characterize the optical trap, to characterize the trapping of a single particle as well as detect the presence of multiple particles in the trap. We record the white-light scattering spectrum of each individual trapped rod to measure its aspect ratio, and study the thermal stability of the rods. We show that the nanorods align with the polarization of the trap laser by measuring the polarization and spectrum of the scattering light. Using scattering correlation spectroscopy we record both the translational and rotational fluctuations of the trapped rod to characterize the orientational and translational trap stiffnesses.

3 Optical trapping apparatus, and characterization of optical trapping of single gold nanorods

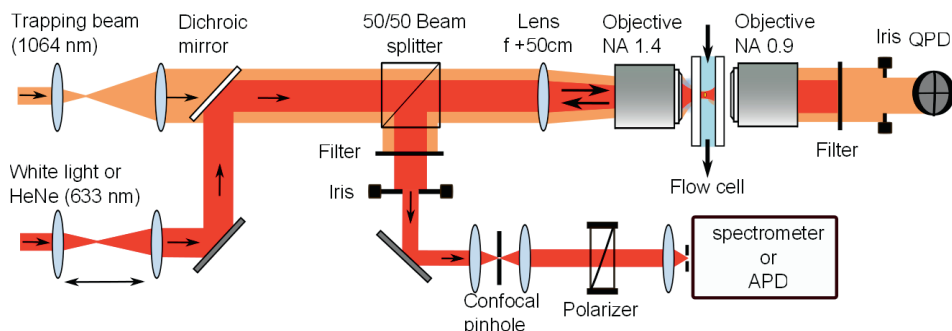


Figure 3.1: a) Scheme of the optical trap. QPD, Quadrant photodiode; APD, Avalanche photodiode

3.2 Methods and materials

3.2.1 Optical trapping setup, and integration with other microscopies

The optical setup schematically shown in Fig 3.1 consists of a single-beam optical trap at 1064 nm (5W IPG Photonics Ytterbium fiber laser). The home-built optical microscope was constructed during this project and has its optical axis parallel to the plane of the optical table (horizontal). The horizontal beam-axis facilitates the integration of the several optical setups that were used in the experiments described in this thesis. The microscope design (shown in Appendix B) aimed at optimizing mechanical and thermal stability.

The trapping beam is focused into water about $25 \mu\text{m}$ away from the glass substrate by an objective with a high numerical aperture (Olympus oil immersion 60 x, 1.4 NA). To alleviate the spherical aberrations introduced by water's too low index, the incoming trapping beam was made slightly convergent by means of a 50 cm lens just before the objective.¹¹⁸ This aberration correction was essential to achieve stable trapping of gold nanoparticles.

To obtain scattering spectra, white light from a Xenon arc lamp was focused to a spot and overlapped with the trap focus. Scattered light was collected by the focusing objective and detected by a nitrogen-cooled CCD camera coupled to a spectrograph. An iris inserted into the detection path selected the center 5 mm of the beam, to minimize depolarization effects by the objective. We inserted a $50 \mu\text{m}$ confocal pinhole at the focus of a 10 cm lens to reduce the background.

Translation and rotation dynamics of the trapped rods were deduced from

the back-scattered light of a HeNe laser (633 nm), detected by a single-photon counting photodiode (Perkin Elmer) and analyzed with a correlation card (PicoQuant). For the experiment we used a function generator to provide a reference signal with a frequency of 10 MHz. In all experiments, count rates at the detector were in the range $2 \cdot 10^5 - 4 \cdot 10^5$ counts per second.

3.2.2 **Materials**

Gold nanorods with 60 nm average length and 25 nm average diameter (sample $25 \text{ nm} \times 60 \text{ nm}$) and with 92 nm average length and 33 nm average width (sample $30 \text{ nm} \times 90 \text{ nm}$) were synthesized by the silver-assisted seed-mediated method¹¹⁹ in the presence of cetyltrimethylammonium bromide (CTAB) and coated with thiolated polyethyleneglycol (mPEG, MW5000, Sigma Aldrich) to prevent their aggregation in pure water.¹²⁰ The rod suspensions were diluted with ultrapure water to limit the trapping of multiple particles during the course of a measurement, up to 2 hours.

3.2.3 **Calibration of effective numerical aperture and intensity at the trap focus**

An important technical factor is the calibration of the intensity at the trap focus. The actual intensity at the trap focus is considerably reduced compared to the intensity that could be calculated in the ideal case for the following reasons: i) the objective's transmission in the NIR is only 19 %; ii) the objective is not corrected for imaging in water. Spherical aberrations reduce the intensity at the focus; iii) because of total internal reflection at the glass-water interface, the effective numerical aperture at the focus cannot exceed the index of refraction of water. Indeed, it is significantly weaker than 1.4, as explained hereafter.

The plot of Fig. 3.2 has been obtained by placing an iris on the NIR beam in front of the lens-objective system of the trap. The rotational correlation rate (inverse of the rotational correlation time), which is directly proportional to the local intensity at the focus (see Sec. 3.7) has been measured as a function of the beam diameter corresponding to the iris aperture (due to the convergence of the beam introduced by the lens, the diameter of the beam at the objective back aperture is about 0.8 times the iris aperture). We see that the trapping strength increases steeply with beam diameter, both because the transmitted power increases and because the numerical aperture increases. The measurements are in qualitative agreement with a function scaling as a

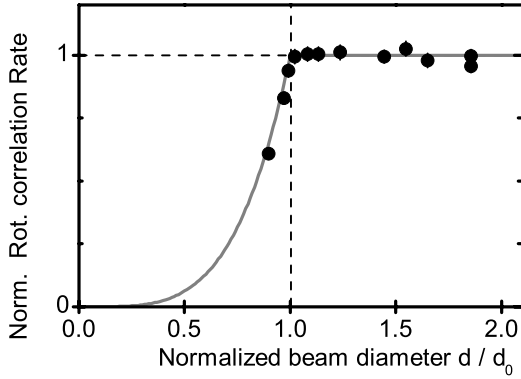


Figure 3.2: Determination of the effective numerical aperture of the trapping beam by the local intensity at the focus. The rotational correlation rate (inverse of the rotational correlation time), measured on a single trapped nanorod (25 nm \times 60 nm sample), is proportional to the local intensity. The measurements are plotted as function of the normalized beam d/d_0 , where d_0 is 8 mm at the objective back aperture, and the objective back aperture is 11.5 mm in diameter. The solid line is a concatenation of the functions $f(d) = (d/d_0)^4$ for $d < d_0$ and $f(d) = \text{constant}$ for $d > d_0$.

beam diameter to the fourth power, expected for this situation. For a beam diameter above a characteristic diameter d_0 , the local intensity at the focus remains constant. That means that the off-axis rays do not contribute to trapping. The numerical aperture corresponding to this characteristic diameter is 1.0 and has been used as the effective NA at the trap focus.

3.2.4 Identification of single and multiple trapped nanorods by their white light scattering spectra

To identify nanorods in the optical trap we have recorded their white light scattering spectrum. Our current procedure to trap a single rod is to start from a rather diluted suspension, and to wait for one nanorod to get trapped. At low enough concentration, this waiting time is about 10 minutes. The concentration of diffusing rods continuously decreases with time because rods stick to the surfaces of the flow cell. Therefore, trapping a second rod becomes more and more unlikely as time goes. Nonetheless, it occasionally happens. In that case, we observe a stepwise increase in scattered intensity, and the spectrum often clearly shows a split or broadened shape, as illustrated in Fig. 3.3. Usually, one of the two trapped rods is quickly ejected from the trap (after a few minutes) and either the initial rod or the newcomer re-

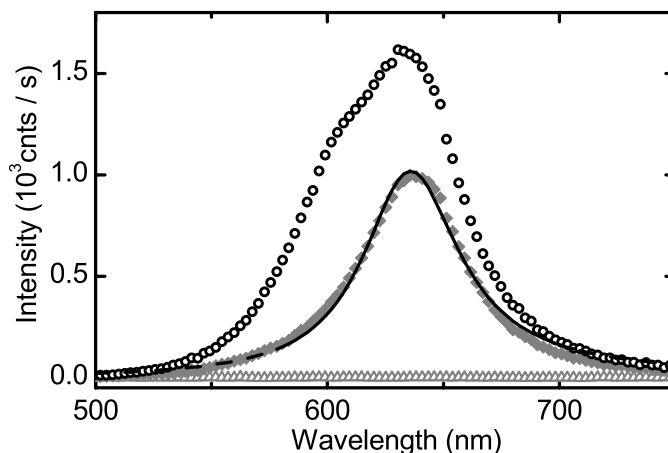


Figure 3.3: Spectra of scattered white light when zero (open gray triangles), one (solid gray diamonds) or two nanorods (open black circles) are trapped. Note the broadened and asymmetric shape of the latter spectrum due to difference in shape and size of the two trapped rods (sample: $25 \text{ nm} \times 60 \text{ nm}$). The spectrum changes in a stepwise way, as a new rod enters or leaves the trap. The black line is a Lorentzian fit (on an energy scale), where the fitted region is indicated by the solid part of the line. The width of the single particle spectrum is 50 nm (0.155 eV), a typical width of the plasmon resonance under our conditions.

mains in the trap for a long time. Trapping more than two rods only happens at high concentrations. In all measurements reported here there was only one nanorod in the trap.

3.3 Theory of optical forces and torques on gold nanorods

In this chapter we demonstrate the capabilities of our optical trapping setup by the stable three dimensional trapping of single gold nanorods. In this section we discuss the optical forces and torques acting on a gold nanorod in an optical field.

The optical response of a particle much smaller than the wavelength of light can be well described in the electrostatic limit, considering the particle as a dipole. The gold nanoparticles of sizes used in this thesis are small enough to be well described by this approximation. The scattering and absorption properties of the particle, and the optical forces and torques acting on the particle in the trap, can be calculated from the polarizability.

3.3.1 Polarizability

To evaluate the optical properties of the gold nanorods we calculate the polarizability of a prolate spheroid in the dipole approximation. For polarization of the incoming light parallel or perpendicular to the long principal axis of the ellipsoid, the polarizability is given as:⁶

$$\alpha_{\parallel,\perp}(\lambda) = 3\epsilon_0\epsilon_m(\lambda)V_p \frac{\epsilon(\lambda) - \epsilon_m(\lambda)}{3\epsilon_m(\lambda) + 3L_{\parallel,\perp}[\epsilon(\lambda) - \epsilon_m(\lambda)]} \quad (3.1)$$

where V_p is the volume of the particle, ϵ_m and ϵ are the complex dielectric functions of the medium and gold respectively and L_{\parallel} and L_{\perp} are geometrical factors. L_{\parallel} is given by

$$L_{\parallel} = \frac{1 - e^2}{e^2} \left(-1 + \frac{1}{2e} \ln \frac{1 + e}{1 - e} \right) \quad (3.2)$$

where e is the eccentricity, given as $e = \sqrt{1 - \rho^2}$, with ρ the aspect ratio of the spheroid. For L_{\perp} , we have

$$L_{\perp} = \frac{1 - L_{\parallel}}{2} \quad (3.3)$$

As the complex dielectric function of gold, we take the values measured by Johnson and Christy for bulk gold,¹¹³ see Appendix C. In the calculation of the polarizability of the gold nanorods, this bulk complex dielectric function is modified to take into account additional damping mechanisms present in the nanoparticle, electron surface scattering and radiation damping.¹²¹

In order to match the spectral width of the calculated scattering spectrum to the spectrum observed in the experiment we incorporate a larger damping than the values that were reported in Novo *et al.*¹²¹ We attribute this additional damping to chemical interface damping introduced by the thiol groups that bind the PEG capping layer to the gold.¹²² Part of the broadening of the linewidth could also be introduced by the increased temperature of the gold nanorod in the trap, via electron-phonon coupling. This broadening is on the order of 0.1 meV /K,¹²³ contributing an increase in linewidth of only 7-8 meV at the highest trapping power. Therefore, the heating contribution to the linewidth is a minor effect. We will explore the temperature dependence of the plasmon damping further in Chapter 5.

Figure 3.4 displays the polarizability of a gold nanorod of dimensions typical in our experiment, calculated using the above expressions.

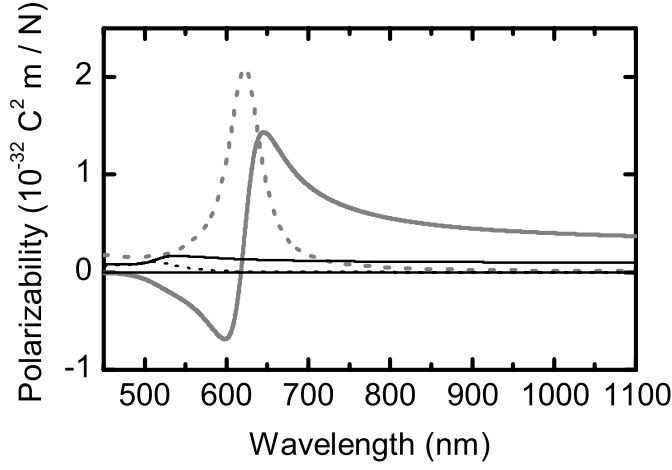


Figure 3.4: Calculated polarizability of a gold nanorod in water, in the dipole approximation (eqn 3.1). Grey (black) solid lines: real part of the polarizability for a field along the long axis (one of the short axes) of the rod. Gray (black) dashed lines: the imaginary part of the polarizability along the long axis (one of the short axes) of the rod. The nanorod has a volume $2.5 \cdot 10^4 \text{ nm}^3$ and an aspect ratio of 2.45 .

3.3.2 Optical forces

The optical forces that act on the gold nanoparticle are the gradient force \vec{F}_{grad} and the dissipative force \vec{F}_{d} due to the radiation pressure of the absorbed photons. In the dipole approximation the scattering force vanishes.¹²⁴ The total force \vec{F} on the particle is given as $\vec{F} = \vec{F}_{\text{grad}} + \vec{F}_{\text{d}}$. For an optical field $\vec{E}(\vec{r}, t) = \text{Re} \left\{ \vec{E}_0(\vec{r}) \exp(-i\omega t) \right\}$, the time-averaged gradient force on a particle with polarizability α is given as¹²⁴

$$\langle \vec{F}_{\text{grad}}(\vec{r}) \rangle = \frac{1}{4} \text{Re} \{ \alpha \} \vec{\nabla} |\vec{E}_0(\vec{r})|^2 \quad (3.4)$$

The time-averaged dissipative force is given as

$$\langle \vec{F}_{\text{d}}(\vec{r}) \rangle = \frac{1}{2} \vec{k} \text{Im} \{ \alpha \} |\vec{E}_0(\vec{r})|^2 \quad (3.5)$$

Using the above expressions we calculate the optical forces on a gold nanorod along the propagation axis of the trap beam. The rod has the same dimensions as the rod in Fig 3.4. As a trapping beam we take a Gaussian beam with a 1.0 numerical aperture. We assume that the rod's long axis is

3 Optical trapping apparatus, and characterization of optical trapping of single gold nanorods

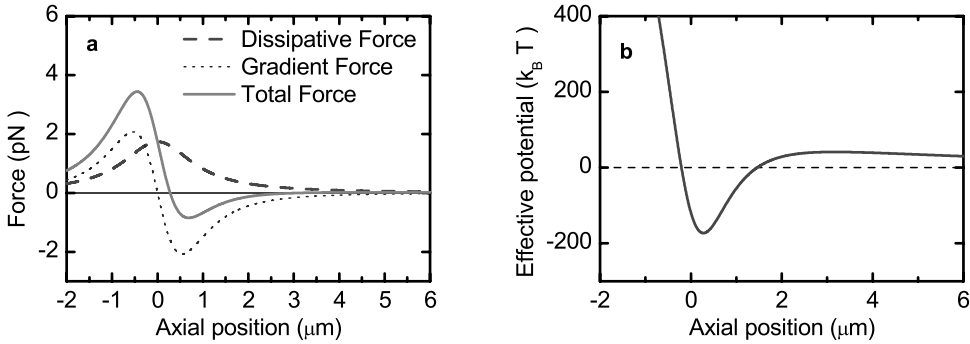


Figure 3.5: a) Calculated axial forces on a single gold nanorod, per Watt of optical power in the focus of a Gaussian beam of numerical aperture 1.0 and a wavelength 1064 nm. The nanorod polarizability is calculated in the electrostatic approximation, for a nanorod of volume of $2.5 \cdot 10^4 \text{ nm}^3$ and aspect ratio 2.45 (longitudinal resonance wavelength in water 624 nm) in water. b) Corresponding effective axial potential, per Watt of optical power.

parallel to the field, and compute α_{\parallel} as the polarizability of the rod in the above equations. The results are plotted in Fig. 3.5a as functions of the position along the axis of the beam. We see that the axial equilibrium position (the position at which the total force on the rod is zero) is shifted by about 275 nm from the focus of the beam. For a beam with a numerical aperture of 1.2 this axial shift would reduce to about 150 nm. For lower NA the axial shift would be larger.

Figure 3.5b displays the effective potential experienced by the gold nanorod in Fig. 3.5a. This potential is an effective potential as the dissipative force does not derive from a true potential. The effective potential depth for the particle in a 1 W trapping beam is about $175 k_B T$ (with $T = 300 \text{ K}$).

The trapping forces are proportional to the real part of the polarizability, with a positive real part leading to trapping at the intensity maximum of a focused beam. Larger values of the real part of the polarizability closer to the plasmon resonance lead to larger trapping forces. It would thus seem an advantage to use a trap laser with a wavelength close to the plasmon resonance, as long as it is on the long wavelength side of the half maximum of the resonance. However, this gain is more than compensated for by the larger imaginary part of the polarizability. Indeed, the imaginary part of the polarizability varies as a Lorentzian wing, whereas the real part follows a dispersion profile and decays much more slowly. The larger $\text{Im}(\alpha)$ leads to

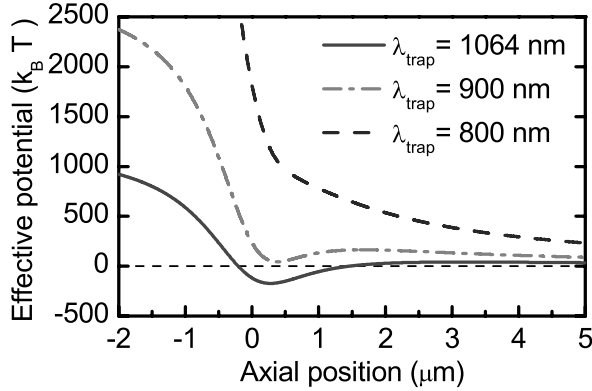


Figure 3.6: a) Calculated effective axial potentials, per Watt of optical power in the focus of Gaussian beam of 1.0 numerical aperture. The nanorod polarizability has the same parameters as the nanorod from figure 3.5.

a larger radiation pressure, pushing the particle out of the trap, as well as to more heating.

In Figure 3.6 we see the effective axial potentials that the same nanorod would experience for different wavelengths of the trapping laser. From the figure we see clearly the advantage of using a trap laser with a wavelength far in the red wing of the plasmon resonance. As the trapping wavelength approaches the resonance the effective potentials become less and less deep as the radiation pressure force starts to dominate the gradient force. For wavelengths below about 900 nm, stable trapping using a single beam gradient trap is no longer possible, at least for a numerical aperture of 1.0.

3.3.3 Optical torques

The anisotropic polarizability of gold nanorod leads to a trap potential that depends on the orientation of the nanorods with respect to the polarization of the trap laser

$$U(\theta) = -\frac{1}{4} \text{Re} \{ \Delta\alpha \} E_0^2 \cos^2 \theta, \quad (3.6)$$

where θ is the angle between the polarization of the trap and the rod's long axes. $\text{Re} \{ \Delta\alpha \} = \text{Re} \{ \alpha_{\parallel} - \alpha_{\perp} \}$ is the difference between the real parts of the longitudinal and transverse polarizabilities of the nanorod at the trap wavelength. The potential energy is minimized when the long axis of the rod is parallel to the polarization of the trap, because $\alpha_L > \alpha_T$. For realistic intensi-

3 Optical trapping apparatus, and characterization of optical trapping of single gold nanorods

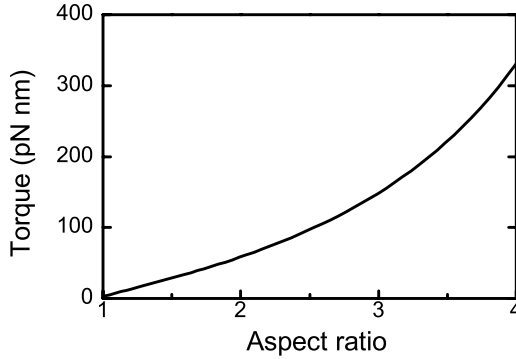


Figure 3.7: Maximum optical torque on a gold nanorod as function of aspect ratio, for a rod of constant volume. The torque is calculated according to Eq. 3.7, for typical parameters used in this thesis. The polarizability of the rod is calculated in the electrostatic approximation (Eq. 3.1) for a prolate gold spheroid of volume $2.5 \cdot 10^4 \text{ nm}^3$ in water, in a beam with wavelength 1064 nm and with local intensity $2.4 \cdot 10^{11} \text{ W/m}^2$. The local intensity corresponds to an optical field amplitude $E_0 = 1.3 \cdot 10^7 \text{ V/m}$ and, for typical experimental conditions in this thesis, to an optical power of about 80 mW at the focal plane. The maximum torque is proportional to the local intensity and, in the electrostatic approximation, to the volume of the ellipsoid.

ties of the trapping laser, the depth of orientational potential is several times the thermal energy. We thus expect that nanorods align in the optical trap.

To see the same property in a different way, we can evaluate the optical torque on the nanorod. The time-averaged optical torque on a dipole in an optical field is given as

$$\vec{T} = -\frac{1}{2}\kappa_{\text{rot}} \sin(2\theta) \hat{k} \hat{k} \quad (3.7)$$

where $\hat{k} \hat{k}$ is a unit vector in the direction perpendicular to the rods long axis, and κ_{rot} is the rotational trap stiffness, given by

$$\kappa_{\text{rot}} = \frac{1}{2} \text{Re} \{ \Delta \alpha \} E_0^2. \quad (3.8)$$

The maximum torque that is exerted on the nanorod is $T_0 = 0.5\kappa_{\text{rot}}$. The torque is shown in Figure 3.7 as function of the rods aspect ratio.

Experimental Results

3.4 Thermal stability of trapped nanorods

Surface gold atoms are considerably more mobile than bulk ones. Surface diffusion leads to shape changes in gold nanoparticles, even at temperatures much lower than 1064°C, the melting temperature of bulk gold.¹²⁵ This phenomenon is called reshaping. Gold nanorods reshape into the thermodynamically more stable spherical shape, possibly with facets. While at room temperature gold nanorods in solution can be stable for several months to years, at a temperature of 250 °C rods reshape into spheres within 1 h.¹²⁵ During reshaping, the shape of the rod remains close to a spherically capped cylinder, and the particle aspect ratio can be deduced from the longitudinal plasmon wavelength, as for non-heated rods.¹²⁵

As gold nanoparticles heat up in the optical trap due to absorption of the trap laser,^{77,88,89} it is important to test for possible reshaping. We have studied the thermal reshaping of a sample of gold nanorods both on the ensemble level -by heating in an oven- and for single rods in the optical trap. The results on the ensemble of rods in the oven are shown in Fig. 3.8 (a) for a temperature of 95 °C. The sample had an average aspect ratio of 2.5, yielding a longitudinal plasmon resonance at 625 nm. The thermal reshaping leads to a blue shift of the longitudinal plasmon by about 3 nm in one hour, corresponding to a change in aspect ratio of about 1.5%. Fig. 3.8 (b) shows the plasmon resonance for 9 individual nanorods in the optical trap, as a function of the time spent in the trap. A first quick regime of blue shifting, seen in the inset for one of the rods, might be due to desorption of residual organic capping molecules (CTAB, PEG) due to the temperature change. This regime was followed by a very stable period, where the blue shift was limited to less than 1 nm in half an hour. Therefore, we conclude that reshaping was negligible for these nanorods, and that the temperature in the trap did not exceed 95°C. The results of Figure 3.8 show that single gold nanorods can be stably trapped with negligible reshaping, for periods of at least 0.5 h.

We have also observed thermal reshaping of trapped nanorods. Fig. 3.9(a) shows an example of a single nanorod that reshapes over time. This rod was first trapped at a low power, and a blue-shift is recorded upon increasing the trapping power. This blue-shift is attributed to reshaping. The process of reshaping in the trap is self-stabilizing: as the plasmon resonance shifts to the blue, the absorption at the trap laser wavelength decreases, the temperature of the rod decreases and the reshaping process is slowed down. As a result,

3 Optical trapping apparatus, and characterization of optical trapping of single gold nanorods

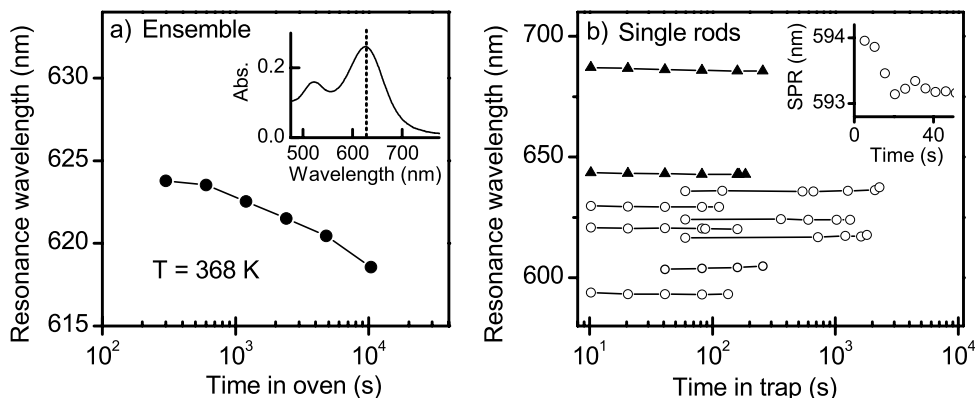


Figure 3.8: Thermal stability of gold nanorods (25 nm \times 60 nm, PEG-coated). (a) Longitudinal plasmon resonance of an ensemble of gold nanorods in water, at different times after heating in a laboratory oven at 368 K (95 °C). Inset: Absorption spectrum of the ensemble before heating. The dotted line indicates the longitudinal plasmon resonance at 625 nm. (b) Longitudinal plasmon resonance of scattering spectra of 9 single gold nanorods in the optical trap, as a function of the time since they were first trapped. Inset: plasmon resonance SPR of one of the rods at short times. Trapping power at the focal plane was 60 to 80 mW (open circles) or 40 mW (solid triangles).

stable trapping at a given trap laser power will be limited to rods with an aspect ratio below a certain value. This behavior can be seen in Fig. 3.9 (b). Here we recorded the resonance wavelengths of about 20 nanorods in conditions where they were stably trapped, with plasmon shifts due to reshaping less than about 1 nm in 10 minutes. At the lowest trapping power, the average plasmon resonance is still close to the value measured on the ensemble. As the trapping power increases, only rods with shorter plasmon resonance wavelengths are stably trapped.

The results of Figures 3.8 and 3.9 show that gold nanorods can be stably trapped in three dimensions over extended periods of time (hours), but care must be taken to avoid thermal reshaping. In particular, trapping with a trap laser wavelength close to the plasmon resonance will cause a large absorption and lead to thermal reshaping of rods.

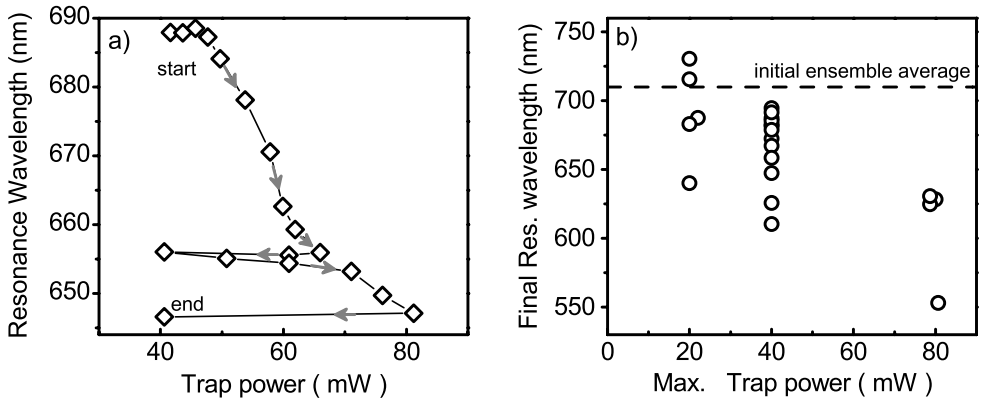


Figure 3.9: Thermal reshaping of single nanorods in the trap, ($30 \text{ nm} \times 90 \text{ nm}$, PEG-coated). a) Trajectory of the longitudinal plasmon resonance of a single trapped nanorod as a function of trap power. The time interval between the start and the end of the trajectory was about 20 min. b) Final wavelength of the longitudinal plasmon resonance for a set of single gold nanorods in the trap, after reshaping. The data is plotted as a function of the maximum trap power that the individual rods were exposed to. The dashed line indicates the longitudinal plasmon resonance of the absorption spectrum of the ensemble. Indicated trap powers are at the focal plane.

3.5 Gold nanorods align with the trap polarization

As the scattering cross section of gold nanorods depends strongly on the polarization of the light relative to the long axis of the rod, alignment of the nanorods in the trap can be observed by analyzing the polarization dependence of the scattered light. Figure 3.10 (a) shows scattering spectra of a single gold nanorod, recorded with an analyzer in the detection path at various orientations with respect to the trap polarization. The incoming light from the thermal source is unpolarized. The spectrum recorded with the analyzer parallel to the trap polarization (0°) is much more intense than the spectrum recorded with the analyzer perpendicular. This observation shows that trapped gold nanorods align with their long axis parallel to the trap laser polarization. Fig. 3.10 (b) displays the polarization dependence of the intensity of the longitudinal plasmon over 360° . The dependence is well described by a squared cosine function, expected for the dipolar longitudinal plasmon resonance.

Due to thermal fluctuations, a trapped gold nanorod will undergo orientational fluctuation around the equilibrium orientation defined by the trap

3 Optical trapping apparatus, and characterization of optical trapping of single gold nanorods

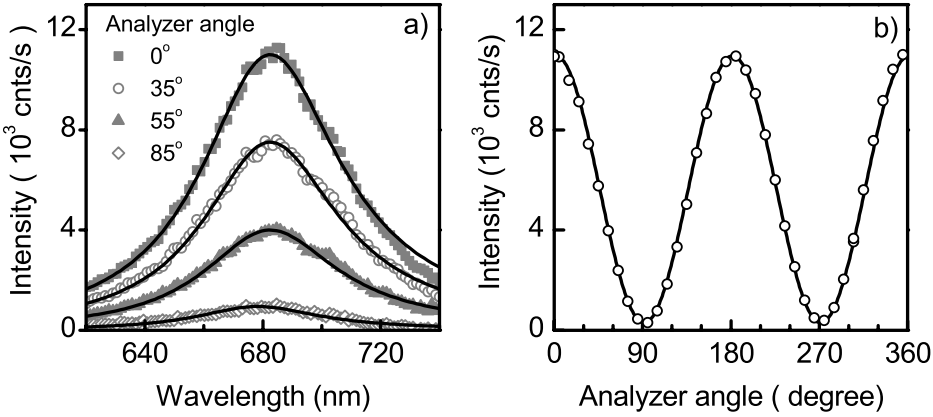


Figure 3.10: Alignment of a single gold nanorod in the trap observed by its polarization-dependent scattering spectrum (30 nm \times 90 nm rod, PEG-coated). (a) Scattering spectra, recorded with unpolarized white light in excitation and an analyzer in the detection path. Spectra are shown for several orientations θ of the analyzer with respect to the trap polarization. Solid lines are Lorentzian fits, with resonance wavelength 682 nm and width 57 nm. (b) Maximum intensity of the longitudinal plasmon as a function of the orientation of the analyzer, obtained from the Lorentzian fit of the scattering spectrum. Solid line is a fit of a squared cosine plus offset.

polarization. The alignment of a rod in the trap will thus not be as perfect as would be observed for a nanorod immobilized on a solid substrate.

Fig. 3.11 (a) displays scattering spectra of a trapped nanorod, detected with an analyzer parallel or perpendicular to the trap polarization. The spectrum recorded with an analyzer perpendicular to the trap laser is much weaker. The spectrum shows residual intensity of the longitudinal plasmon around 630 nm and the transverse plasmon around 530 nm. Fig. 3.11 (b) shows that the polarization dependence of the intensities of the longitudinal and transverse plasmon is well described by a \cos^2 and a \sin^2 function, respectively, as expected.

The amplitude of the orientational fluctuation directly reflects the competition between the orientational trap depth and the thermal fluctuations. In Chapter 4 we will show how the polarization ratio can be used to quantify the optical torque acting on the trapped rod, by using Boltzmann statistics. A quantitative evaluation of the polarization intensity ratio rests on a polarization analysis of the light scattered by a single nanorod. The actual setup departs in two ways from the ideal situation of a nanorod precisely trapped at the focus of the linearly polarized excitation beam: i) the nanorod is displaced

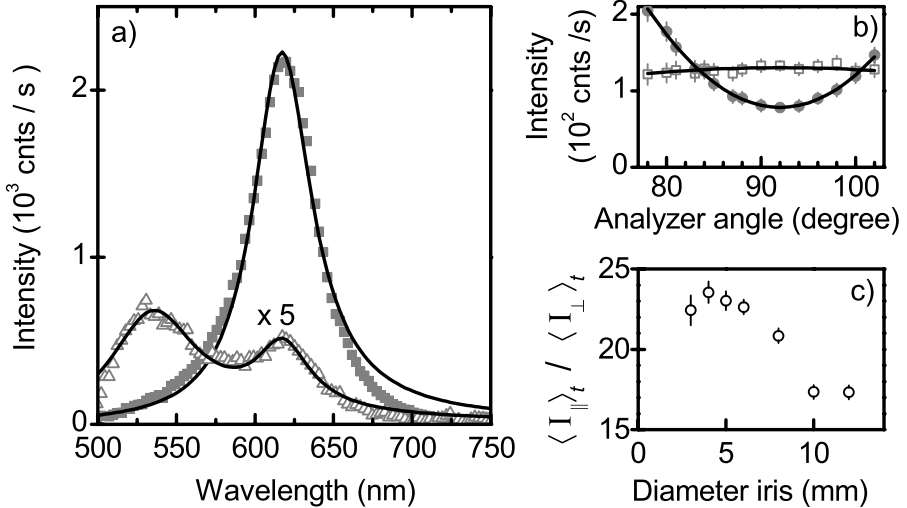


Figure 3.11: Polarization ratio of a single trapped nanorod, $25 \text{ nm} \times 60 \text{ nm}$. a) White light scattering spectra from a single trapped nanorod, with analyzer parallel (solid squares) or perpendicular (open triangles) to the trap polarization. Solid lines are Lorentzian fits (in frequency). The perpendicular spectrum is fitted with a sum of two Lorentzians. b) Spectral intensities recorded with the analyzer around the perpendicular orientation. Solid circles: Longitudinal resonance. Open squares: transverse resonance. c) Ratio $\langle I_{\parallel} \rangle_t / \langle I_{\perp} \rangle_t$ as a function of the diameter of the iris aperture in the detection path. Diameter of the objective back aperture is 11.5 mm .

from the focus and from the beam axis by thermal fluctuations. Therefore, it experiences polarization components in the longitudinal direction as well as along the perpendicular direction in the focal plane. Because of the rod's displacement, the scattered light will also be slightly depolarized with respect to the central position. ii) even when the rod lies at the center of the trap, the light scattered by the rod is collected with a large numerical aperture, which may lead to depolarization of the detected light. The magnitude of the latter effect can be minimized by limiting the solid angle of the detection.

Figure 3.11 (c) shows how the polarization ratio of light scattered by a trapped nanorod changes when an iris is placed in the detection path, as a function of the iris aperture. This ratio, which reaches 24 here for a strong alignment, clearly decreases for apertures larger than 6 mm , but keeps a constant value, within experimental error, for smaller apertures. For apertures less than 2 mm , the signal-to-noise ratio was too small to measure. For quantitative analysis of the polarization ratio (Chapter 4), the iris diameter was

fixed at 5 mm, a value for which depolarization in the detection is still negligible.

3.6 Characterization of trapping forces by position fluctuations

In Section 3.5 we have shown that single gold nanorods can be optically trapped in water for extended times, up to hours. This observation confirms that the potential depth of the trap is significantly larger than $k_B T$. This simple observation suffices for many of the applications of the trap discussed (or envisioned) in this thesis.

Applications that use optically trapped objects as a transducer of a known force or torque, require a quantitative knowledge of (the bottom of) the trap potential, and a measurement of the displacement (in position or angle) of the particle from the trap equilibrium position.

Here we characterize the optical potential by an analysis of the position fluctuations of the trapped particle, a method commonly applied in the literature for both microscopic dielectric and nanometric metallic particles.^{67,75,126} In this method, the interference between the light scattered by the fluctuating particle and the transmitted trap beam is recorded on a quadrant photodiode (QPD) in the back focal plane of a collection objective. The motions of the particle in the trap can be recovered by an analysis of the intensity distribution of the beam. Specifically, a transversal displacement of the particle away from the trap center causes a transversely asymmetric intensity distribution, resulting in a voltage on the X or Y channels of the QPD, for which the signal is proportional to the difference in the intensity between the left/right, or up/down quadrants. A displacement of the particle in the longitudinal direction modifies the total collected intensity, represented by the sum of all quadrant signals.

The intensity distribution in the trap focus is approximately Gaussian in all three dimensions, resulting in a harmonic potential in the X, Y, and Z direction. The force on a trapped particle in each direction is then given by Hooke's law, with a spring constant (trap stiffness) κ . In each dimension, the Brownian motion of the trapped particle is described by a Langevin equation. For example, in the x-direction we have $m\ddot{x} = -\kappa_x x - \gamma_x \dot{x} + \mathcal{F}(T, t)$, where κ_x is the trap stiffness in the x-direction, γ_x is the corresponding friction coefficient, and $\mathcal{F}(T, t)$ is a term describing the white noise that results from the random collisions of the surrounding molecules with the particle.

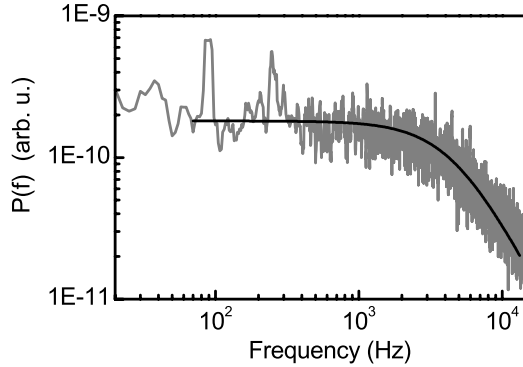


Figure 3.12: Power spectrum (in a transverse direction) of a single gold nanorod (sample average 30 nm diameter, 90 nm length, PEG coated), for transverse fluctuations of the rod. The black line is a fit of a Lorentzian with the corner frequency $f_c = 4.7$ kHz. The trapping power was 60 mW at the focal plane.

The inertial term can be neglected. The Fourier transform of the Langevin equation results in a Lorentzian power spectrum, with a corner frequency $f_c = \kappa / (2\pi\gamma)$.

Figure 3.12 displays the Fourier transform (power spectrum) of the transverse fluctuations of a single trapped gold nanorod. The spectrum is well fitted by a Lorentzian with a corner frequency $f_c = 4.7$ kHz.

The trap stiffness k can be obtained from the measured corner frequency if the friction coefficient of the trapped particle is known. For the friction coefficients of the rod, we use the expressions for a prolate spheroid derived by Perrin,¹²⁷ see Appendix D. Alternatively, we could use the expressions for a cylinder, derived in the limit for infinitely long cylinders, with a correction for their finite size.^{128,129} The friction coefficients calculated by these two models for the gold nanorods in our experiment differ by less than about 20% for rotational friction, and less than 2% for translation friction, see Appendix D. The interpretation of our experimental results is not sensitive to the model that is used, at least up to the accuracy obtained thus far. The advantage of the friction coefficients for ellipsoids is that the analytic expressions are valid for any aspect ratio. In contrast, the friction coefficients for cylinders are valid only for aspect ratios larger than 2.

More important than the geometric shape factor in the friction coefficient is the fact that all friction coefficients are proportional to the shear viscosity of the medium. Viscosity is a strongly temperature dependent parameter for many typically used liquids. For example, the viscosity of water at 90 °C is

more than a factor of 3 lower than at room temperature, see Appendix D. As the metal nanoparticle can heat up significantly in the trap, a first requirement therefore is to know the particle temperature, and the corresponding local viscosity. We can then describe the Brownian motion of the hot particle in an inhomogeneous temperature and viscosity profile, which will be discussed in Chapter 4.

3.7 Translational and rotational dynamics observed by photon correlation spectroscopy

To investigate the rotational dynamics of the rods in the trap we apply photon correlation spectroscopy on the polarized light scattered by the nanorods. Photon correlation spectroscopy has been introduced as a technique to characterize particles in optical traps by Bar-Ziv *et al.*¹³⁰ and Meller *et al.*,¹³¹ for micron-sized dielectric particles. Photon correlation is a convenient technique to measure the rotational dynamics of nanoparticles as it provides access to a wide range of time scales in a single measurement, down to the nanosecond regime.¹³⁰ Whereas for a particle of 1 micron diameter rotational correlation times are on the order of seconds, the rotational correlation times of a 30 nm diameter particle is $3 \cdot 10^4$ times shorter, because the rotational friction coefficient scales as the particle volume. For these small particles, correlation times are on the order of microseconds or shorter, and are difficult to access with position-sensitive detectors.

Due to the optical anisotropy of gold nanorods, the rotational dynamics can be recorded with polarization-sensitive scattering measurements, as has been applied on freely diffusing ensembles of rods.^{132,133} The rotational dynamics of weakly trapped gold nanorods have been measured by fluorescence correlation spectroscopy,⁸⁰ by averaging over many individual rods. To our knowledge, photon correlation has thus far not been applied to quantify the rotational and translational dynamics of single stably trapped particles (either metal or dielectric) with sizes below ~ 100 nm.

3.7.1 Dynamics of a gold nanorods trapped in water

Here we provide autocorrelation functions measured on an optically trapped nanorod using a photon counting APD, with polarization-sensitive and polarization-insensitive detection. The result is shown in Fig. 3.13. The polarization-sensitive measurement is well fitted by a bi-exponential decay. The fast re-

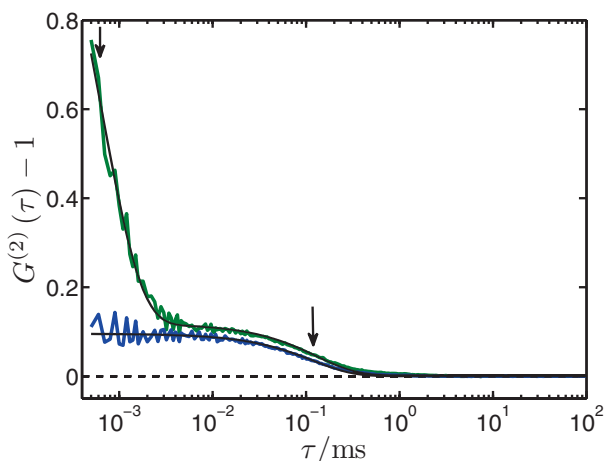


Figure 3.13: Autocorrelation functions of light from a HeNe laser, scattered by a single trapped gold nanorod in water. Green solid line: linearly polarized excitation parallel to the trap, with a detection analyzer perpendicular to the trap polarization. Blue solid line: Circularly polarized excitation, without analyzer in the detection. Solid black lines are a bi-exponential fit (characteristic times $0.64 \pm 0.01 \mu\text{s}$ and $131 \pm 0.6 \mu\text{s}$, indicated by the arrows) and a single-exponential fit $118 \pm 0.4 \mu\text{s}$ of the green and blue curves, respectively. Trapping power 80 mW, integration time 20 s.

laxation is due to rotational fluctuations of the rod in the trap. The slower relaxation is due to transverse and axial translational fluctuations in the trap. With the polarization-insensitive detection, only the slow translational part is seen. The correlation function is well fitted with a single exponential decay, with the same characteristic time as the one measured in the translational part of the autocorrelation function measured with the polarization-sensitive detection.

Dynamics of a gold nanorod trapped in a viscous glycerol mixture

Fig 3.14(a) displays the polarization-sensitive and polarization insensitive correlation functions on a single nanorod trapped in a viscous glycerol-water mixture. Here the rotational and translation relaxation times are slowed down. Whereas in water only the steep decrease of the rotational contrast could be detected, in glycerol the plateau of the rotational contrast can be clearly resolved.

Due to the much slower dynamics of the rod trapped in glycerol compared to pure water, in glycerol a fair number of photons ($\sim 10^2$) are collected

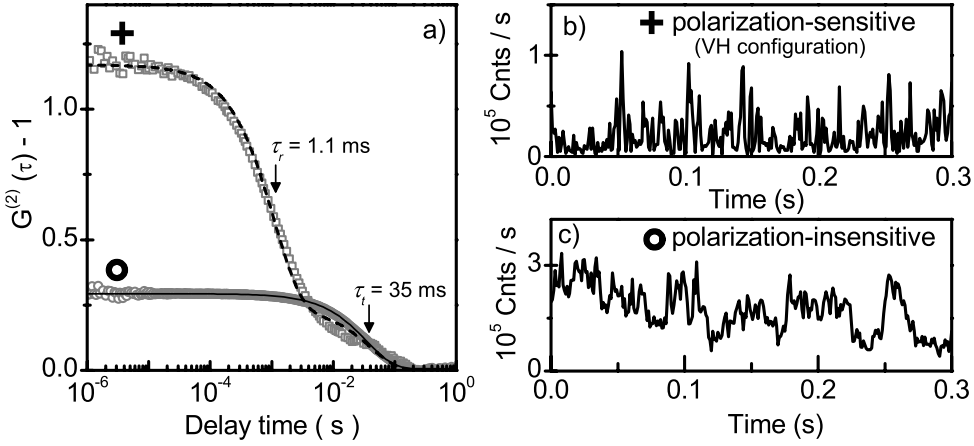


Figure 3.14: Translational and rotational dynamics of a single trapped gold nanorod in a viscous glycerol-water mixture (80% glycerol by volume). (a) Autocorrelation functions of light scattered by a trapped nanorod. Open gray squares: scattered light from a HeNe laser, with an analyzer in the perpendicular direction. Open gray circles: scattered white light from a Xe lamp, without analyzer. The solid (dotted) curves are (bi)-exponential fits with characteristic time(s) $\tau_t = 35 \pm 0.4$ ms ($\tau_t = 40 \pm 4$ ms and $\tau_r = 1.1 \pm 0.03$ ms). (b) Time trace of the scattered intensity of the HeNe light with analyzer in the perpendicular direction, directly showing the intensity fluctuations due to rotational fluctuations of the rod. (c) Time trace of scattered white light without analyzer, showing intensity fluctuations due to the rod’s translational fluctuations. For the time traces, photon counts have been grouped in 1 ms time bins. Trapping power was 60 mW at the focal plane.

per rotational fluctuation time. The time traces of the scattered intensities in Fig 3.14 (b) and 3.14 (c) clearly show the intensity fluctuations due to rotational and translation fluctuations, respectively.

3.8 Conclusions

In this Chapter, we have shown that single nanorods of 25 nm nominal width and 60 nm nominal length (nominal aspect ratio 2.5) can be stably trapped in solution with an infrared single beam optical trap (1064 nm wavelength). We showed that the nanorods align along the polarization of the trap laser by time-averaged, polarization-sensitive white light scattering spectra. We measured the combined translational and rotational dynamics of the trapped nanorods by polarization-sensitive photon correlation spectroscopy. We have

investigated the thermal stability of the trapped gold nanorods, and found conditions under which rods can be trapped for more than half an hour without significant thermal reshaping. For rods with aspect ratios above about 3 significant reshaping was observed at the high end of the trapping powers used here, around 80 mW at the focal plane, corresponding to a local intensity of about $2 \cdot 10^{11}$ W/m². The lower thermal stability of the longer nanorods was attributed to the closer proximity of their longitudinal plasmon resonance to the trap laser wavelength, leading to larger absorption cross-sections and increased trap laser-induced heating. Our results show the promise of optically trapped gold nanorods as ultra-small trapping handles with control over both position and orientation. Additionally, our results demonstrate the important role of laser-induced heating of the rods. While conditions for stable trapping of single gold nanorods can be found, a careful in-situ determination of the thermal stability of the trapped nanorods is required.

Brownian fluctuations and heating of an optically aligned gold nanorod

Abstract – We present the first quantitative measurements of the torque exerted on a single gold nanorod in a polarized three dimensional optical trap. We determined the torque both by observing the time-averaged orientation distribution and by measuring the dynamics of the rotational Brownian fluctuations. The measurements are in good agreement with calculations, where the temperature profile around the hot nanorod gives rise to a reduced, effective viscosity. The maximum torque on a 60 nm x 25 nm nanorod was 100 pN·nm, large enough to address single-molecule processes in soft and biological matter.

The contents of this chapter have been published:
P. V. Ruijgrok, N. R. Verhart, P. Zijlstra, A. L. Tchebotareva and M. Orrit, “Brownian fluctuations and heating of an optically aligned gold nanorod”, *Phys. Rev. Lett.* **107**, 037401 (2011)

4.1 Introduction

Since their invention some 30 years ago,^{65,66} optical tweezers have become a versatile tool to study the mechanics of soft matter, investigate the statistical mechanics of model systems, and enable fabrication on the nanometer scale.⁷¹ Rapid advances in optical trapping techniques have led to new methods by which both forces and torques can be exerted and measured. Most of those exploit the action of a polarized trap laser on an optically anisotropic microparticle.^{134,135} These advances have led to a better understanding of the rotational Brownian motion of a microparticle in the laser potential,¹³⁶ and resulted in the first simultaneous measurement of torque, angle, force and position during supercoiling of DNA.¹³⁷

Applications in environments that are structured on the nanometer scale, as found in soft matter systems, require trapping handles smaller than - or comparable in size to - the structures under study. However, optical trapping of dielectric particles below 300 nm in diameter is difficult. In contrast, the large polarizability of a metal compared to a dielectric enables the stable trapping of spherical gold nanoparticles⁷⁴ down to a diameter of 9.5 nm.⁷⁶ The optical forces that can be exerted on a metal nanoparticle have been characterized for gold and silver nanospheres^{75,77,78} and gold nanorods.⁷⁹ The shape and volume of the metal nanoparticles largely determine the accessible forces, which range from 0.1 to 10 pN for gold nanorods smaller than 100 nm, i.e., relevant forces for many biophysical and soft matter systems.⁷⁰ More interestingly still, non-spherical metal nanoparticles also experience torques in optical traps, because of the anisotropy of their polarizability tensor.^{80,84} Simultaneously applying a torque and a force to a metal nanoparticle would be particularly appealing for single-molecule experiments. However, no quantitative measurements of optical torques on such small particles have been published yet.

In this chapter, we demonstrate that a single gold nanorod of 25 nm in diameter and 60 nm in length can be used to exert optical torques of up to 100 pN · nm in a linearly polarized, three-dimensional optical trap. The restoring optical torque leads to a strong alignment of the rod, limiting the amplitude of its Brownian orientation fluctuations to about 14 degrees. In addition, we exploit the dipolar character of the rod's longitudinal plasmon resonance¹³⁸ to accurately determine the optical torque in two independent ways: (1) via the time-averaged orientation distribution deduced from white-light scattering spectra, and (2) through a dynamical analysis of rotational Brownian fluctuations observed in the polarized scattered intensity. We de-

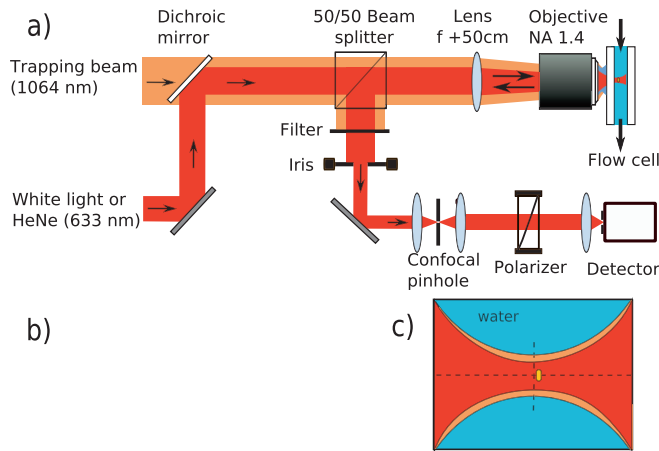


Figure 4.1: a) Scheme of the optical trap. b) Scanning electron micrograph of some gold nanorods. c) Scheme of a rod trapped in the laser focus in water. The rod is slightly shifted along the axis by radiation pressure.

termine the rod's heating by the trap beam and provide first data on the combined translational and rotational Brownian motions of a hot object in an optical trap.

4.2 Experimental Methods

The optical setup schematically shown in Fig 4.1(a) consists of a single beam optical trap at 1064 nm (5W IPG Photonics Ytterbium fiber laser). The trapping beam is focused into water about $25\ \mu\text{m}$ away from the glass substrate by an objective with a high numerical aperture (Olympus oil immersion 60 x, 1.4 NA). To alleviate the spherical aberrations introduced by water's too low index, the incoming trapping beam was made slightly convergent by means of a 50 cm lens just before the objective.¹¹⁸ We estimated an effective numerical aperture of 1.0 at the trap focus, see chapter 3. To obtain scattering spectra, white light from a Xenon arc lamp was focused to a spot and overlapped with the trap focus, see Fig. 4.1(c). Scattered light was collected by the focusing objective and detected by a nitrogen-cooled CCD camera coupled to a spectrograph. An iris inserted into the detection path selected the center 5 mm of the beam, to minimize depolarization effects by the objective (see Chapter 3). We inserted a $50\ \mu\text{m}$ confocal pinhole at the focus of a 10 cm lens to reduce the background. Translation and rotation dynamics of the trapped rods were deduced from the back-scattered light of a HeNe laser (633 nm),

detected by a single-photon counting photodiode and analyzed with a correlation card. Gold nanorods with 60 nm average length and 25 nm average diameter, shown in the electron micrograph in Fig. 4.1(b), were synthesized by the silver-assisted seed-mediated method¹¹⁹ and coated with thiolated polyethyleneglycol (mPEG, MW5000, Sigma Aldrich) to prevent their aggregation in pure water.¹²⁰ The rod suspensions were diluted with ultrapure water to limit the trapping of multiple particles during the course of a measurement, up to 2 hours.

White-light scattering spectra of a trapped nanorod are shown in Fig. 4.2(a). The parallel spectrum (analyzer along the trap polarization), displays the strong longitudinal plasmon, with maximum at 625 nm. The (nearly) Lorentzian shape of the spectrum and its narrow width (49 nm FWHM) confirm that only a single particle is trapped, see Chapter 3. With an analyzer perpendicular to the trap's polarization, the scattered signal is much weaker. Its spectrum shows residual intensity from the longitudinal plasmon at 625 nm and the transverse plasmon at about 550 nm.

4.3 Torsional stiffness quantified by the time averaged distribution of orientations

Because of the dipolar angular dependence of the scattered intensity, the time-averaged intensity $\langle I_{\perp} \rangle_t$ of the longitudinal plasmon observed in the perpendicular direction mainly arises from small angular fluctuations of the rod around its equilibrium orientation along the trap polarization. The intensity ratio $\langle I_{\parallel} \rangle_t / \langle I_{\perp} \rangle_t$ can be directly related to the ratio of the rotational trapping energy (or trap depth) to the thermal energy $k_B T$. The time-averaged intensities of the longitudinal plasmon in the two directions are the thermal expectation values $I_0 \langle \cos^2 \theta \rangle_T$ and $I_0 \langle \sin^2 \theta \cos^2 \phi \rangle_T$ (θ and ϕ are the polar angles of the rod axis, see Appendix E). The probability of finding angles θ, ϕ is given by a Boltzmann distribution $\exp \left\{ -U(\theta) / k_B \widetilde{T}_B \right\}$, with an effective temperature \widetilde{T}_B accounting for heating by the absorbed trap light. The potential energy U is that of the rod's induced dipole in the optical field E_0 , given by

$$U(\theta) = -\frac{1}{4} \text{Re} \{ \Delta \alpha \} E_0^2 \cos^2 \theta = -\frac{1}{2} \kappa_r \cos^2 \theta, \quad (4.1)$$

where $\text{Re} \{ \Delta \alpha \} = \text{Re} \{ \alpha_L - \alpha_T \}$ is the difference between the real parts of the longitudinal and transverse polarizabilities of the nanorod at the trap wave-

4.3 Torsional stiffness quantified by the time averaged distribution of orientations

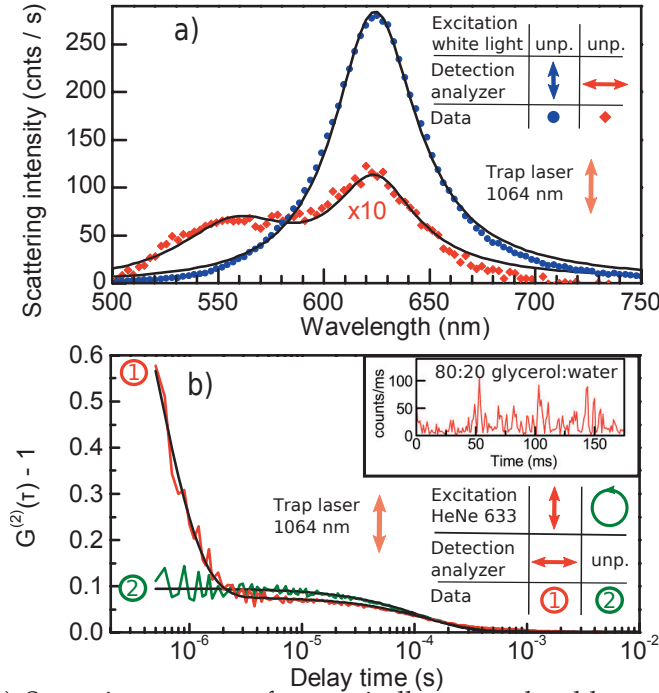


Figure 4.2: a) Scattering spectra of an optically trapped gold nanorod in water, recorded with unpolarized excitation and analyzed parallel (blue circles) or perpendicular (red diamonds) to the trap polarization. The solid lines are Lorentzian fits. Trapping power 80 mW, integration time 15 s. b) Autocorrelation functions of light from a HeNe laser, scattered by a trapped nanorod in water. Data set 1 (Red): Same nanorod as a), with an analyzer in the perpendicular direction. Data set 2 (Green): A different nanorod than a), with circularly polarized excitation and without analyzer in the detection. The solid curves are (bi-)exponential fits (characteristic times $0.48 \pm 0.01 \mu\text{s}$ and $132 \pm 8 \mu\text{s}$ for data set 1, and $96 \pm 2 \mu\text{s}$ for data set 2). Trapping power 80 mW, acquisition time 20 s. Inset: Time trace of the intensity scattered by a rod trapped in a glycerol-water mixture, directly showing slowed down orientation fluctuations. Photon counts have been grouped in 1 ms time bins.

length, and κ_r is the rotational trap stiffness, equal to the rotational spring constant of the trap for small angles. In the limit of high rotational trap stiffness, the spectral intensity ratio is well approximated by (see Appendix E):

$$\langle I_{\parallel} \rangle_t / \langle I_{\perp} \rangle_t \simeq \kappa_r / (k_B \widetilde{T}_B) - 3. \quad (4.2)$$

A measured intensity ratio $\langle I_{\parallel} \rangle_t / \langle I_{\perp} \rangle_t = 29$ thus directly yields a trap depth $\kappa_r/2$ of $16 k_B \widetilde{T}_B$. This corresponds to root-mean-square angular fluctuations

$\theta_{RMS} \approx \sqrt{2k_B \widetilde{T}_B / \kappa_r} = 14^\circ$. The maximum torque that can be exerted is $\kappa_r/2 \approx 100 \text{ pN} \cdot \text{nm}$.

4.4 Torsional stiffness quantified by the orientational relaxation time

The angular trapping of the rod can also be characterized by the dynamics of the rotational Brownian motion. We excited the rod with a HeNe laser at 633 nm linearly polarized along the trap polarization, and detected the scattered light behind an analyzer oriented in the perpendicular direction, see Fig. 4.2(b), curve 1. As the rod wiggles around its equilibrium, the detected signal fluctuates between zero and positive values, as scattering from the transverse band and residual background are negligible. This signal is displayed in the inset of Fig. 4.2(b) for a nanorod trapped in a viscous water-glycerol mixture, where the rotational dynamics are slowed down. Fig. 4.2(b) shows the normalized autocorrelation function of the light scattered by the gold nanorod of Fig. 4.2(a), trapped in water. The correlation function is well fitted by a bi-exponential decay. We attribute the fast relaxation to rotational fluctuations of the rod in the trap. The slower relaxation is due to the transverse and axial translations of the rod in the focus, which also modulate the scattered intensity. To confirm this attribution, we recorded autocorrelation functions with circularly polarized excitation and unpolarized detection, shown in Fig. 4.2(b), data set 2. These measurements indeed present only the slow translational part, without the fast relaxation due to orientation fluctuations. In the limit of strong alignment, the rotational correlation time τ_r is half the macroscopic relaxation time of the rod in the trap, itself the ratio of the rotational friction coefficient ζ_r to the trap stiffness κ_r (see Appendix F):

$$\tau_r = \zeta_r / 2\kappa_r \quad (4.3)$$

where $\zeta_r = \eta V C_r$, η is the viscosity of water, V the hydrodynamic volume, and C_r a geometrical factor.

4.5 Temperature dependent dynamics of Brownian fluctuations in the trap

We now correlate the time-averaged and dynamic measurements on the same particle. Whereas the time-averaged spectral ratio directly measures the com-

4.5 Temperature dependent dynamics of Brownian fluctuations in the trap

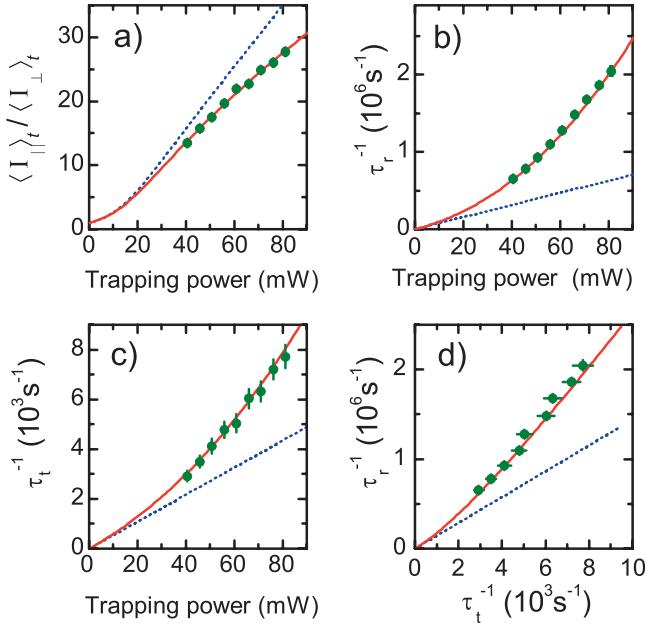


Figure 4.3: Trap characteristics as functions of trapping power, for the nanorod of figure 4.2. a) Ratio of scattered intensities of the rod's longitudinal plasmon resonance, parallel and perpendicular to the trapping laser polarization. b) Inverse of the rotation correlation time τ_r . c) Inverse of the translation correlation time τ_t . d) Inverse rotation correlation time versus inverse translation correlation time. The red lines show a global fit with an effective temperature \widetilde{T}_B deduced from (a) and effective viscosities for translations $\widetilde{\eta}_t$ from (c) and rotations $\widetilde{\eta}_r$ from (b). The blue dotted lines would be observed in the complete absence of heating. In d), the blue dotted line follows from taking the same effective viscosity for rotation and translation, $\widetilde{\eta}_r = \widetilde{\eta}_t$.

petition between the trap energy and the thermal fluctuations, the rotational correlation time probes the temperature-dependent viscosity. Fig. 4.3 shows these two quantities for the same nanorod, versus trapping power. The plot of the intensity ratio $\langle I_{\parallel} \rangle_T / \langle I_{\perp} \rangle_T$ versus trap intensity in Fig. 4.3(a) shows a distinct downward curvature, which we attribute to an increase of local temperature with trap power. Indeed, the optical restoring torque on the nanorod competes with stronger thermal fluctuations as the rod gets hotter. Similarly, the plots of the inverse rotational and translational times $1/\tau_r$ and $1/\tau_t$ in Fig. 4.3(b) and Fig. 4.3(c) show an upward curvature because of the reduced water viscosity at higher trap powers.

The Brownian motion of the hot nanorod takes place in an inhomogeneous temperature- and viscosity profile. Heat diffusion being much faster

than molecular diffusion, the temperature profile accompanies the particle in its motion.⁹⁰ We describe these fluctuations phenomenologically by means of an effective temperature and of effective viscosities, as proposed recently for translational diffusion of a hot free particle.⁹⁰ This Hot Brownian Motion (HBM) has an effective temperature T_{HBM} close to the average $(T_p + T_0)/2$ between the particle temperature T_p and the bath temperature T_0 , and an effective viscosity η_{HBM} . Here, we introduce another effective viscosity for the rotational HBM. This new parameter is needed because the plot of the rotational inverse time versus the translational inverse time (see Fig. 4.3(d)) is strongly nonlinear, indicating that these two effective viscosities must be different (see further data from other rods in Appendix H). Indeed, taking the same effective viscosity for both translations and rotations would lead to the straight dotted line in Fig. 4.3(d), with slope $B\kappa_r/\kappa_t$ (B depending only the shape and size of the particle under study).

To find the effective temperatures and viscosities, we globally fitted the data of Fig. 4.3 and those of two other particles measured under the same conditions to a model (see Appendix H) involving an effective temperature \widetilde{T}_B and two effective viscosities $\widetilde{\eta}_r$ and $\widetilde{\eta}_t$. We adjusted the unknown parameters in the following way. The local trap intensity was obtained from the spectral intensity ratio and from the polarizability $\text{Re}\{\Delta\alpha\}$ of the three nanorods. That polarizability was calculated in the electrostatic approximation, with appropriate corrections to account for radiation damping and electron-surface scattering,^{121,138} see Chapter 3. The aspect ratio of the ellipsoid and the plasmon damping rate were adjusted for each rod to reproduce the resonance wavelength and width measured in scattering spectra, see Appendix H. The intensity in the trap and the average volume of the 3 measured rods were jointly fitted to remain compatible with the volume distribution obtained from electron microscopy.

With this local intensity and the rotational times, we adjusted the rods' hydrodynamic volumes. We calculated friction coefficients from Perrin's expressions¹²⁷ for a prolate spheroid translated along the principal axes or rotated around a short principal axis, see Appendix D. The fitted effective hydrodynamic volume accounts for the PEG layer (effective thickness 5 nm¹³²). The effective temperature \widetilde{T}_B was fitted by the intensity ratios and found to be close to the particle's temperature T_p calculated independently from the trap intensity. The effective translational viscosity was taken as η_{HBM} , whereas the rotational effective viscosity was varied to fit the temperature dependence of rotational times in Fig. 4.3. The viscosity $\widetilde{\eta}_r$ found was close to its maximum

possible value, water's viscosity at the particle's temperature. The trap intensity found at the nanorod position was about 50% of the value expected for the focus of a diffraction-limited spot with the effective numerical aperture of 1.0 and the measured objective transmission of 19%. We attribute this low value to residual spherical aberrations.

4.6 Discussion

It is reasonable that the effective temperature \widetilde{T}_B of the orientation distribution should be close to the particle's temperature T_p . Indeed, the particle should be in thermal quasi-equilibrium with the liquid shell around it. The effective translational viscosity $\widetilde{\eta}_t$ should be close to that of the Hot Brownian Motion, because our fat rod closely resembles a sphere. The difference in effective viscosities for the rotational and translational Brownian motions, however, is a surprise. Although rotations occur on much shorter times (microseconds) than translations (milliseconds), inertial effects appear too weak to explain this difference. We note that the amplitude of the rotational motion, less than 10 nm for the tip in a rotation of 20 degrees, is much smaller than the amplitude of the translational motion. The difference in viscosities may thus arise from the PEG brush, which must follow the rod's translation but not necessarily its rotation.

Our model yields a temperature increase of the rod in the trap of about 70 K at the highest trapping power of 80 mW, or about 0.9 K/mW. This value is fairly well reproduced by a simple model taking into account the fitted trap laser intensity, the calculated absorption cross section (electrostatic approximation) and heat dissipation (see Appendix H). Similar heating rates were previously found for gold spheres.^{77,88} Such temperature rises may be of concern for certain applications. However, the temperature around the nanorod decays rapidly with distance, with a characteristic length of the order of the particle's radius. At a distance 100 nm away from the rod, the temperature increase is only about 10 degrees (See Appendix G) for the highest trapping power used here.

4.7 Conclusions

We have determined for the first time the torque that can be exerted on a single gold nanorod in a polarized optical trap. The maximum torque we measured was 100 pN·nm, large enough to address typical single-molecule

4 *Brownian fluctuations and heating of an optically aligned gold nanorod*

processes.¹³⁷ The small volume of a single gold nanorod compared to conventional dielectric particles paves the way to study environments which exhibit mechanical heterogeneity on nanometer length scales.

5

Measuring the temperature of a single metal nanoparticle by changes of the plasmon spectral width

In this chapter we present preliminary results on the temperature dependence of the spectral width of the plasmon resonance of a single gold nanoparticle, and its use to measure the temperature of the particle.

5.1 Introduction

In a wide variety of experiments, it is interesting to locally measure temperatures with a local temperature probe.^{139–141} The range of operation temperatures, the accuracy of the temperature determination, and the temporal and spatial resolution determine the range of application for each given temperature probe. The use of nano-objects as thermometers is promising due to their small size and short thermal relaxation times, enabling both high spatial and temporal resolution.

In optical experiments on metal nanoparticles it is often required to estimate the temperature of a particle that is heated by absorption of the illumi-

nation light. Commonly, the temperature increase of an illuminated nanoparticle is estimated from a calculation of the power absorbed by the particle and the dissipation of heat into the particle environment, as given by Fourier's law of heat conduction. However, in practical experiments at least one of the required parameters –the absorption cross-section of the particle, the local illumination intensity, the particle radius or the thermal conductivity– is often not accurately known, resulting in large uncertainties in the temperature estimation.

To obtain more reliable estimates of particle temperature, various methods have been developed that measure the particle temperature indirectly, by characterization of some physical property of the environment of the particle. Examples come from optical trapping, where a particle temperature can be inferred from the scaling of the amplitude of Brownian fluctuations with trapping power,^{77,142} as presented also in Chapter 4. Recently, an elegant approach was presented by Bendix *et al.*,⁸⁸ who used the known temperature of a melting transition in a lipid bilayer to probe the temperature profile around a trapped particle. The hot region of the membrane close to the particle could be identified by fluorophores that favored one of the membrane phases. Baffou *et al.*¹⁴⁰ have used the polarization anisotropy of fluorescent dye molecules to probe the temperature around metal nanostructures. However, the need for an optical trap, a lipid membrane or fluorescent dyes limits the range of applications of these approaches. To have a temperature sensor that can be used in the same way in a variety of experimental configurations, a temperature-dependent optical effect of the particle itself is desirable.

Here, we set out to explore the possibility to measure the temperature of single gold nanoparticles from temperature-induced changes of the width of their plasmon resonance. The idea is that the temperature dependence of the damping of a plasmon excitation is known accurately. When contributions from interband transitions can be neglected, as is the case for gold nanorods with a longitudinal plasmon resonance below $\approx 2\text{eV}$, the temperature dependence of the plasmon relaxation γ rate is determined by the temperature dependence of electron-phonon decay rate in the metal. Around room temperature (well above the Debye temperature of the metal), the decay rate increases linearly with temperature, a convenient feature for a thermometer. The plasmon relaxation rate $\gamma(\omega)$ at a frequency ω is observed experimentally as the spectral linewidth $\Gamma(\omega)$ of the plasmon resonance. Scattering spectra of individual gold nanoparticles can be readily measured with relatively simple equipment. As the only experimental restriction is that a scattering spectrum can be measured, the method would be applicable to variety of experimental

configurations.

In this chapter, we present two novel single-particle approaches to test whether the changes of the spectral width can serve as a single-particle thermometer. First we calibrate the method on immobilized gold nanorods in a temperature-controlled sample chamber, where temperature is varied in a range 290 K-340 K. Secondly, we apply the method to optically trapped gold nanorods, an example of an experimental system where temperature is an important parameter that is difficult to estimate.

5.2 Experimental

The experimental setups used for the two approaches to study the temperature dependent plasmon damping are shown in Fig. 5.1.

Experiments on immobilized particles are performed with a metal sample holder that can be brought to a controlled temperature by means of circulating water heated by a laboratory temperature controller, Fig. 5.1 (a-b). The temperature of the metal chamber is measured by a temperature sensor (platinum resistor) inserted in the center of the chamber. Two coverslips separated by immersion oil are clamped to the sample holder with a metal ring that is in good thermal contact with the chamber, to assure a constant temperature over the region between the temperature sensor and the gold nanoparticles. The metal sample holder is mounted on a piezo-scanner to enable three-dimensional positioning with nanometer accuracy. The chamber is thermally isolated from the scanner to minimize thermal drifts and prevent scanner damage. In the experiment single particles are followed over a temperature range of 50 K. Over this range, the residual thermal drift in the microscope is still several tens of microns, large enough for the nanoparticles under study to completely drift out of the microscope's field of view. To follow single particles over the complete temperature range, the temperature of the sample chamber was changed in small steps (≈ 2 K) and thermal drifts were compensated by manually adjusting the piezo-scanner to keep the particle in focus.

The optical trap setup shown in Fig. 5.1 (c-d) is as previously described in Chapter 3. Briefly, an infrared cw beam (wavelength 1064 nm) is focused by a NA = 1.4 oil immersion objective, about 25 μm into water in a home built flow cell.

Gold nanorods were synthesized by silver-assisted seed-mediated growth in the presence of hexadecyltrimethylammonium bromide (CTAB).¹¹⁹ The

5 Measuring the temperature of a single metal nanoparticle by changes of the plasmon spectral width

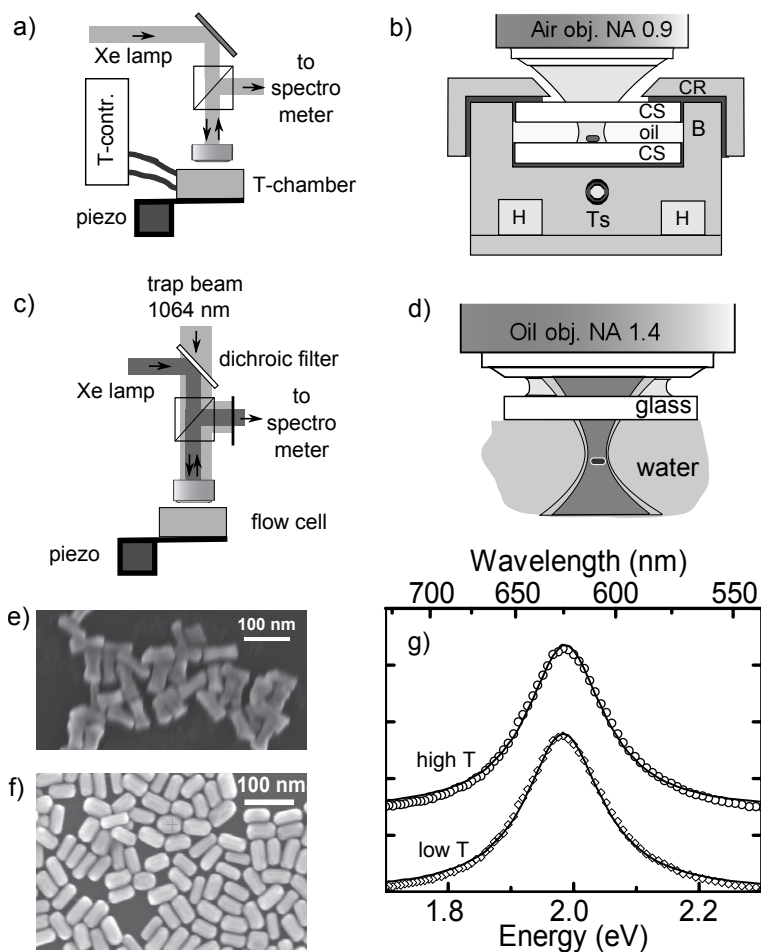


Figure 5.1: Schematic overview of the two experimental approaches to study the temperature dependence of plasmon damping. a) Schematic of the setup to record white light scattering spectra of single gold nanoparticles immobilized on a glass substrate, in a temperature controlled chamber. b) Detail of the chamber. CS, cover-slip; B, metal heater block; CR, metal clamp; H, heater channel with water flow from T-controller; Ts, temperature sensor. c) Schematic of the optical trapping setup. d) Detail of the trap focus in the flow cell. e) Gold nanorods (33 nm width, 74 nm length) used for the experiments on immobilized particles. f) Gold nanorods (25 nm width, 60 nm length) used in the optical trapping experiments. d) Typical scattering spectra of an optically trapped gold nanorod, showing the longitudinal plasmon resonance. The two spectra were taken at the maximum (high T, open circles) and minimum (low T, open diamonds) trap power, and are offset for clarity. The spectra are very similar, but the Lorentzian fits (solid lines) resolve a small broadening and blue-shift of the high temperature spectrum, with respect to the low temperature spectrum.

experiment with immobilized particles was performed with gold nanorods (33 nm mean diameter by 74 nm mean length) that were coated with (3-Mercaptopropyl)trimethoxysilane (MPTS, Sigma-Aldrich) following Liz-Marzán *et al.*¹⁴³ to increase the thermal stability of the nanorod. A sample with single well-separated rods was obtained by spin-coating on a microscope coverslip. The experiments in the optical trap were performed with gold nanorods of 25 nm mean diameter and 60 nm width. These nanorods were coated with thiolated polyethyleneglycol (PEG, $M_W = 5\text{kDa}$, Sigma Aldrich) coated to prevent their aggregation in pure water.¹²⁰ The rod suspensions were diluted by several orders of magnitude to prevent the trapping of multiple particles during a measurement. White light scattering spectra were measured as previously described in Chapter 3: the rods were excited with unpolarized light from a Xe-lamp, and backscattered light from the rods was detected through a pinhole. For immobilized particles, no polarizer was placed in the detection path.

5.3 Modeling of plasmon damping

We briefly review the mechanisms responsible for damping of a plasmon excitation in a gold nanoparticle, with a focus on their temperature dependence. A more in-depth treatment has been given by, for example, Liu *et al.*¹²³

The total damping rate γ of a plasmon excitation in a metal nanoparticle is determined by damping rate γ_b due to mechanisms present in the bulk metal plus a rate γ_{np} due to damping mechanisms present in nanoparticles only, via

$$\gamma = \gamma_b + \gamma_{np} \quad (5.1)$$

In the bulk metal, the plasmon relaxation rate is the sum of a decay rate γ_{e-e} due to electron-electron scattering and the electron-phonon scattering rate γ_{e-p} :

$$\gamma_b = \gamma_{e-e} + \gamma_{e-p}(T). \quad (5.2)$$

Of the two mechanisms, only γ_{e-p} depends significantly on temperature.¹²³ The electron-phonon scattering is calculated by considering a free electron gas and a Debye model for phonons. In the absence of interband transitions the damping rate is given by¹²³

$$\gamma_{e-p}(T) = \hbar\tau_0^{-1} \left[\frac{2}{5} + 4 \left(\frac{T}{\Theta} \right)^5 \int_0^{\Theta/T} \frac{z^4}{e^z - 1} dz \right] \quad (5.3)$$

5 Measuring the temperature of a single metal nanoparticle by changes of the plasmon spectral width

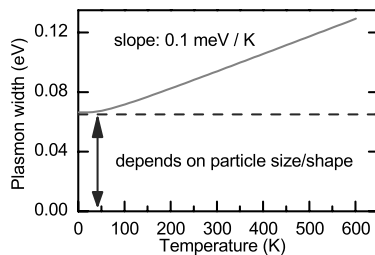


Figure 5.2: Calculated plasmon damping as a function of temperature, following the model of Liu *et al.*¹²³ In the absence of interband transitions, the temperature dependence is determined by the temperature dependence of electron-phonon coupling only. At room temperature and above, it varies linearly with temperature.

where τ_0 is a material-dependent constant, and Θ is the Debye temperature. Eq. 5.3 is derived in the limit $E_F \gg \hbar\omega \gg k_B T$ and $k_B \Theta$, with E_F the Fermi energy. These requirements are satisfied for gold at plasmon energies around 2 eV. For gold, $\tau_0 = 30$ fs and $\Theta = 185$ K.¹⁴⁴

The bulk damping rate γ_B evaluated with Eq. 5.3 for gold, and the expression for γ_{e-e} taken from Liu *et al.*¹²³ is shown in Fig. 5.2. At room temperature and above, the damping increases almost linearly with temperature, with a slope 0.1 meV/K.

In nanoparticles, radiation of the plasmon forms an extra damping mechanism with a rate γ_r , independent of temperature at optical frequencies.¹²³ In addition, the bulk electron scattering rate has to be modified to take into account electron surface scattering, contributing a rate γ_S , also temperature independent. Both radiative damping and electron surface scattering depend on the particle radius R , varying as R^3 and $1/R$ respectively. The plasmon width thus varies with particle size. However, within the limits of our model the temperature dependence of the plasmon width results only from the temperature dependence of the electron-phonon scattering rate, which is independent of particle size. The temperature-induced change of the plasmon width, which increases linearly with temperature with a known proportionality constant, can serve as a thermometer.

Experiments on ensembles of immobilized gold bipyramids¹²³ have confirmed the dominant role of electron-phonon scattering in the temperature dependence of the damping of the plasmon resonance of the nanoparticles, and were in quantitative agreement with the above model. A question remains how accurately the parameter τ_0 describes different samples or different individual particles within a sample. The parameter τ_0 is normally

obtained from the infrared absorption of bulk metals. As reviewed by Winsemius,¹⁴⁵ the infrared absorption of metals has been shown to vary with crystal structure, concentration of defects or impurities and surface roughness.^{146–149}

We emphasize that the above modeling holds only in the absence of interband transitions. When the contribution of interband transitions cannot be neglected, the modeling needs to be re-evaluated. Although the modeling may be more involved than for the case of intraband transitions, the temperature dependence of interband transitions is known,¹⁵⁰ and may thus also serve as a thermometer. Such an analysis may be then be used to evaluate the temperature dependence of plasmon damping in spherical gold nanoparticles. For these particles, the contribution of interband transitions can not be neglected, as the plasmon resonance occurs around 2.4 eV, in the region of interband transitions. For the longitudinal plasmon resonance of the gold nanorods used in this Chapter, with resonance energy < 2 eV, the contribution of interband transitions is still small, so that the above modeling applies.

5.4 Results and discussion

5.4.1 Temperature dependence of the plasmon width of immobilized gold nanorods

Figure 5.3 displays the results obtained on immobilized single gold nanorods in a temperature- controlled sample chamber. Scattering spectra as in Fig. 5.1 (g) were recorded for a number of single gold nanorods at a given temperature. A series of such measurements were made from room temperature upwards to 340 K and then downwards back to room temperature. Panel a) and b) show a typical spectral width (full width at half maximum, FWHM) and resonance energy observed in a measurement series on a single gold nanorod, obtained from Lorentzian fits of the measured scattering spectra .

A broadening of the plasmon resonance as a function of temperature is clearly observed in Fig. 5.3 a). Note that the change of the plasmon width is not large compared to the plasmon width itself; over the full temperature range the plasmon width changes by less than 3 percent. However, changes of this magnitude are easily resolved from the fits of the scattering spectra, due to the high signal-to-noise. A small anomaly to the overall trend is seen in the first three acquired data points –at the lowest temperatures of the upwards series– displaying a plasmon narrowing with increasing temperature. This effect is not reproduced in the downward measurement series that was

5 Measuring the temperature of a single metal nanoparticle by changes of the plasmon spectral width

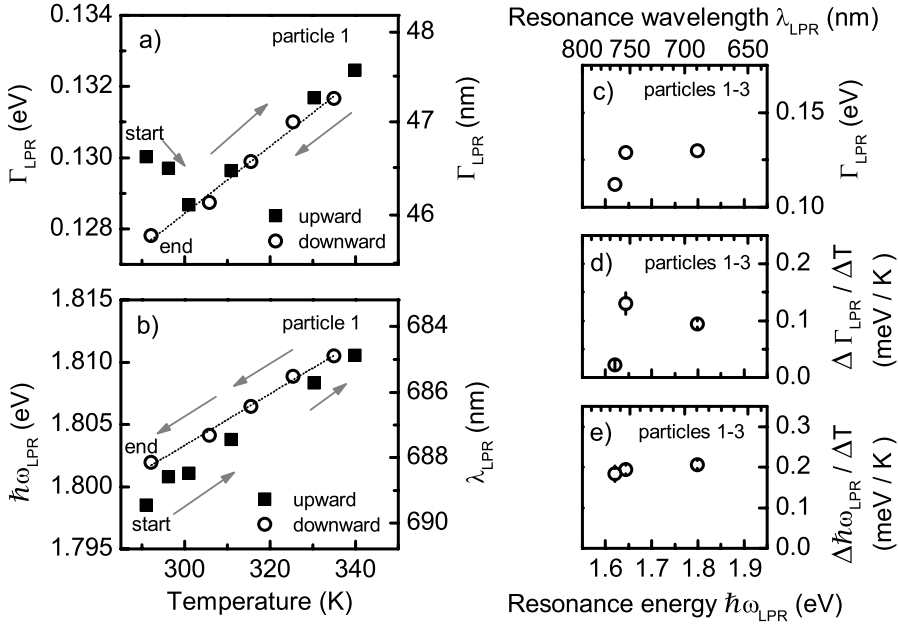


Figure 5.3: Temperature dependence of the longitudinal plasmon resonance of single gold nanorods, immobilized on a glass substrate and surrounded by immersion oil. (a) Width Γ_{LPR} and (b) energy $\hbar\omega_{LPR}$ of the longitudinal plasmon resonance of an individual gold nanorod. Data was taken first going upwards in temperature, then downwards back to room temperature at 290 K. The dotted lines are linear fits of the data from the series downwards in temperature. (c-e) Measured temperature dependence of the plasmon for the nanorod in (a-b), plus two additional rods, as a function of the longitudinal plasmon resonance energy $\hbar\omega_{LPR}$ of the rods. Panel (c): Width Γ_{LPR} (at 290 K) of the rods. Panels (d) and (e) display respectively the temperature dependence of the plasmon width and energy, obtained from the slopes of the linear fits as in (a-b).

acquired subsequently, indicating that an irreversible change to the particle may have occurred. An explanation of this change could be the removal of part of the MPTS capping layer of the rod, diminishing the effect of chemical interface damping on the particle. Independently of the origin of such irreversible changes, over the complete series a temperature-induced broadening is robustly observed: the linear temperature dependence of the plasmon width is identical in both upward and downward measurement series, within experimental error. The measured temperature-induced broadening is 0.1 ± 0.01 meV/K. This value is good agreement with the value of 0.1 meV/K

that is expected in the absence of inter-band transitions, due to the increase of electron-phonon scattering rate with temperature.

Similar results were obtained on two other single gold nanorods, as summarized in Fig. 5.3 (c-e). On all three nanorods a temperature-induced broadening is observed, see Fig. 5.3 d). However, while for two of the gold nanorods the temperature-induced broadening is around the expected value of 0.1 meV/K, on one of the rods the broadening is much smaller. The reason for this deviation is currently not understood.

The experiment on immobilized particle shows that the temperature-induced broadening of the plasmon resonance can be measured on a single gold nanoparticle. The experimentally measured broadening is close to the value expected if the temperature dependence of plasmon damping is determined by electron-phonon scattering only. However, the quality of our experiment is as yet good not enough to serve as an accurate calibration of our proposed method as single particle thermometer. We expect to be able to improve the quality of our calibration experiment by performing measurements on more individual particles. To test the validity of the method more thoroughly, experiments should be repeated for rods with a broader range of aspect ratios, thus probing a range of plasmon energies. Additionally, it will be instructive to perform measurements on gold spheres, to quantify the influence of interband transitions on the temperature dependence of plasmon damping.

We end our discussion by observing that all three investigated particles display a temperature-induced blue-shift of the plasmon energy, see Fig. 5.3 e). As the effect is accurately observed –the detected blue-shift is within experimental error the same on all particles– it may seem an attractive alternative to exploit as thermometer. However, we believe that the temperature dependence of the plasmon energy is not suitable as a thermometer, because the shift may vary for different experimental conditions, and is difficult to model. The reason is that several effects of different physical origins shift the plasmon as a function of temperature. Thermal expansion causes a red-shift of the plasmon, due to a lowered electron density. Most dielectric media display a lowering of the refractive index with increasing temperature, causing a blue-shift of the plasmon. The temperature dependence of the refractive index of the medium surrounding the particles is not always known.

5.4.2 Temperature dependence of the plasmon width of optically trapped gold nanorods

The optical trapping of gold nanoparticles is an example of a class of experiments where the particle temperature is an important parameter that is difficult to estimate accurately.

Before discussing our experimental results on optically trapped particles, it is instructive to consider how the difficulty in the temperature estimation arises. Although some of the encountered difficulties are specific to optical trapping only, similar issues are met frequently in optical microscopy experiments on metal nanoparticles.

Heating of the particles in the optical trap is induced by absorption of the trap laser. The temperature increase ΔT of a trapped nanorod is given by Fourier's law of heat conduction. Specifically, for the case of a spherical particle with a thermal conductivity much higher than that of the environment, the temperature is given in steady-state by the expression

$$\Delta T = \frac{I\sigma_{\text{abs}}}{4\pi RK_m}, \quad (5.4)$$

where σ_{abs} is the absorption cross-section at the trap wavelength, I is the local intensity of the trap laser, R is the radius of the sphere and K_m is the thermal conductivity of the medium. The heat dissipation of nanorods of moderate aspect ratio (smaller than 5) can be well approximated by the heat dissipation of a sphere with the volume of the rod, see Appendix G.

In optical trapping experiments, single nanoparticles are selected at random from a given sample. The inevitable distribution of particle sizes and shapes in the ensemble results in a distribution of absorption cross-sections σ_{abs} and radii R of the trapped particles, leading to uncertainty in the evaluation of Eq. 5.4.

An additional complication arises because the local intensity of the trap is difficult to determine accurately in the experiment. The local intensity is normally obtained from calculation, by assuming a diffraction limited focal spot for a certain numerical aperture. However, the wavelengths typically used in optical trapping are in the near-infrared, far from the visible region for which most commercial high-numerical-aperture objective are designed. The aberrations that result can enlarge the focal spot and significantly lower the local intensity. In addition, in some cases spherical aberrations are introduced due to the refractive index mismatch of coverslips and the liquid medium, as encountered in Chapters 3 and 4. These aberrations can be compensated in various ways^{118,151} and/or quantified experimentally, but obtaining an accurate

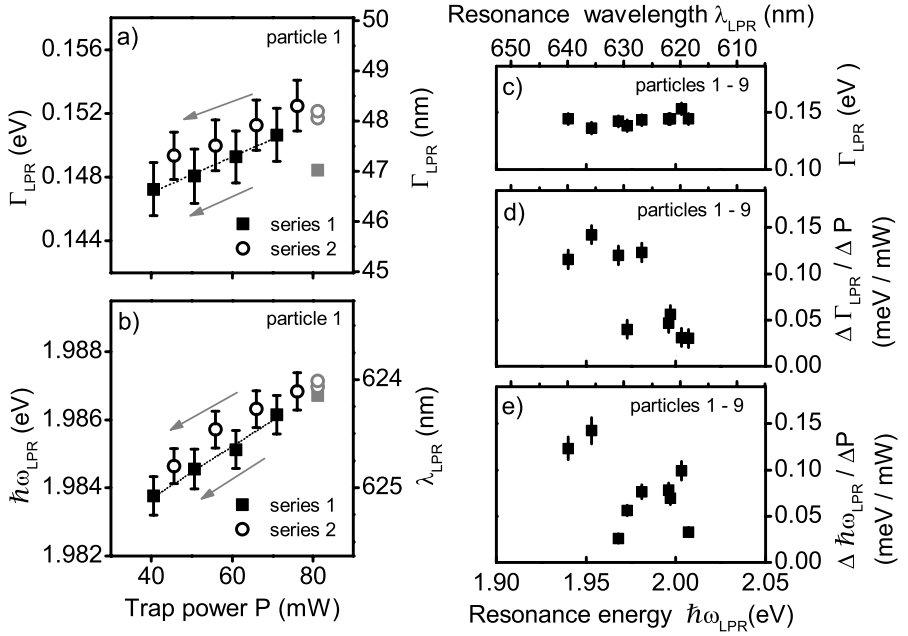


Figure 5.4: Temperature dependence of the plasmon resonance of single optically trapped gold nanorods in water, via laser-induced heating of the rods. A typical result obtained on a single trapped nanorod is shown in panels (a) and (b), displaying the width and energy of the rod as functions of trapping power. Black solid squares and black open circles are two consecutive measurement series on the same nanorod, taken going downward in trapping power. Grey solid squares and grey open circles indicate the plasmon width and energy before the start of the corresponding measurement series. Dotted lines are linear fits to the first series 1 with slopes $(1.0 \pm 0.09) \cdot 10^{-4} \text{ eV/mW}$ (a) and $(0.8 \pm 0.1) \cdot 10^{-4} \text{ eV/mW}$ (b), respectively. (c-e) Temperature dependence the plasmon resonance obtained from linear fits to the data as presented in panel (a-b), for 9 single trapped gold nanorods. The data are plotted as functions of the rods' longitudinal plasmon resonance energy. Panel (c): Width of plasmon resonance of the rods at zero trap power. Panels (d) and (e) display respectively the variation of plasmon width and energy with trapping power.

determination of the absolute value of the local intensity remains challenging.

In Fig. 5.4 we examine the temperature dependence of the plasmon resonance of single gold nanorods in an optical trap. Here, the temperature of the rods is controlled indirectly by variation of the trapping power. Figures 5.4 (a) and (b) show a typical result obtained on a single gold nanorod in the op-

5 Measuring the temperature of a single metal nanoparticle by changes of the plasmon spectral width

tical trap. As expected, we observe a broadening of the longitudinal plasmon resonance of the particle as the trapping power is increased, see Fig. 5.4 (a). The figure displays two series of measurements on the same gold nanorod. The data points in each series were taken within about 2 minutes, whereas the two series were separated in time by about 10 min. In the second series a small overall broadening of the plasmon is seen. The reason for this increased plasmon damping is not clear. Significant reshaping is excluded, as the longitudinal plasmon resonance remains at its initial value to within 0.1%. The small additional damping may be related to thermally induced changes of the structure of the particle, for example an increased surface roughness. The slope of the lines is $1.0 \pm 0.1 \cdot 10^{-4}$ eV/mW. According to the calculation in section 5.3, this corresponds to a temperature increase of 1 K/mW. This is close to the value of 0.9 K/mW found for this particular rod in the measurements of Brownian fluctuations presented in Chapter 4.

We measured a number of individual gold nanorods in the trap. As seen in Fig. 5.4 (c-d), all particles qualitatively displayed the same behavior as observed for the rod in Fig. 5.4 (a-b). On average, the rods with a longer longitudinal plasmon resonance wavelength (larger aspect ratio) display a larger increase of the plasmon width as function of trapping power. This is expected, as the resonance wavelength of these rods is closer to the trap wavelength, resulting in larger absorption cross-sections and higher temperatures. The spread of values in Fig. 5.4 d) indicates that different particle temperatures occur at a given trap power and rod aspect ratio (or resonance wavelength). This spread is most likely due to the spread in volumes of the particles in the sample.

We end our discussion by noting that in the analysis of the scaling of trap parameters as a function of trap power in Chapter 4, we have assumed a linear dependence of the temperature increase with trapping power. With a thermally induced broadening of the particle's plasmon resonance, this assumption no longer strictly holds. However, we note that the temperature-induced broadening is small, resulting in a plasmon broadening of less than 5 percent between zero and maximum trap power. A broadening of this magnitude is not expected to qualitatively change any of the previously obtained results, although some of the obtained values may be altered in a minor way.

5.5 Conclusions

We have presented an experimental study of the temperature dependence of the plasmon resonance in single gold nanoparticles, motivated by the possible use of temperature-induced broadening of the plasmon as a thermometer. We have investigated immobilized single gold nanorods in a calibrated temperature chamber, and gold nanorods in an optical trap. In all experiments, a broadening of the plasmon is observed when temperature is increased, and the amount of broadening is close to the expected value. However, a distribution of responses is observed for different single immobilized nanorods for the same temperature increments. As this behavior is not yet understood, the validity of the proposed method as thermometer remains to be proven.

6

Acoustic vibrations of single gold nanoparticles optically trapped in water

Abstract – We combine ultrafast pump-probe spectroscopy with optical trapping, to study homogeneous damping of the acoustic vibrations of single gold nanospheres (80 nm diameter) and nanorods (25 nm diameter by 60 nm length) in water. We find a significant particle-to-particle variation in damping times. Our results indicate that vibrational damping occurs not only by dissipation into the liquid, but also by damping mechanisms intrinsic to the particle. Our experiment opens the study of mechanisms of intrinsic mechanical dissipation in metals at frequencies 1-1000 GHz, a range that has been difficult to access thus far.

The contents of this chapter are based on:
P. V. Ruijgrok, P. Zijlstra, A. L. Tchebotareva and M. Orrit, “Damping of acoustic vibrations of single gold nanoparticles optically trapped in water”, *Nano Lett.* **12**, 1063 (2012)

6.1 Introduction

Acoustic vibrations of nanometer scale objects provide fundamental insight into the mechanical properties of matter. Moreover, the sizes, shape and crystallinity of the nanoobjects can be controlled and their effect on the mechanical properties investigated.¹⁵² Of particular interest are noble metal nanoparticles, that interact strongly with light due to a collective oscillation of their conduction electrons. This oscillation is known as a surface plasmon resonance, and its energy and linewidth depend on particle composition, size, shape and environment. Due to this strong interaction, acoustic vibrations can be excited and detected with far-field optical techniques^{153–156} down to very small particles sizes (~ 1 nm) and high vibration frequencies (~ 1 THz).¹⁵⁷ Besides fundamental interest, knowledge about mechanical properties of nanoparticles is important for applications where vibrating nanostructures are employed as ultra sensitive mass sensors.^{158–161} For these applications often low damping is desired.

In experimental studies on nanoparticles thus far it has been particularly difficult to extract information about damping of mechanical vibrations. Most experiments have been performed on ensembles of particles,³⁶ resulting in an inhomogeneous broadening that dominates the observed damping time. This broadening arises because even the best synthesis methods produce samples with a distribution of sizes and shapes and therefore a distribution of vibration frequencies. In some very specific cases, ensemble-averaged homogeneous damping times have been extracted from measurements,^{162,163} but these experiments require assumptions on how the ensemble-averaged optical response is related to the width and form of the distribution of particle sizes and shapes. Recently, it has been demonstrated that mechanical vibrations can also be observed for individual metal nanoparticles immobilized on a substrate, by performing pump-probe spectroscopy with the nanoparticles in the focal spot of a high numerical aperture microscope objective.^{164–173} As inhomogeneous broadening is absent in these experiments, the homogeneous damping times are directly observed and were found to be significantly longer than the damping times observed in ensemble experiments. Single-particle experiments consistently show a large particle-to-particle variation of damping times, that has been attributed to variations in the mechanical coupling of the individual nanoparticles to the environment.^{165,167–169,173} Quantitative comparison to theory in this geometry remains challenging, as the local environment is inhomogeneous due to the presence of the substrate. Additionally, the coupling of the particle to the substrate may depend on small

variations in the particle shape and capping layer, and vary from particle to particle.

A possible approach to investigate the mechanisms of mechanical damping on the nanometer length scale is to perform measurements on single particles in a homogeneous environment that can be modeled theoretically, such as a liquid. The techniques to measure acoustic vibrations on single particles thus far were not compatible with measurements in liquid, as the particle needs to be immobilized in the focal volume of the microscope for the entire duration of the pump-probe measurement, on the order of minutes. In a liquid, however, the particle quickly diffuses out of the focal volume, typically on a millisecond timescale in water.

Here, we report on the first observations of the acoustical vibrations of single gold nanoparticles in a homogeneous liquid environment, for nanospheres of 80 nm diameter and nanorods of 25 nm diameter and 60 nm length. We confine the nanoparticle to the focal volume of a high-numerical-aperture-objective with an optical trap in water. We use an infrared single-beam trap, with a wavelength far in the red wing of the plasmon resonance of the gold nanoparticles.^{74,75} In this geometry, laser-induced heating is minimized, while the optical forces are large enough to achieve stable trapping of gold nanoparticles with diameters down to ~ 10 nm,⁷⁶ up to periods of several hours for the nanoparticles used in this study.¹⁷⁴ We measure the acoustic vibration of the nanoparticles in the optical trap with a pump-probe spectroscopy setup as done in previous single-particle experiments, with the foci of the pump and probe beams overlapped with the trap focus. We directly observe the homogeneous damping time of the vibration, which we compare to established theory for the damping of the vibrations of an elastic sphere in a homogeneous liquid environment.^{53,175–178} We consistently observe a lower quality factor of the vibration than predicted by theory. In addition, we observe a large particle-to-particle variation of the quality factor for both nanospheres and nanorods in water, similar to that previously observed for single nanoparticles on solid substrates. Our results indicate that intrinsic mechanisms within the gold nanoparticle itself are significant contributors to the damping.

6.2 Methods

Acoustic vibrations of individual nanoparticles were measured by time-resolved absorption with the ultra-fast pump-probe setup shown schematically

6 Acoustic vibrations of single gold nanoparticles optically trapped in water

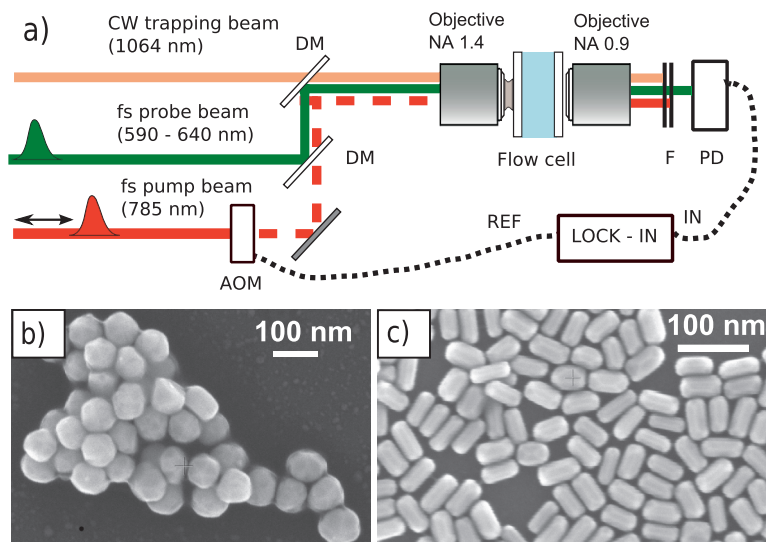


Figure 6.1: a) Schematic of the optical setup. The infrared cw trapping beam (1064 nm) is focused by a high-numerical-aperture objective into water in a flow cell, where single gold nanoparticles can be trapped for extended periods, up to several hours. Acoustic vibrations of the gold nanoparticles are investigated by a time-resolved transmission setup, consisting of femtosecond pulsed pump (785 nm) and probe (tunable 590-640 nm) beams with a variable delay, focused at the trap focus. AOM, acousto-optical modulator; DM, dichroic mirror; PD, photodiode; F, optical filters. b) Scanning electron micrograph of the gold nanospheres (80 nm diameter), and c) of gold nanorods (25 nm width and 60 nm length).

in Figure 6.1 (a), as described earlier.^{166,170} Acoustic vibrations were excited with pulses from a Ti:sapphire laser with repetition rate 76 MHz (785 nm, ~ 300 fs pulse length) and probed by the frequency-doubled output of an Optical Parametric Oscillator (tunable 590 nm - 640 nm, 350 fs pulse length). The intensity of the pump beam is modulated by an acousto-optical modulator at a frequency around 400 kHz. The transmitted intensity of the probe beam is recorded with a fast Si-PIN photodiode, and a lock-in amplifier extracts the small change of the detected probe intensity $\delta\mathcal{T}$ at the modulation frequency. We construct a vibration trace of the nanoparticle by recording $\delta\mathcal{T}(t)$ as function of the time delay t between pump and probe pulses, controlled using a mechanical delay stage. The wavelength of the probe beam is tuned to be close to the half maximum on either side of the plasmon resonance of the gold nanoparticles, where changes of the plasmon wavelength

are most sensitively observed.

The gold nanoparticles were held in water with a single-beam gradient optical trap.¹⁷⁴ The optical trap was formed by a near-infrared cw beam (1064 nm) focused by a high-numerical-aperture microscope objective, 10–20 μm away from the surface of a coverslip. To reduce spherical aberrations caused by the index mismatch between glass and water, the incoming beams were made slightly convergent.¹⁷⁴ Pump and probe foci were spatially overlapped with the trap focus by maximizing the pump-probe signal of a single gold nanoparticle. To confirm the presence of only a single rod in the trap, we recorded scattering spectra by collecting the backscattered white light from a Xenon lamp, on the CCD camera of a spectrometer.¹⁷⁴ Pump and probe pulses were kept below $10 \pm 3 \text{ pJ}$ and $0.2 \pm 0.05 \text{ pJ}$ respectively (corresponding to pulse fluences of about 4 mJ cm^{-2} and 0.2 mJ cm^{-2}). For these powers, no melting or reshaping of the nanorods was observed, as judged by a measurement of the scattering spectra before and after the measurements.

We investigated the acoustic vibrations of optically trapped nanoparticles from a sample of commercially available, roughly spherical gold nanoparticles (British Biocell International) of $80 \pm 0.7 \text{ nm}$ nominal diameter (sample standard deviation 8%) and gold nanorods with a mean length of $60 \pm 0.7 \text{ nm}$ and mean width $25 \pm 0.6 \text{ nm}$ (with sample standard deviations 8% and 16% respectively, cf. electron micrographs in Fig. 6.1 (b) and Fig. 6.1 (c)). The gold nanospheres are capped by the manufacturer with a thin organic capping layer. Gold nanorods were synthesized by silver-assisted seed-mediated growth,¹¹⁹ in the presence of hexadecyltrimethylammonium bromide (CTAB). Unless otherwise indicated, the rods were functionalized with thiolated polyethyleneglycol (mPEG, $M_W = 5 \text{ kDa}$, Sigma-Alrich) to prevent aggregation in pure water. For the experiments in the optical trap, the suspensions were diluted by 3 to 4 orders of magnitude with ultra-pure water to prevent trapping of multiple particles during the duration of a measurement, up to several hours.

6.3 Damping of acoustic vibrations of optically trapped gold nanoparticles

Acoustic vibrations of single gold nanospheres

Figure 6.2(a) shows a typical delay trace obtained on a spherical gold nanoparticle of 80 nm diameter in the optical trap. The delay trace exhibits a

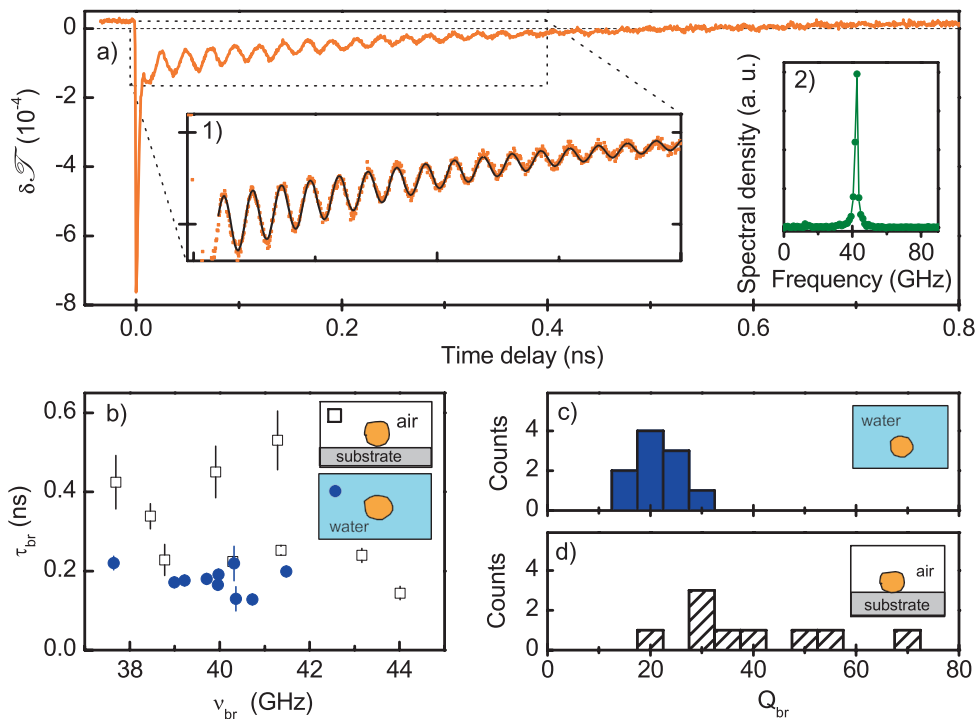


Figure 6.2: Acoustic vibrations of 80 nm diameter single gold nanospheres. (a) Trace of a single nanosphere in the optical trap in water, displaying a damped breathing mode oscillation. The probe wavelength, 595 nm, lies in the red wing of the plasmon resonance. Lock-in integration time 30 ms per point. Inset (1): Fit of eq. 6.1 to determine the frequency ν_{br} and characteristic damping time τ_{br} . Inset (2): Power spectral density of the oscillatory part of the vibrational trace. (b) Periods and damping times of the breathing mode of single particles optically trapped in water (blue solid circles) and deposited on a solid substrate (black open squares), taken on different individual particles from the same batch. (c, d): Histograms of quality factors $Q_{br} = \pi\nu_{br}\tau_{br}$ calculated from the data in (b), for the breathing mode of single gold nanospheres in the optical trap in water (c) and for particles on a solid substrate in air (d).

short-lived peak at the temporal overlap of pump and probe pulses, and a damped oscillation and slow decay on a longer timescale. The spike at short times is caused by the heating of the electron gas by the laser pulse, leading to a broadening and shift of the plasmon resonance. The energy of the electron gas is transferred to the lattice in a few picoseconds, and dissipated into the water in several hundred picoseconds. The pump laser pulse excites an acoustic vibration of the particle by two mechanisms,¹⁷⁹ first by the Fermi pressure of the hot electron gas, and second due to the thermal expansion of the heated lattice, both occurring on a timescale much shorter than the natural oscillation frequencies of the particles. The elastic vibration modes of a sphere are labeled in Lamb's theory¹⁸⁰ by two integers, n , the harmonic order, and l , the angular momentum number. As the laser-induced excitation mechanism is spherically symmetric, mainly the spherically symmetric fundamental breathing mode $(n, l) = (0, 0)$ of the sphere is excited. This mode is detected through modulation of the particle's volume, which shifts the plasmon resonance periodically. The measured delay trace displays mainly the fundamental breathing mode, seen in the Fourier transform in the inset of Figure 6.2 (a). For some particles, weak traces of higher order modes were detected (see Section 6.4, Figure 6.4). The zoomed trace in Figure 6.2 (a) displays the initial part of the oscillation, fitted with a sum of damped oscillating terms:

$$\delta\mathcal{I}(t) = A_c \exp(-t/\tau_{\text{cool}}) + \sum_k A_k \exp(-t/\tau_k) \cos(2\pi\nu_k t - \phi_k) \quad (6.1)$$

where the sum is over the number of damped oscillation modes, with characteristic decay time τ_k , frequency ν_k , phase ϕ_k and A_c and A_k are proportionality constants. For the spheres, only the breathing mode $k = \text{br}$ contributes. The near-exponential decay with characteristic time t_{cool} describes the effect of particle cooling and of the accompanying heating of the environment on the plasmon resonance of the particle.¹⁸¹ The particle's temperature should decay as $t^{-3/2}$ on long timescales because of heat diffusion in bulk water.^{182,183}

Vibration frequencies and damping times of the fundamental breathing mode of 10 individual nanospheres in the optical trap are shown as the blue solid circles in Figure 6.2 (b). The measured frequencies around 40 GHz are in good agreement with Lamb's theory for the breathing mode of an elastic sphere,⁵² with the elastic constants of isotropic bulk gold. The distribution of vibration frequencies is in good agreement with the distribution of sizes in the sample. Importantly, the observed damping times of the vibration are

6 Acoustic vibrations of single gold nanoparticles optically trapped in water

Nanoparticle	Mode	ν (GHz)	Q (measured)	Q _{fluid} (theory)		Q _{intrinsic} (calc.)
				visc.	w. o. visc.	
Sphere (N = 10)	Breathing	40 ± 0.3 (3 %)	22 ± 1.5 (17 %)	52.5	54	40 ± 4 (29 %)
	Rod (N = 7)					
	Breathing	73 ± 0.7 (3 %)	30 ± 1.5 (16 %)	50.5	54	89 ± 10 (36 %)
	Extensional	12 ± 0.2 (5 %)	19 ± 1.7 (24 %)	n.a.	n.a.	n.a.

Table 6.1: Measured quality factors Q and frequencies ν of optically trapped single gold particles in water, nanospheres (80 nm diameter) and single-crystal nanorods (25 nm diameter, 60 nm length). Calculated breathing quality factors Q_{fluid} for damping by water according to the model by Saviot *et al.*¹⁷⁸ The model includes sound radiation and damping by bulk and shear viscosities. The model is evaluated for water at 30 °C in the presence (visc.) and in absence (w. o. visc.) of viscous damping, see Table S4 Supporting Information. These values provide lower and upper bounds for Q_{fluid} in the experiment, where the water viscosity is reduced due to the elevated temperature of particle in the trap ($\approx 80 - 100$ °C). The nanorod breathing quality factor Q_{fluid} was taken equal to that of a sphere with the same breathing frequency (diameter 40 nm). The model does not apply to the extensional mode of the rods. $Q_{\text{intrinsic}}$ was calculated from 6.2, with Q_{fluid} for viscous water. Each parameter is specified by the mean \pm standard error. Values in brackets indicate the standard deviation of all single particle measurements.

more widely distributed, varying by a factor of two on the investigated particles, even though they don't interact with a substrate, and they are embedded in the same environment. To facilitate the comparison of particles with different sizes and vibration frequencies, we characterize the damping by the quality factor Q of the vibration, given as $Q = 2\pi\nu_k\tau_k/2$.^{171,184} We have plotted a histogram of quality factors obtained from the data of Fig. 6.2 (b) in Fig. 6.2 (c), where we observe an average $\langle Q_{\text{br}} \rangle = 22 \pm 1.5$. The spread in quality factors (standard deviation 17%, see Table 6.1) is largely determined by the spread in the damping times of the vibration.

Our measured quality factors can be directly compared to the theory of damping of vibrations of an elastic sphere embedded in a homogeneous isotropic elastic medium.^{53,177} In this model, the damping is attributed to radiation of sound waves into the medium surrounding the particle. The magnitude of the damping is governed by the mismatch between acoustic impedances of the particle and the environment material, given as $Z = \rho v_L$ for longitudinal plane waves, where ρ is the material density, and v_L is the longitudinal speed of sound. For the breathing mode of a gold sphere in water, this theory predicts a quality factor $Q = 54$.¹⁷⁷ This value is significantly larger than the experimentally observed values, indicating that additional damping

6.3 Damping of acoustic vibrations of optically trapped gold nanoparticles

mechanisms are present. We have estimated the effect of viscous damping for the breathing mode vibration of a gold particle of 80 nm diameter following the calculation of Saviot *et al.*¹⁷⁸ and found a minor correction, yielding $Q_{\text{fluid}} = 52.5$ (see Table 6.1) for the overall quality factor expected in water.

The large difference with the measured Q indicates that other dissipation mechanisms intrinsic to the particle are at work, e.g., dissipation in the organic capping layer covering the particles, or internal friction due to the anelastic properties of gold itself. The total damping rate will be the sum of the damping rates due to the various mechanisms, so that the total quality factor Q can be written as

$$Q^{-1} = Q_{\text{fluid}}^{-1} + Q_{\text{intrinsic}}^{-1} \quad (6.2)$$

where $Q_{\text{intrinsic}}$ represents all intrinsic damping mechanisms. Here, Q_{fluid} can be reliably estimated, because the particles are embedded in a well defined homogeneous environment. From the average measured quality factor $\langle Q_{\text{br}} \rangle$ and the calculated $Q_{\text{fluid}} = 52.5$, we find from our experiment $\langle Q_{\text{intrinsic}} \rangle = 40 \pm 4$.

In our experiment we find not only the average damping rate, but also the variation from particle to particle, providing valuable information on the damping mechanisms on the nanoscale. In particular, the broad distribution of quality factors (we find $16 < Q_{\text{br}} < 28$) indicates that those dissipation mechanisms are sensitive to particle-to-particle structure variations, as opposed to mechanisms sensitive mostly to bulk material properties of the particles. Taking $Q_{\text{fluid}} = 52.5$, the lowest and highest measured quality factors in the experiment correspond to $23 < Q_{\text{intr}} < 60$, respectively.

To relate our results on single gold nanoparticles trapped in water to measurements performed on single particles on a substrate,^{165,167–169,173} we compare to previous measurements from our group¹⁷⁰ on the breathing mode of single 80 nm gold nanospheres supported on a solid substrate, surrounded by air, see Fig. 6.2 (b, d). Again, a broad distribution of damping times was found, resulting in a distribution of quality factors ranging from 20 to about 70, with a mean $\langle Q_{\text{br}} \rangle = 33 \pm 5.3$ (standard deviation 40 %). Interestingly, the average quality factor for particles on a substrate in air is higher than for those trapped in water. Moreover, we note that both the average value $\langle Q_{\text{br}} \rangle$ and its distribution are close to the values of $Q_{\text{intrinsic}}$ deduced for particles in water (see Table 6.1). This observation suggests that the gold nanospheres in air are only weakly coupled to the solid substrate, and that the observed damping time is dominated by intrinsic damping. Therefore, our results suggest a new interpretation of the broad distributions of damping times observed consis-

tently in all single-particle measurements to date. These distributions reflect inhomogeneity in intrinsic dampings, rather than variations in mechanical coupling to the substrate.

Acoustic vibrations of single gold nanorods

Whereas gold nanospheres may have a variety of crystal structures - single crystalline, multiple twinned or irregular¹⁸⁵⁻¹⁸⁷ - gold nanorods synthesized by seed-mediated growth in the presence of silver ions are known to be single crystals, with a growth direction along the [100] direction.¹⁸⁸⁻¹⁹⁰ If damping mechanisms related to crystal defects or grain boundaries contribute dominantly to the intrinsic damping, we expect to observe higher quality factors for single crystal rods than for polycrystalline spheres.

A representative vibration trace of an optically trapped single gold nanorod is shown in Figure 6.3 (a). Two oscillation modes are detected, as highlighted in the Fourier transform of the trace in the inset, and attributed to the breathing (about 75 GHz) and extensional (about 10 GHz) modes.¹⁹¹ The breathing mode involves radial expansion and depends on both the bulk and shear elasticity moduli, whereas the extensional mode involves an axial expansion combined with a radial contraction, and probes the Young's modulus along the long axis of the rod.¹⁹¹

The frequencies and damping times of the breathing and extensional modes of 7 nanorods in the optical trap are shown in Fig. 6.3 (b)-(c). For comparison, we also plotted the measured frequencies and damping times of single nanorods of similar sizes and aspect ratios immobilized on a clean silica substrate in air, from previous work.¹⁶⁶ For the nanorods in water, the frequency ratio of the two vibration modes is strongly correlated to their aspect ratio deduced from the measured longitudinal plasmon resonance resonance (See Section 6.5, Fig. 6.5).

The quality factors of the breathing and extensional modes are shown in the scatter plot Fig. 6.3 (d). The average quality factor of the breathing mode measured on the trapped nanorods is $\langle Q_{br} \rangle = 30 \pm 1.5$. We expect that the damping rate of the breathing mode due to radiation of sound waves for our short aspect ratio nanorods will be close to the value predicted for spheres. We therefore estimate $Q_{fluid} = 50.5$ by calculating the damping for a sphere with the same vibration frequency as the rods, see Table 6.1. Using this value we find $\langle Q_{int} \rangle = 84 \pm 10$, indeed significantly higher than for spheres. The Q -factors we find for gold nanorods suggest that crystal structure is an important factor in the intrinsic damping. The extensional mode of the rods has

6.3 Damping of acoustic vibrations of optically trapped gold nanoparticles

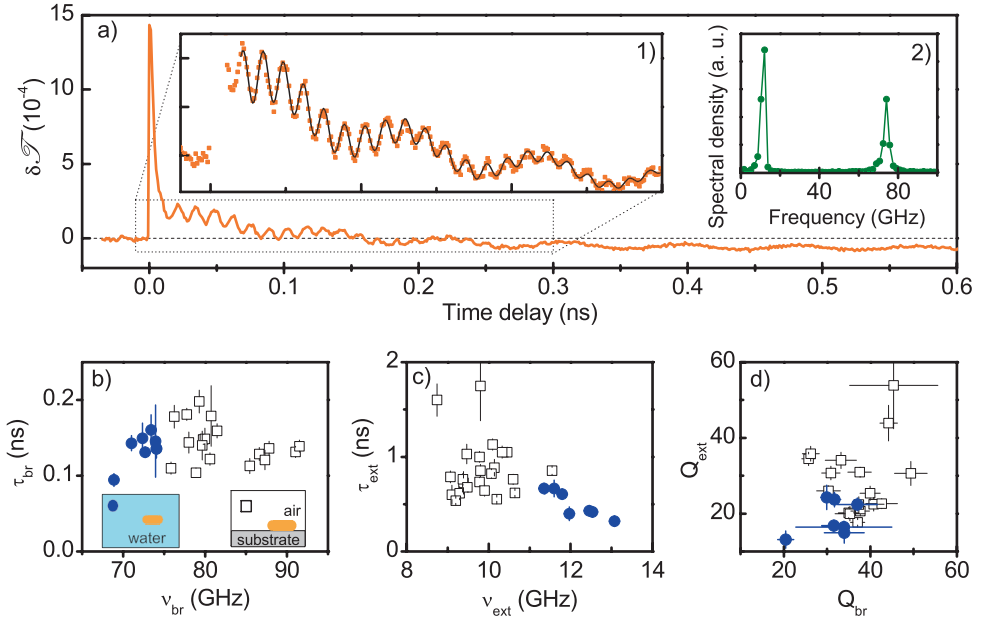


Figure 6.3: Acoustic vibrations of single gold nanorods. (a) Vibration trace of a single 25 nm \times 60 nm gold nanorod, optically trapped in water. The probe wavelength, 610 nm, lies in the blue wing of the plasmon resonance. Inset (1): zoom of a part of the trace, fitted with a sum of two damped oscillations and slow cooling. The fit gives the frequencies ν_{br} , ν_{ext} and damping times τ_{br} , τ_{ext} of the breathing and extensional modes. Lock-in integration time 30 ms per point. Inset (2): Power spectral density of the oscillatory part of the vibrational trace. (b-d) Parameters of the vibrations of single gold nanorods, optically trapped in water (blue solid circles, sample of 25 nm \times 60 nm nanorods) and immobilized on a solid substrate in air (black open squares, sample of 30 nm \times 90 nm rods). (b),(c) Scatter plots of the damping time τ_{br} , τ_{ext} versus vibration frequency ν_{br} , ν_{ext} , for the breathing and extensional modes. (d) Scatter plot of the quality factor $Q = 2\pi\nu\tau/2$ of the breathing mode (Q_{br}) versus that of the extensional mode Q_{ext} . Error bars are the fit inaccuracies.

an average quality factor of $\langle Q \rangle = 19 \pm 1.7$, lower than that of the breathing mode. As the extensional mode involves a large shear displacement, it may be more sensitive to viscous damping by the water. A quantitative analysis of the damping of the extensional mode requires extensive numerical modeling and is beyond the scope of this paper. As was observed for the spheres, the quality factors of the nanorods are broadly distributed.

To determine the contribution of the capping layer of the nanorods to the

damping, we have attempted a measurement of the damping rates of gold nanorods stabilized by CTAB. CTAB is expected to form a bilayer of ~ 4 nm thickness on the surface on the gold nanorod.¹³³ We found that trapping was less stable in this configuration. Thus far, we measured 2 nanorods in CTAB, and found damping rates similar to those of the mPEG-coated nanorods.

Discussion

Our measurements of acoustic damping of gold nanoparticles in water indicate that dissipation into the surrounding liquid and intrinsic dissipation in the nanoparticle are of similar magnitude. This result is surprising, as in most of the previous literature the damping of nanoparticle vibrations was assumed to arise mainly from radiation of sound waves into the surrounding medium. Recently, Pelton et al. have provided experimental evidence that intrinsic damping mechanisms cannot be neglected for ensembles of gold bipyramids.¹⁶³ Their measurement of the homogeneous damping time of the extensional vibration mode in various liquids was consistent with an intrinsic quality factor $\langle Q_{\text{intrinsic}} \rangle = 25 \pm 3$, in the same range as our results on the breathing mode of gold nanospheres ($\langle Q_{\text{intrinsic}} \rangle = 37 \pm 4$) and gold nanorods ($\langle Q_{\text{intrinsic}} \rangle = 84 \pm 10$).

Our measurements on single particles reveal a significant variation in the damping rates from particle to particle, indicating that a significant fraction of the intrinsic damping is caused by dissipation mechanisms that are sensitive to particle-to-particle variations in shape, crystal structure or defects. In the following we discuss several possible contributions.

Crystal defects contribute to dissipation, and variations in structural defects may contribute to a particle-to-particle variation of damping rates. Indeed, as gold nanorods have less defects than spheres, we expect and observe higher quality factors for nanorods than for spheres. It is known that as-synthesized rods are single crystals, without stacking faults, twins or dislocations,¹⁸⁹ but we cannot exclude the presence of internal defects on the basis of our experimental results. Although rods have fewer defects than spheres, variations in number of defects could still lead to the observed particle-to-particle variation of damping rates. In addition, a crystal defect common to all nanoparticles is their surface itself. Surface atoms are more mobile than bulk atoms,¹⁸⁵ providing additional channels for dissipation. Due to the large surface-to-volume ratio of the particle, the dynamics at the surface may provide a significant contribution to the total damping. Finally, for nanorods the damping rate could be influenced by the silver atoms used during rod syn-

thesis. Gold nanorods grown by the silver-assisted seed-mediated route¹¹⁹ contain 2-3% silver (by number of atoms),¹⁹² possibly opening additional dissipation channels.

The organic molecules capping nanoparticles may also contribute to the damping, and capping layer structure variations may also lead to particle-to-particle variations of the damping rate. For the extensional vibration mode of gold bi-pyramids,¹⁶³ Pelton et al. found that the capping layer of the particles may be responsible for up to 30% of the intrinsic damping. We therefore do not expect the thin organic capping layer to contribute more than 30% to the damping of the 80 nm gold spheres. For the 25 nm diameter gold nanorods the capping layer could contribute more to the damping, because of the larger surface-to-volume ratio and higher vibration frequency. However, preliminary experiments showed no big difference in damping rates between CTAB and PEG capping layers.

Our experiment opens the possibility to study the mechanisms of mechanical dissipation in metals, at frequencies in the range of 1 GHz - 1 THz. Whereas damping mechanisms in macroscopic structures have been well studied,¹⁹³ much less is known about dissipation mechanisms at these high vibration frequencies. Quality factors in the range 10^3 up to 10^5 were found for poly-crystalline gold nanoresonators with vibration frequencies in the 10 MHz-100 MHz range.^{194,195} At temperatures from 1 mK to ~ 100 K, a dominant part of damping was attributed to dislocations. The vibration frequencies in nanoparticles are much higher however, and different mechanisms may be dominant. Studies on macroscopic samples indicate that metals have higher intrinsic losses than dielectrics, due to their conduction electrons.¹⁹⁶ At room temperature and for frequencies of several GHz and above, intrinsic losses are high for both metals and dielectrics, as known from microwave ultrasonics.¹⁹⁶ In fact, losses are typically so high that they are difficult to measure accurately in macroscopic samples, and not much experimental work has been done in this regime.^{196,197} Measurements on damping of acoustic vibrations in nanoparticles provides a novel access to explore this area. This range is particularly interesting as both electron and phonon relaxation times are comparable to the period of the sound wave, and mean free paths are comparable to the particle size.¹⁹⁶ As in experiments on macroscopic samples, it may be possible to probe internal friction in metal nanoparticles, as a function of frequency, temperature, crystal structure and crystal orientation. Of particular value would be the correlation of vibrational measurements on a single nanoparticle to its exact morphology obtained by high-resolution transmission electron microscopy.

6.4 Higher order vibrational modes of gold nanospheres

In our experiment, the vibrational response of the trapped gold nanospheres is dominated by the breathing mode. However, weak signatures of other vibration modes are detected on some particles. The vibration modes of an elastic sphere have been first calculated by Lamb more than a century ago.⁵² The vibration modes in Lamb's theory are labeled by two integers, n , the harmonic order, i.e. the number of radial nodes, and l , the angular momentum number, representing the angular dependence of the mode.

Fig. 6.4(a) shows a vibrational spectrum of a trapped sphere that displayed several vibration frequencies. Besides the fundamental breathing mode $(n, l) = (0, 0)$ at $\Omega_{0,0} = 38.8$ GHz, vibration modes are detected at 84 GHz and 126 GHz. These frequencies are close to the values calculated in Lamb's theory for the first higher order radial modes of a 80 nm gold sphere¹⁸⁰ with a free boundary condition, taking the bulk elastic constants of gold. For the first higher order radial modes $(1, 0)$ and $(2, 0)$ the calculated frequencies are $\Omega_{1,0} = 2.1 \Omega_{0,0}$ and $\Omega_{2,0} = 3.18 \Omega_{0,0}$. The $(1, 0)$ radial mode was detected for 3 out of the 10 investigated single gold spheres. The excitation and detection of this mode appears robust: if the mode was found for a particular sphere, it was observed in each of several (2-5) consecutive vibrational spectra acquired on that particle in the optical trap, over a time span of up to 30 minutes. The second order radial mode $(2, 0)$ was clearly observed for 2 out the 3 the particles that displayed the $(1, 0)$ mode, but in both cases appeared in only one trace out of a series of vibrational traces acquired on the particle.

Some particles (3 out of 10) displayed a weak vibration mode with a frequency around 0.3 times the breathing mode frequency. A vibrational spectrum of a such a particle is shown in Fig. 6.4(b). The mode at 12.5 GHz is possibly the non-spherically symmetric $(n, l) = (0, 2)$ mode, corresponding to a uniaxial cigar-to-pancake deformation of the spheres. The excitation of this mode is not expected for spheres, embedded in an isotropic environment and subject to a spherically symmetric excitation mechanism. However, the ellipsoidal vibration mode can be excited in slightly elongated particles,¹⁷⁰ where the spherical symmetry is broken.

6.5 Vibration modes of gold nanorods

Figure 6.5 displays the scaling of the breathing mode frequency ν_{br} to the extensional mode frequency ν_{ext} measured on single gold nanorods in an opti-

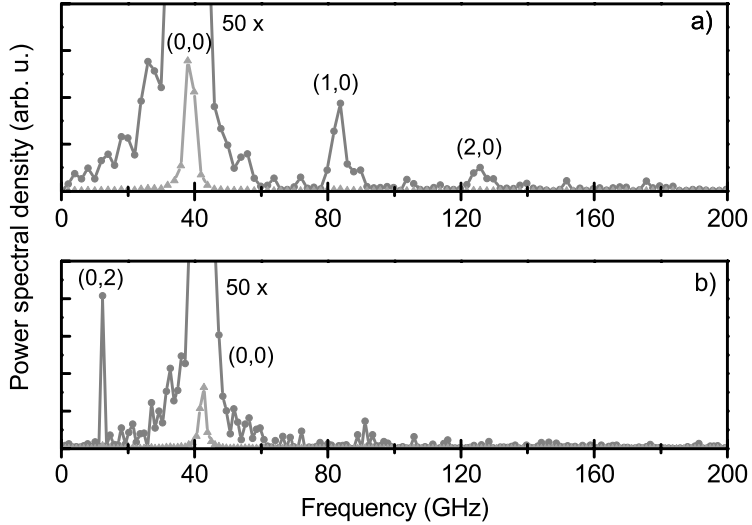


Figure 6.4: Vibration modes of single 80 nm gold spheres optically trapped in water. Vibrational spectra are dominated by the fundamental breathing mode $\Omega_{0,0}$ around 40 GHz, but weak traces of other vibrational modes are detected. (a) Vibrational spectrum of a sphere with a breathing mode at $\Omega_{0,0} = 38.8$ GHz. Weak traces of the higher order radial modes $(n, l) = (1, 0)$ at $\Omega_{1,0}$ (84 GHz, $2.16 \times \Omega_{0,0}$) and $(n, l) = (2, 0)$ at $\Omega_{2,0}$ (126 GHz, $3.25 \times \Omega_{0,0}$) are detected. (b) Vibrational spectrum of a sphere with a breathing mode at $\Omega_{2,0} = 42.4$ GHz. An additional vibration mode at 12.5 GHz ($0.29 \times \Omega_{0,0}$) is attributed to the (0, 2) ellipsoidal deformation mode.

cal trap in water. Data on the same nanorods is reported in Fig. 6.3 in Section 6.3. In addition to the data on the 7 PEG-coated rods in Section 6.3, data on 2 nanorods stabilized in CTAB are included.

It is expected that the frequency ratio $\nu_{\text{br}}/\nu_{\text{ext}}$ is proportional to the aspect ratio of the rod.¹⁹¹ In our experiment we can estimate the aspect ratio for each individual nanorod in the trap from the longitudinal plasmon resonance λ_L , obtained from the rods scattering spectrum. Here, we approximate $\text{AR} = (\lambda_L - 410)/85$, with λ_L in units of nm, by calculation of the plasmon resonance of a gold ellipsoidal particle in water, in the dipole limit. The data points in Figure 6.5 all fall on a horizontal line, indicating that the frequency ratio $\nu_{\text{br}}/\nu_{\text{ext}}$ is strongly correlated to the rods aspect ratio. The graph also displays the theoretical values calculated for a polycrystalline rod¹⁹¹ (dashed line, $\nu_{\text{br}}/\nu_{\text{ext}} = 2.32 \times \text{AR}$) and for a single crystalline rod¹⁶⁶ with its long axis along the [100] direction (dotted line, $\nu_{\text{br}}/\nu_{\text{ext}} = 3.24 \times \text{AR}$). It appears that the data are closer to the value expected for polycrystalline rods than for sin-

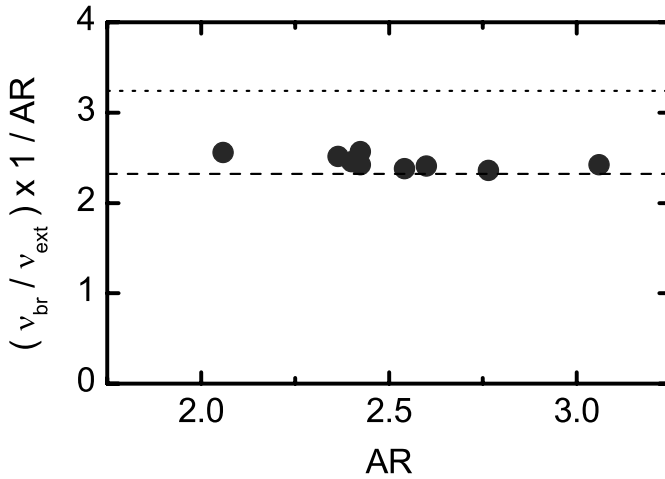


Figure 6.5: Ratio of breathing mode and extensional mode frequencies of optically trapped nanorods, as function of aspect ratio. The aspect ratio was deduced from the measured wavelength of the longitudinal plasmon resonance λ_R via $AR = (\lambda_R - 410)/85$, with λ_R in nm. Dashed line: theoretical value for a gold nanorod with polycrystalline elastic constants.^{166,191} Dotted line: theoretical value for a single crystalline rod, with the long axis of the rod in the the [100] direction.

gle crystal rods. However, this attribution depends critically on the absolute value of the aspect ratio. It is difficult to obtain an accurate absolute relation between the aspect ratio of the rod and its longitudinal plasmon resonance. Calculated values of the resonance depend sensitively on the exact shape of the tip of the rod, and on the exact thickness and structure of the capping layer, parameters that are not known with high precision for the individual rods in our experiment. Therefore, we do yet draw quantitative conclusions from the absolute value of the proportionality constant found in Fig. 6.5. The assumption of a linear relation between aspect ratio and plasmon resonance is more robust, so that our data nevertheless provides evidence for a strong correlation between aspect ratio and vibration frequency.

To come to a quantitative conclusion about the scaling of vibration mode frequencies in gold nanorods, it would be necessary to determine the exact aspect ratio of each individual nanorod in the trap by electron microscopy on the nanorod, as was done previously for nanorods immobilized on a substrate.¹⁶⁶

6.6 Conclusions

We have measured for the first time acoustic vibrations of single gold nanoparticles in an optical trap in water. Our approach directly provides the homogeneous damping time of the vibrations of the nanoparticle, in an isotropic liquid environment. We find that vibrations of the nanoparticles are damped not only by dissipation into the environment, but that damping mechanisms intrinsic to the particle must be taken into account. This intrinsic damping leads to ensemble-averaged quality factors in the range $\langle Q_{\text{intrinsic}} \rangle = 40 \pm 4$ (for 80 nm nanospheres) to $\langle Q_{\text{intrinsic}} \rangle = 84 \pm 10$ (for 25 nm \times 60 nm nanorods). Intrinsic quality factors vary largely for individual particles (standard deviations $\sim 30\%$ and $\sim 40\%$ for spheres and rods, respectively). This particle-to-particle variation provides a signature of mechanisms of intrinsic damping that are sensitive to nanometer scale variations in particle structure. Our results are the first step in the investigation of mechanisms of mechanical dissipation in metals in the frequency range 1-1000 GHz, a range that has been difficult to access so far.

Conclusions and perspectives

In this thesis we have investigated the optical trapping of single gold nanoparticles, as a novel approach to study single metal nanoparticles in solution, and to explore the use of a single metal nanoparticle as an ultra-small tool to enable mechanical manipulations on the nanometer scale. Here we conclude by summarizing the main arguments, reviewing the main results and providing a perspective on future work that may be enabled by the methods presented in this thesis.

7.1 Thesis conclusion

7.1.1 Study of single nanoparticles in solution

We have argued that the study of single gold nanoparticles in solution has potential as an approach to resolve nanoscale phenomena. The benefit of single-particle studies originates from the observation that no two nanoparticles are ever exactly alike; a given sample always presents a distribution of particle sizes and shapes. As the properties of the particles, and the processes taking place on those particles, are functions of the particle size and shape, a distribution of particle properties results. Single-particle studies give access to the full distribution of particle properties, and the correlation of multiple properties on the same particle. Time-dependent phenomena can be studied without the need for ensemble-wide synchronization, and study of

stochastic processes becomes possible. The interest in the study of particles in solution results from the observation that a variety of physical processes intrinsically takes place in solution, and that immobilization on a solid surface – the commonly taken approach to study single nanoparticles – may introduce unwanted perturbations. A study of particles in a homogeneous liquid environment prevents unknown, local nanometer-scale interactions with a solid surface, facilitating direct comparison with theoretical models.

In this thesis we have used an optical trap as a means to confine a single nanoparticle in solution to the focal spot of a microscope objective. We have demonstrated that with this approach a single nanoparticle in solution could be studied with a variety of optical techniques for practically unlimited times. Observation times up to several hours were demonstrated, but this was limited by the patience of the author rather than by any principle limitation.

As a first demonstration of an experiment that benefits from this geometry, we have studied the mechanical vibrations of gold nanoparticles with time-resolved optical techniques. For the first time we could directly measure the homogeneous damping time of the acoustic vibration of a single gold nanoparticle in a homogeneous liquid environment. Surprisingly, these damping times were a factor of 2-3 shorter than predicted by the commonly used theory – well tested in macroscopic systems – that considers acoustic energy loss by radiation of sound waves into the environment. Also, the observed vibrational damping time varied largely for individual particles, by more than a factor of two. We concluded that damping mechanisms other than radiation losses contribute significantly to the damping of the vibrations of nanoparticles. Although part of the dissipation may originate from the organic capping layer surrounding the particles, the current hypothesis is that a significant fraction of the total damping of the vibration is contributed by internal friction in the metal nanoparticle itself. Particle-to-particle variations in crystal structure and the number of crystal defects may cause the particle-to-particle variation in damping times.

7.1.2 Optically trapped single gold nanoparticles as a mechanical tool

We have argued that optically trapped single gold nanoparticles have potential to be used as tools to perform local nanoscale mechanical manipulations in solution and in complex soft-matter environments that are inaccessible to other mechanical tools.

Due to their conduction electrons, metals have higher polarizabilities than dielectric materials. In a metal nanoparticle, this polarizability is enhanced further due to the surface plasmon resonance. Even more importantly, the effect of the plasmon resonance is to concentrate the absorption profile in a narrow region around the resonance, so that the absorption at infrared wavelengths becomes small –in stark contrast to bulk metals– and appreciable optical forces can be exerted without excessive heating and the resulting detrimental radiation pressure. In practice, polarizabilities of nanoparticles at infrared wavelengths can be 20-50 times larger than those of typically used dielectric materials as glass or polystyrene. Gold nanoparticles can be trapped down to 10 nm in size, whereas trapping of dielectric particles smaller than several hundred nanometers becomes difficult. The reduced size of the nanoparticles may be beneficial for applications where the allowable space for a probe/actuator is limited, or for heterogeneous systems where the probe size limits the spatial resolution.

In this thesis we have explored the potential of single metal nanoparticles as mechanical actuators by demonstrating the novel optical trapping features that are enabled by the optical properties of single gold nanorods. Firstly, the gold nanorod can be trapped with larger forces –or down to smaller sizes – due to the high polarizability associated with the narrow longitudinal surface plasmon resonance. Secondly, the polarizability of the rods is also highly anisotropic, dominated by the dipolar dependence of the longitudinal plasmon resonance. This leads to an optical torque that aligns the rod along the polarization of the trap. We demonstrated that an optical torque of up to 100 pN·nm could be exerted on a nanorod of 25 nm diameter and 60 nm length, with a trapping power of 80 mW. This torque would be large enough to allow mechanical manipulation of relevant single (bio-)molecules such as DNA. Simultaneously, optical forces up to a few tenths of pN can be exerted on the trapped rod. The simultaneous application of these relatively large forces and torques on an ultra-small particle could enable optical manipulation in living cells.

The measurements of the optical forces and torques on the single gold nanorod were obtained from a study of the Brownian motion of the particle in the trap. Several novel methods were developed in this thesis to allow the simultaneous observation of the translational and rotational Brownian motion of the trapped rods, making use of the rod's anisotropic light scattering properties. By measuring the orientational and translational trap stiffnesses as functions of trap power, we could determine the temperature of the particle in the trap. We found heating rates around 0.5-1 K/mW, resulting in

7 *Conclusions and perspectives*

particle temperature increases around 40-80 K at the used trap powers. For biological applications these temperature increases are of concern. However, we anticipate that heating rates may be further reduced, and methods can be developed to circumvent detrimental effects resulting from this heating (see Perspectives).

The study of the temperature-dependent dynamics of the translational and rotational Brownian motion also resulted in a surprising finding about the Brownian motion of a hot particle. Firstly, our results experimentally confirmed a recently developed theory for the translational diffusion of a hot particle, moving in an inhomogeneous viscosity and temperature profile. The translational fluctuations can be described by an effective temperature, close to the average of the particle temperature and the temperature of the environment. Secondly, we found that the rotational Brownian motion must be described by a higher effective temperature. Although we suggested several possible explanations in Chapter 4, this effect was not fully understood. After publication of our work, theoretical physicists from Leipzig immediately started to think about this surprising result. Very recently an analytical theory has been developed,^{92,198} showing that our results are quite generally valid for Brownian motion of hot particles, both for spheres and rods. The reason that the rotational Brownian motion must be described by a different temperature than the translational Brownian motion is that the velocity profile around the particle moving through a liquid is different for the two types of motion. The velocity profile for rotational motion follows a steeper spatial decay (scaling as $1/R^3$) than the profile for translational motion (scaling as $1/R$). As a result, the rotational motion is most sensitive to properties close to the particle, where temperatures are highest and viscosities are lower.

7.1.3 Overview of results obtained in this thesis

Here we list as concise statements what we believe to be the most important scientific findings obtained in this thesis, with reference to the Chapters in which they were reported.

1. The signal-to-noise ratio in photothermal detection of absorbing nano-objects can be enhanced by i) choice of a liquid surrounding the particle with optimal photothermal properties (high $\partial n/\partial T$, high n and low heat capacity/thermal conductivity); ii) using a detection laser with a wavelength outside of the absorption band of the absorber and the highest possible intensity; iii) by thermal isolation of the absorber from the glass substrate.

Chapter 2

2. A trapped single gold nanorod of 25 nm diameter and 60 nm length can serve as a simultaneous transducer of forces ($\sim 0.1 - 1$ pN) and torques ($\sim 10 - 100$ pN·nm), large enough to enable mechanical manipulation of relevant single (bio-)molecules.

Chapter 4

3. The translational and rotational Brownian motions of a hot nanoparticle are described by different effective temperatures. The temperature of rotational Brownian motion is closest to the particle temperature.

Chapter 4

4. The damping of acoustic vibrations of gold nanoparticles is determined both by radiation of sound waves to the environment and by intrinsic dissipation in the nanoparticle.

Chapter 6

7.2 Perspectives

The results in this thesis demonstrate the potential of studying single particles in solution with the aid of an optical trap, and the promise of optical trapping for the use of gold nanoparticles as mechanical tools. Here we discuss directions that could be taken, in the immediate and near future.

7.2.1 Deposition of trapped particles on a solid substrate

For a variety of experiments it would be valuable to study a single nanoparticle in the optical trap in solution, subsequently deposit the particle on a solid substrate and repeat the performed measurements. Such experiments would enable the direct probing of the optical, thermal and mechanical effects of the substrate. Additionally, once the particle is immobilized, the coverslip can be taken to an electron microscope to determine the exact morphology of the particle that was studied.^{166,170} The deposition of optically trapped particles on substrates has been demonstrated by several authors.^{199,200} Aided by the specially designed flow-cell (Appendix B), this type of experiments can be performed immediately.

7.2.2 Focal engineering

The quality of optical trapping is determined by the gradient of the light intensity that can be created. As in so many applications in microscopy, this ultimately boils down to the requirement to create the smallest possible focal spot. This requirement is especially challenging in optical trapping applications; the near-infrared wavelengths that are typically used fall outside of the wavelength range for which commercially available microscope objectives are optimized, and frequently spherical aberrations are introduced when trapping is performed many microns away from a glass surface. In this thesis we have already seen the importance of these spherical aberrations for optical trapping, and the need to compensate them with inventive methods.

In recent years there have been much developments in the engineering of beam foci by altering the phase and amplitude profiles of an incoming beam with spatial light modulators.^{201,202} With these methods, optical trapping of dielectric particles through a turbid layer has been demonstrated.²⁰³ We anticipate that these methods can help to overcome the limitations of commercial microscope objectives at near infrared wavelengths and improve the optical trapping of metal nanoparticles.

A different approach comes from the realization that the properties of a focus depend on the polarization structure of the beam.²⁰⁴ Besides the familiar linearly or circularly polarized Gaussian beams, Maxwell's equations allow solutions with many other polarization structures, that can have surprising properties. In particular, the focus of a radially polarized beam can be both tighter than the focus of the linearly polarized beam,¹¹⁶ and be almost completely longitudinally polarized.²⁰⁵ A property accompanying the latter effect is that the longitudinal component of the Poynting vector vanishes at the focus.²⁰⁶ For optical trapping of metal nanoparticles, this has the important consequence of eliminating radiation pressure, that normally results from absorption of the trap laser. This leads to a deeper potential for a given trap power or, conversely, a reduced heating of the trapped particle for a given trap depth. For typical conditions as reported in this thesis, the temperature increase of the particle may be reduced by about a factor of two for the same achieved trap depth.

7.2.3 Single-particle studies in solution

With practically unlimited observation times on single metal nanoparticles in solution, a variety of exciting applications comes within reach. Here we think of problems in nanoscale heat conduction,²⁰⁷⁻²¹⁰ and the formation of a vapor-shell around a hot nanoparticle.^{211,212} The formation of a vapor-shell around a nanoparticle is an interesting thermodynamic problem in itself, but may also enable practical applications. For example, these nanobubbles have already been used to enhance the effectiveness of cancer therapies.²¹³ Reports thus far have focused on the case where bubbles are formed transiently, by heating of the metal nanoparticles with short optical pulses. If conditions for stable vapor-shell formation can be found, the trapped gold nanoparticle can be effectively studied in gas-phase. Another exciting direction is the study of nanoparticle catalysis. Since the pioneering work of Haruta²¹⁴ in 1989 it is known that gold nanoparticles can be efficient catalysts.²¹⁵ Catalysis is performed both in the gas-phase with supported nanoparticles and with nanoparticles in solution.²¹⁶ Study on single particles in solution may provide new insights into the heterogeneous nature of catalysis.

7.2.4 Manipulation of bio-molecules

One of the methods that has revolutionized biophysics in the last decades has been the application of optically trapped particles to mechanically manipu-

late single bio-molecules *in-vitro*. Thus far, these studies have been performed exclusively using dielectric particles. Concern about laser-induced heating of metal nanoparticles has most likely been the reason that metal nanoparticles have not been used for single-molecule manipulation.

We advocate here that such trials should be made nevertheless, to characterize to what degree the attached bio-molecules are affected. Additionally, we suggest that continued efforts should be made to i) reduce the laser-induced heating and ii) find inventive ways to circumvent any detrimental effects of heating on the biological system of interest. Specific possibilities of the first include the optimization of optical trapping by focal engineering as addressed above. As a possible method to contribute to the latter we suggest to make use of the steep decay ($1/R$) of the temperature around the particle, for example by using particles with a silica coating. Such a coating does not affect significantly the heating of the particle or the resulting temperature, but simply serves as a heat resistant layer that keeps the bio-molecules at a safe distance.

7.2.5 Trapping in living cells

In this thesis we have advocated the use of optically trapped metal nanoparticles in crowded environments. The prime example of such an environment is a living cell. Our vision, perhaps rather naive, is to study the mechanical properties of cellular components and/or single molecules in their natural environment. Of course, the challenges are great. However, we advocate that such experiments simply be tried, and their limits explored. One of the challenges to overcome is the effect of trapping beam aberrations that result from the refractive index variations in the cell. We believe that significant progress can be made here using adaptive optics. An additional complication is that cellular components may move, so that the trapping beam will have to be adapted dynamically. Whether, or to what degree, the laser-induced heating of the metal nanoparticles will affect cellular experiments remains to be characterized. Even if heating turns out to be too great an obstacle to enable non-destructive single molecule manipulations in the cell, we anticipate that trapped metal nanoparticles can be used otherwise, for example to perform some form of nanoscale surgery.

Appendices

A

Thermal and optical constants for selected materials

Table A.1: Thermal and optical constants for selected materials at room temperature and normal pressure ^a

Substance	n^b	$10^4 \times \frac{\partial n}{\partial T}$ K ⁻¹	$10^{-6} \times C_p$ J m ⁻³ K ⁻¹	κ W m ⁻¹ K ⁻¹	$10^{10} \times \Sigma_{PT}$ m ³ J ⁻¹	$10^3 \times FOM$ m W ⁻¹
BK7 glass	1.52	-0.13	2.2	1.1	0.09	0.02
PMMA	1.49	-1.2	1.4	0.2	1.3	0.90
Water	1.33	-0.9	4.2	0.56	0.29	0.21
Glycerol	1.47	-2.7	2.6	0.28	1.5	1.4
Ethanol	1.36	-4.4	1.9	0.17	3.1	3.5
Hexane	1.37	-5.5	1.5	0.12	5.0	6.1
Pentane	1.36	-6.0	1.5	0.14	5.6	6.0
Chloroform	1.45	-6.2	1.4	0.13	6.3	7.0
Carbon tetrachloride	1.47	-6.1	1.3	0.10	7.1	8.6
Carbon disulfide	1.63	-8.1	1.3	0.16	11	8.2

^a The tabulated values for each substance are the refractive index n and its derivative with respect to temperature $\frac{\partial n}{\partial T}$, the heat capacity at constant pressure C_p , the thermal conductivity K , the photothermal strength $\Sigma_{PT} = n \left| \frac{\partial n}{\partial T} \right| \frac{1}{C_p}$, and the photothermal figure-of-merit $FOM = n \left| \frac{\partial n}{\partial T} \right| \frac{1}{K}$. Values are from the CRC Handbook of Chemistry and Physics (49th ed.) and Bialkowski.⁹⁴

^b For sodium light ($\lambda = 589.3$ nm), CRC Handbook of Chemistry and Physics

B

Optical microscope

B Optical microscope

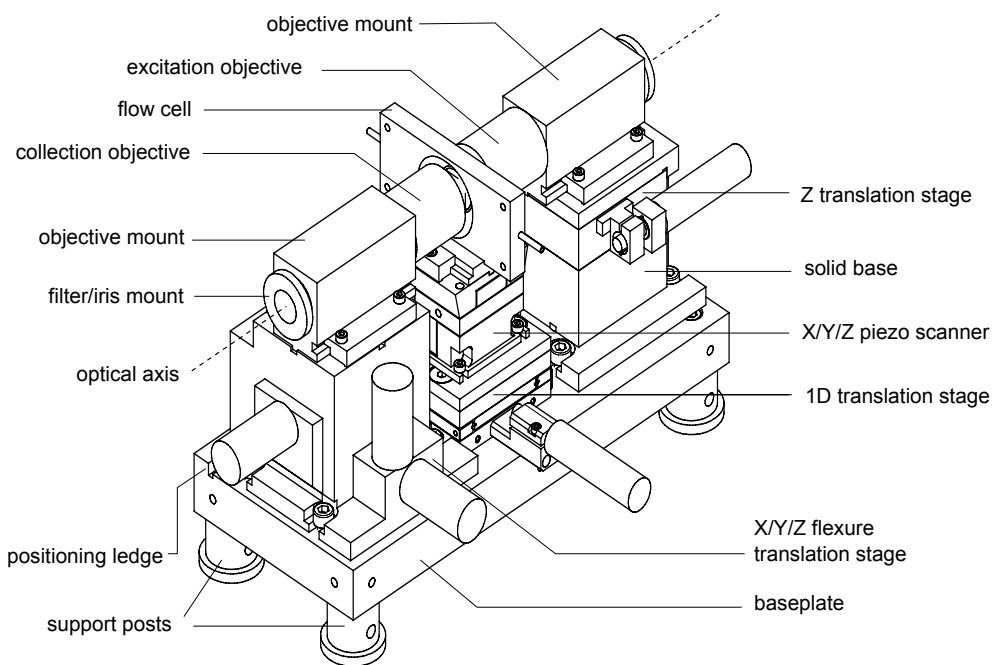


Figure B.1: Optical microscope assembly constructed in this thesis, in a configuration as used in part of the reported experiments. Three independent constructions are mounted on a 25 mm thick aluminium baseplate, to support the excitation-objective, the sample holder/flow-cell and the collection-objective. The constructions can be removed and repositioned accurately with the help of positioning ledges. The design aims to achieve high mechanical stability and low thermal drift by a compact, stiff construction and a minimum number of translation elements. The optimization is directed to achieve the highest stability for the relative position between the excitation objective and the sample holder (flow-cell).

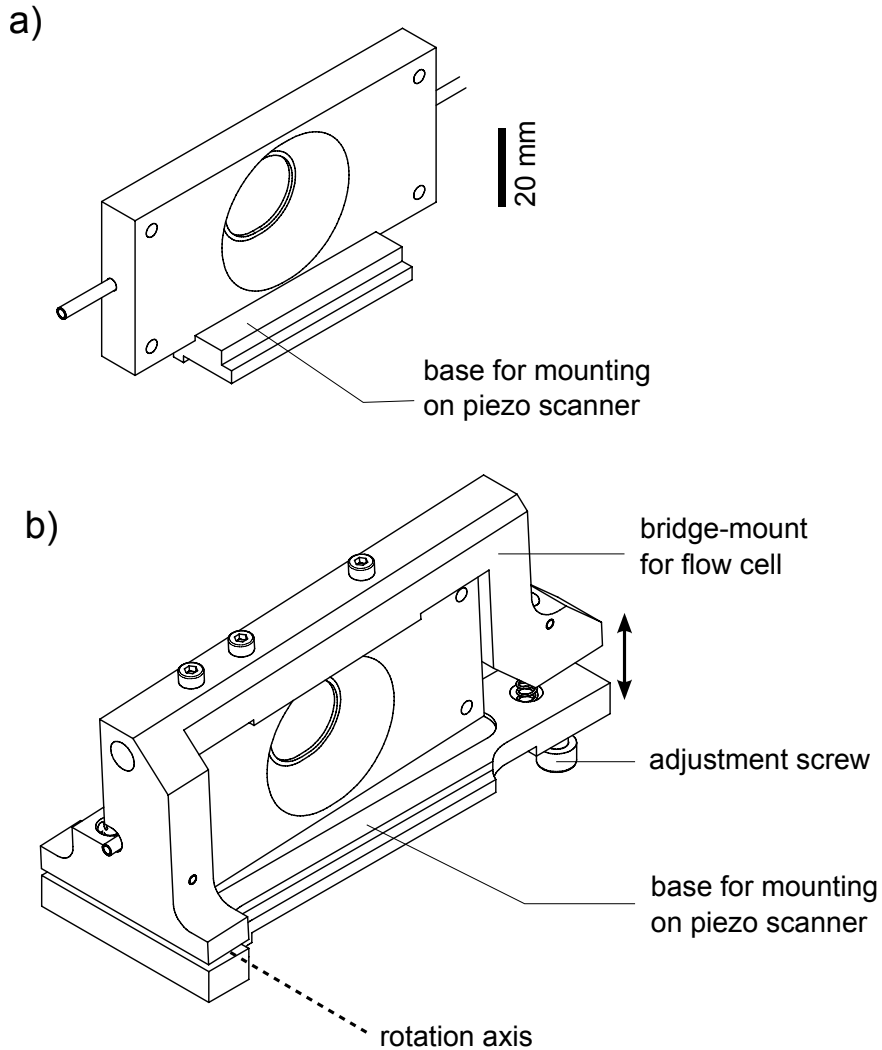


Figure B.2: Two configurations to mount the flow-cell on the piezo-scanner in the microscope. a) Fixed mount. b) Mount that allows manual translation in the vertical direction, while maintaining mechanical stability. The flow-cell is mounted hanging on a spring-loaded bridge construction, that can be rotated around an axis (two ball joints) on one end with an adjustment screw on the other end. At the center of the flow cell, the rotation amounts to an effective vertical translation, over a range up to ± 1 mm. This movement facilitates the search for a specific location on the sample over a region larger than the $100 \mu\text{m}$ range of the piezo-scanner. The experiments reported in this thesis were performed with the fixed mount.

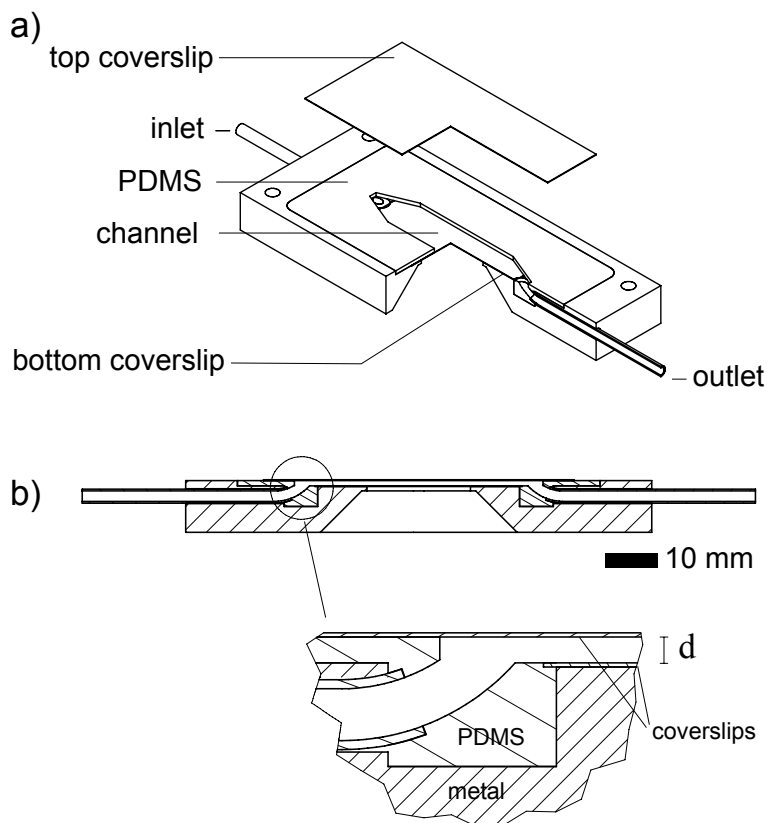


Figure B.3: Details of the flow-cell used in the experiments reported in this thesis. a) Perspective view. The construction with the flexible in/outlets and the bottom coverslip embedded in polydimethylsiloxane (PDMS) can be remade repeatedly, when desired. A micro-fluidic channel is cut out from the PDMS layer by hand. The top coverslip forms the closure of the micro-fluidic channel when pressed on the PMDS, and can be repeatedly re-applied. b) Side view. The inset shows a detailed view of the connection between the inlet of the cell and the micro-fluidic channel. The design eliminates contact of the fluid with the metal part of the flow-cell casing. Channel thickness d could be varied between $40 \mu\text{m}$ and 1mm by the use of metal casings with different chamber depths. The design was based on a design from the group of Dr. J. van Noort (Leiden University).

C

Optical constants of bulk gold

C Optical constants of bulk gold

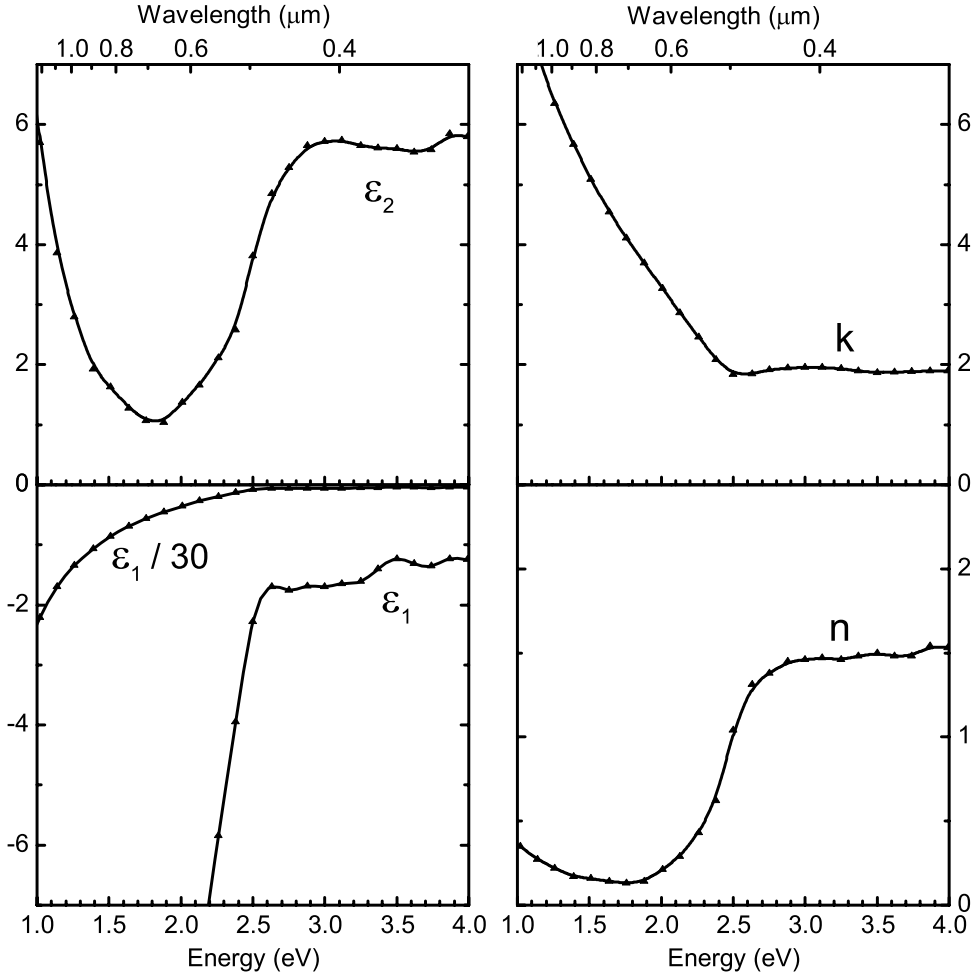


Figure C.1: The optical constants of bulk gold at room temperature as a function of photon energy, used throughout this thesis. The data are from Johnson and Christy¹¹³ and were obtained from reflection and transmission measurements on vacuum-evaporated thin films of gold. The individual panels display the real and imaginary parts of the complex dielectric function $\tilde{\epsilon} = \epsilon_1 + i\epsilon_2$ and the real and imaginary parts of the complex refractive index $\tilde{n} = n + ik$. The complex dielectric function and the complex refractive index are related as $\tilde{\epsilon} = \tilde{n}^2$, so that $\epsilon_1 = n^2 - k^2$ and $\epsilon_2 = 2nk$. The symbols represent tabulated measured values, while the solid lines are spline interpolations.

D

Hydrodynamic friction coefficients

As the friction coefficients for the gold nanorod we have used the analytical expressions derived by Francis Perrin for a prolate spheroid¹²⁷ with aspect ratio ρ . The friction coefficient ζ_r for rotation around a short principal axis is given as

$$\zeta_r = 8\eta V \frac{\rho^4 - 1}{(2\rho^2 - 1)S(\rho) - 2\rho^2} \quad (\text{D.1})$$

where η is the medium's viscosity, V is the hydrodynamic volume, and

$$S(\rho) = \frac{2\rho}{\sqrt{\rho^2 - 1}} \log \left\{ \rho + \sqrt{\rho^2 - 1} \right\}. \quad (\text{D.2})$$

For translation, the friction coefficients are given by

$$\zeta_{tr,\parallel} = 16\pi\eta \left(\frac{3\rho^2 V}{4\pi} \right)^{1/3} \frac{\rho^2 - 1}{(2\rho^2 - 1)S(\rho) - 2\rho^2} \quad (\text{D.3})$$

for translation parallel to the long axis of the spheroid, and

$$\zeta_{tr,\perp} = 32\pi\eta \left(\frac{3\rho^2 V}{4\pi} \right)^{1/3} \frac{\rho^2 - 1}{(2\rho^2 - 3)S(\rho) + 2\rho^2} \quad (\text{D.4})$$

for translation perpendicular to the long axis of the spheroid.

The friction coefficients for translation and rotation are plotted as functions of aspect ratio in Fig. D.1(a) and Fig. D.1(b) respectively, for an ellipsoid

D Hydrodynamic friction coefficients

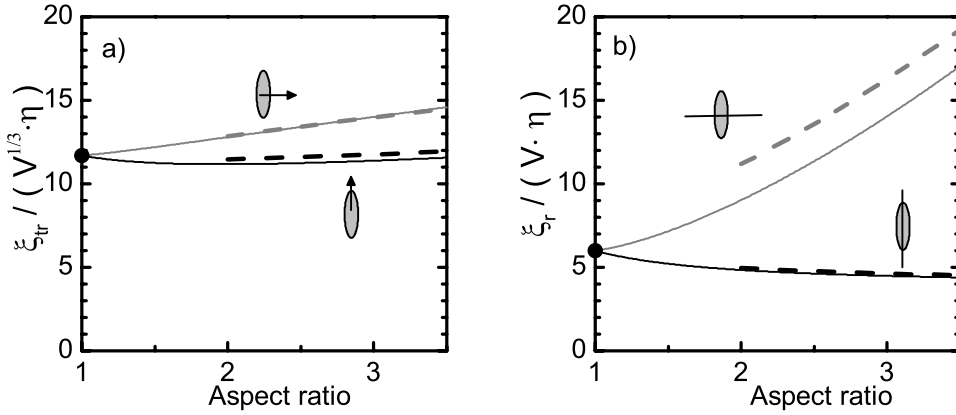


Figure D.1: Hydrodynamic friction coefficients for ellipsoids, cylinder and spheres. a) Translational friction coefficients as functions of aspect ratio for a prolate spheroid (solid lines¹²⁷) and a cylinder (dashed lines²¹⁷) of the same volume V . Black (Grey) curves: friction coefficients for translation parallel (perpendicular) to the symmetry axis of the rod. The Stokes equation $\zeta_{tr} = 6\pi\eta (3V/(4\pi))^{1/3}$ is shown as a limit for an aspect ratio of 1 (black dot). b) Rotational friction coefficients as functions of aspect ratio for a prolate spheroid (solid lines¹²⁷) and a cylinder (dashed lines^{129,217}) of the same volume V . Black (Grey) curves: friction coefficients for rotation around the long symmetry axis (one of the short symmetry axes) of the rod. The Stokes equation $\zeta_r = 6\eta V$ is shown as a limit for an aspect ratio of 1 (black dot).

of constant volume. As the real shape of our gold nanorods is not an ellipsoid, but something close to a spherically capped cylinder, the expressions for ellipsoids are expected to provide an approximate value only. For comparison, we also plot the values of the friction coefficients for cylinders, as calculated by Tirado et al.²¹⁷ Whereas the expression for the friction coefficients for spheroids are valid for particles of arbitrary aspect ratio, the expressions for cylinders are expected to provide reliable results only for aspect ratios larger than 2.

Temperature-dependent viscosity of water

As can be seen in Fig. D.2, the temperature dependence of the viscosity of water is well described by a Vogel-Fulcher law as:⁹⁰

$$\eta(T) = \eta_{\infty} \exp\left(\frac{A}{T - T_{VF}}\right), \quad (\text{D.5})$$

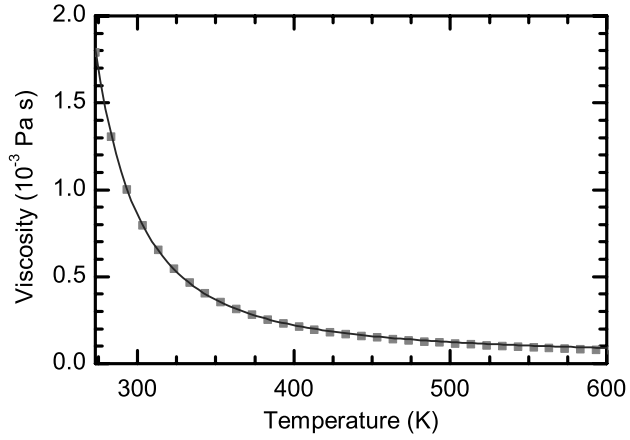


Figure D.2: Viscosity of water as function of temperature, at vapor saturation pressure. The influence of pressure on viscosity in this range is small. Squares: data derived from NIST Chemistry Webbook.²¹⁸ Solid line: Vogel-Fulcher law with parameters as used in this study.

with $\eta_{\infty} = 0.0298376 \cdot 10^{-3} \text{ Pa} \cdot \text{s}$, $A = 496.889 \text{ K}$ and $T_{\text{VF}} = 152.0 \text{ K}$.

Calculation of the orientational trap stiffness from a measured spectral intensity ratio

We calculate the rotational trap stiffness κ_r from the time averaged spectral intensity ratio $\langle I_{\parallel} \rangle_t / \langle I_{\perp} \rangle_t$. Here $\langle I_{\parallel} \rangle_t$ and $\langle I_{\perp} \rangle_t$ are the time-averaged values of the intensity of the longitudinal plasmon resonance, detected with analyzer parallel and perpendicular to the trap laser polarization, respectively. The incoming light is white light from a Xenon arc lamp, therefore it is unpolarized (randomly polarized) thermal light. We assume ergodicity and evaluate the intensity ratio as

$$\frac{\langle I_{\parallel} \rangle_t}{\langle I_{\perp} \rangle_t} = \frac{\langle \cos^2 \theta \rangle_T}{\langle \sin^2 \theta \cos^2 \phi \rangle_T} \quad (\text{E.1})$$

where θ and ϕ are polar angles of the rod axis with respect to the trap polarization, as defined in Fig. E.1 a), and the subscripted T denotes a thermally weighted averaging. The weights in the averaging are given by the Boltzmann distribution $\propto \exp \left\{ -U(\theta) / k_B \widetilde{T}_B \right\}$ where the potential is $U(\theta) = -\frac{1}{2} \kappa_r \cos^2 \theta$. We find for the numerator²¹⁹

$$\langle \cos^2(\theta) \rangle = \frac{1}{2\sqrt{\mathbb{E}} \text{Daw}(\sqrt{\mathbb{E}})} - \frac{1}{2\mathbb{E}} \quad (\text{E.2})$$

E Calculation of the orientational trap stiffness from a measured spectral intensity ratio

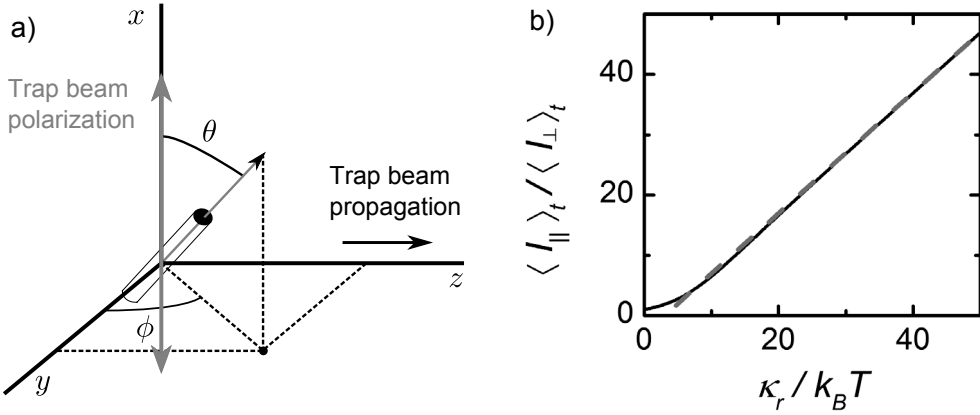


Figure E.1: a) Coordinate system. b) Calculated spectral intensity ratio $\langle I_{\parallel} \rangle_t / \langle I_{\perp} \rangle_t$ versus rotational trap stiffness κ_r . Solid line: analytical solution (eq. E.6). Dashed line: Linear approximation for high trap stiffness (eq. E.7).

where we have used the Dawson function defined as

$$\text{Daw}(z) \equiv \exp(-z^2) \int_0^z dt \exp(t^2) \quad (\text{E.3})$$

and

$$\Xi \equiv \frac{\kappa_r}{2k_B \widetilde{T}_B} \quad (\text{E.4})$$

Noting that the angles ϕ and θ are independent, and that there is no preferred value for the angle ϕ we find for the denominator

$$\langle \sin^2(\theta) \cos^2(\phi) \rangle = \frac{1}{2} (1 - \langle \cos^2(\theta) \rangle) \quad (\text{E.5})$$

and we evaluate the intensity ratio as

$$\langle I_{\parallel} \rangle_t / \langle I_{\perp} \rangle_t = \frac{2\sqrt{\Xi} - 2\text{Daw}(\sqrt{\Xi})}{2\Xi\text{Daw}(\sqrt{\Xi}) - \sqrt{\Xi} + \text{Daw}(\sqrt{\Xi})} \quad (\text{E.6})$$

The relation is plotted in Fig. E.1 b). For $\kappa_r \gg k_B \widetilde{T}_B$, the function is well approximated by the first terms in the power series expansion:

$$\langle I_{\parallel} \rangle_t / \langle I_{\perp} \rangle_t \simeq \frac{\kappa_r}{k_B \widetilde{T}_B} - 3 \quad (\text{E.7})$$

which is shown as the dotted line in Fig. E.1 b).

Correlation functions in a potential

In this appendix we discuss the calculation of the autocorrelation functions of light scattered by a trapped nanoparticle.

The goal is to evaluate the autocorrelation function of the scattered intensity I , defined as

$$G^{(2)}(\tau) = \frac{\langle I(t)I(t+\tau) \rangle_t}{\langle I(t) \rangle_t^2} \quad (\text{F.1})$$

where $I(t)$ is the scattered intensity at a time t and $I(t+\tau)$ is the scattered intensity a time τ later. The intensity is assumed to be a stationary random function of time (we take $t=0$ in the following).

We make the assumption that the rotational and translational motions of the trapped particle are independent¹, so that we can write

$$G^{(2)}(\tau) = G_{tr}^{(2)}(\tau)G_r^{(2)}(\tau) \quad (\text{F.2})$$

where $G_{tr}^{(2)}(\tau)$ and $G_r^{(2)}(\tau)$ are the translational and rotational factors of the correlation function, respectively.

¹This is not strictly true for the gold nanorod in the trap. Indeed, both the translational friction and translational trap-stiffness depend on the orientation of the rod. The rotational stiffness is proportional to the local intensity, and thus depends on the position of the rod in the trap.

Rotational autocorrelation function

We outline the calculation of the rotational part of the autocorrelation function of light scattered by the rod in the optical trap, for the case where the incoming excitation light is linearly polarized parallel to the trap laser, and the scattered light is collected behind an analyzer perpendicular to the trap laser polarization. In the particular detection geometry considered here, the scattered intensity is related to the orientation of the rod as

$$I \propto \cos^2 \theta \sin^2 \theta \cos^2 \phi \quad (\text{F.3})$$

where θ and ϕ are polar angles of the rod axis with respect to the trap polarization, as defined in Fig. E.1 a). We have assumed the scattering by the transverse plasmon resonance to be negligible, and the absence of any background intensity.

The orientational dynamics of the rod in the optical potential are governed by the Fokker-Planck equation,^{220–222} which relates the probability distribution of orientation of the rod $p(\theta, \phi, t)$ to the rotational friction coefficient ζ_r for rotation around a short principal axis, and the potential $U(\theta) = -1/2\kappa_r \cos^2 \theta$ as

$$\frac{\partial p}{\partial t} = \frac{1}{\zeta_r} [k_B T \nabla_S^2 p + \nabla_S \cdot (p \nabla_S U)] \quad (\text{F.4})$$

where ∇_S denotes the gradient operator restricted to the surface of a sphere with radius 1.

To proceed with the calculation, we assume ergodicity to replace the time average $\langle \dots \rangle_t$ in the correlation function by the thermally weighted ensemble average $\langle \dots \rangle_T$. The expressions for $I(0)$ and $I(\tau)$ can be formulated in terms of the probability $p(\theta_0, \phi_0, 0)$ to find the rod at an orientation (θ_0, ϕ_0) at time 0 (we take this to be the Boltzmann distribution) and the conditional probability $p(\theta, \phi, \tau | \theta_0, \phi_0, 0)$ to find the rod at an orientation (θ, ϕ) at time τ given that it was at an orientation (θ_0, ϕ_0) at time 0.

An analytic solution for $p(\theta, \phi, \tau | \theta_0, \phi_0, 0)$ can be found in the limit of high rotational trap stiffness. When $\kappa_r \gg k_B T$, the angular deviations of the rod from the orientation parallel to the trap laser polarization will be small: $\theta \ll 1$. The problem then becomes that of a thermally excited harmonic oscillator. The potential is $U(\theta) = \frac{1}{2}\kappa_r \theta^2 + \text{constants}$, and we consider the expression for the thermal average with terms up to third order in θ . In addition, the evaluation of integrals for the thermal averaging can be simplified by extending the integration limits from $\theta \in [0, 2\pi)$ to $\theta \in [0, \infty)$ as the probability

for the occupation of large angles is negligible. To simplify the calculation, and allowed because we have assumed to the excursions from equilibrium to be small, we change from 2D polar to 2D Cartesian coordinates $\chi = \theta \cos \phi$ and $\Psi = \theta \sin \phi$. The required solution to the Fokker-Planck equation is:²²⁰

$$p(\chi, t | \chi_0, t_0) = \sqrt{\frac{\kappa_r}{2\pi k_B T S(\tau, 0)}} \exp \left[-\frac{\kappa_r \left(\chi - \chi_0 e^{-(t-t_0)/(2\tau_r)} \right)^2}{2k_B T S(t, t_0)} \right] \quad (\text{F.5})$$

with

$$\tau_r = \frac{\zeta_r}{2\kappa_r} \quad (\text{F.6})$$

and

$$S(t, t_0) = 1 - e^{-(t-t_0)/\tau_r} \quad (\text{F.7})$$

Evaluating the expression for the correlation function with these approximations, we find

$$G_r^{(2)}(\tau) = 1 + 2 \exp(-\tau/\tau_r) \quad (\text{F.8})$$

where

$$\tau_r = \frac{\zeta_r}{2\kappa_r} \quad (\text{F.9})$$

It is interesting to compare the rotational correlation times as discussed here for a gold nanorod in an optical potential to correlation times measured on ensembles of gold nanorods, both freely diffusing^{80,133} and weakly trapped.⁸⁰ In the case of freely diffusing nanorods the correlation times are determined by the inverse of the rotational diffusion constant D_r , itself the ratio of the thermal energy $k_B T$ to the rotational friction coefficient ζ_r . Specifically, the rotational contrast observed in a configuration with vertically polarized excitation light and horizontally polarized detection decays with a time constant $\tau_{r,\text{free}} = 1/12D_r = \zeta_r/(12k_B T)$.¹³³

As the orientational trap stiffness κ_r can reach values significantly exceeding $6k_B T$ (we demonstrate an orientational trap stiffness up to $40k_B T$ in this thesis), the rotational correlation times observed on a gold nanorod in an optical trap can be significantly shorter than rotation times for freely diffusing rods. In addition, correlation times in a trap will be shorter due to the heating of the rods: the effective viscosity for the rotation of the hot rod can be significantly below the viscosity of the medium at room temperature.

Translation autocorrelation function

The calculation of the translational part of the autocorrelation function follows along the same line as the calculation of the rotational part. For the translational motion, the relevant intensity function is a Gaussian beam

$$I(x, y, z) \propto \exp \left\{ -2 \left(\frac{x^2}{w_x^2} + \frac{y^2}{w_y^2} + \frac{z^2}{w_z^2} \right) \right\} \quad (\text{F.10})$$

with widths w_x, w_y, w_z in x, y and z directions respectively.

In each dimension, the potential for a trapped particle is harmonic, for example in the x -direction given by $U = \frac{1}{2}\kappa_{tr,x}x^2$, with $\kappa_{tr,x}$ the relevant translational friction coefficient. We assume that the motions in the three dimensions are independent, so that the correlation function is simply a product over the functions in the one-dimensional case.

As for the rotational case, the translational dynamics of the trapped particle are governed by the Fokker-Planck equation (as in F.4, with now the translational friction coefficient, and the gradient operator ∇). Because the potential for translations is harmonic, as approximated for the rotational case, the solution of the Fokker-Planck equation is as in Eq. F.5, now with

$$\tau_{tr} = \frac{\tilde{\zeta}_{tr}}{2\kappa_{tr}} \quad (\text{F.11})$$

Evaluating the expression for the correlation function we find, for each dimension,

$$G_{tr}^{(2)}(\tau) = \sqrt{\frac{A+1}{A+(1-\exp(-\tau/\tau_{tr}))}} \quad (\text{F.12})$$

where

$$A = \frac{1}{4} \left(\frac{\kappa_{tr}w^2}{2k_B T} \right)^2 + \frac{\kappa_{tr}w^2}{2k_B T} \quad (\text{F.13})$$

with w the width of the Gaussian beam in the evaluated dimension and

$$\tau_{tr} = \frac{\tilde{\zeta}_{tr}}{2\kappa_{tr}} \quad (\text{F.14})$$

For a stiff trap, the translational fluctuations are much smaller than the focus size w , and we have $\kappa_{tr}w^2/(2k_B T) \gg 1$. In this case we can approximate Eq. F.12 in each dimension by a Taylor expansion in $1/A$ as

$$G_{tr}^{(2)} \approx 1 + \frac{1}{2A} \exp(-\tau/\tau_{tr}) \quad (\text{F.15})$$

G

Heat dissipation of metal spheres and ellipsoids in water

We examine the difference between the steady-state temperature profiles around a heated metal sphere and an prolate spheroid with a moderate aspect ratio (less than 5), for particles dissipating a power P_{diss} in a medium with a thermal conductivity K_m (independent of temperature). We take the approximation that the heat conductivity of the metal is infinite, therefore that the temperature in the particle is uniform. Within these approximations, the steady-state heat diffusion equation is a Poisson-type equation²²³

$$\nabla^2 T = -\frac{\dot{q}}{K_m} \quad (\text{G.1})$$

where \dot{q} is the volumetric heat release rate and K the thermal conductivity of the medium. Following the analogy with the equation for an electrostatic potential, the solution of Poisson's equation for heat conductivity in steady state for a prolate spheroidal source is²²⁴

$$\Delta T(\xi) = \frac{1}{8\pi K_m} \frac{P_{\text{diss}}}{\sqrt{a^2 - b^2}} \log \left(\frac{\sqrt{\xi + a^2} + \sqrt{a^2 - b^2}}{\sqrt{\xi + a^2} - \sqrt{a^2 - b^2}} \right) \quad (\text{G.2})$$

with a and b the major and minor semi-axis of the spheroid respectively, and ζ an ellipsoidal coordinate given by

$$\zeta = \frac{1}{2} \{ (x^2 + y^2 + z^2) - (a^2 + b^2) \} + \frac{1}{2} \sqrt{(a^2 + b^2)^2 + (x^2 + y^2 + z^2)^2 - 2x^2(b^2 - a^2) - 2(y^2 + z^2)(a^2 - b^2)}$$

(G.3)

The surface temperature of the particle is found for $\zeta = 0$.

The analytical solution for the temperature change of the ellipsoid compared to that of the sphere with the same volume is shown in Fig. G.1. For an aspect ratio of 2, the temperature change is less than 5%. This means that, to this degree of accuracy, we can replace the nanorod by a sphere with the same volume. The temperature profile around an ellipsoidal particle is presented in Fig. G.2.

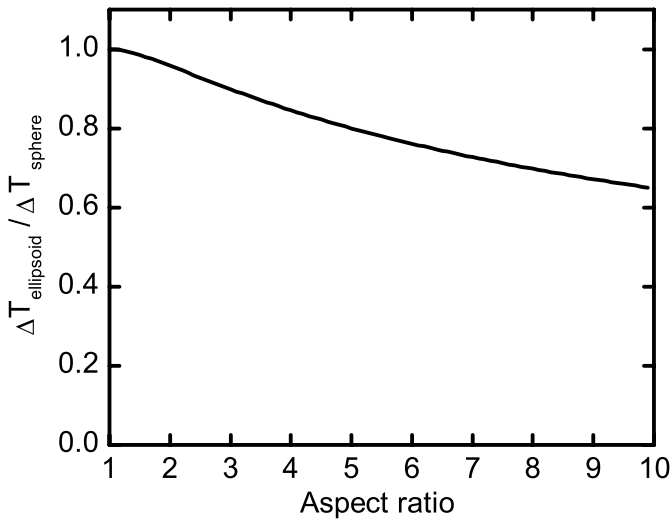


Figure G.1: Heat loss of an ellipsoid of revolution, relative to a sphere of the same volume, for a given dissipative power.

The change of thermal conductivity conductivity is less than a few percent in the whole temperature range of our experiments.²¹⁸ We therefore took the conductivity of water at room temperature in all our calculations.

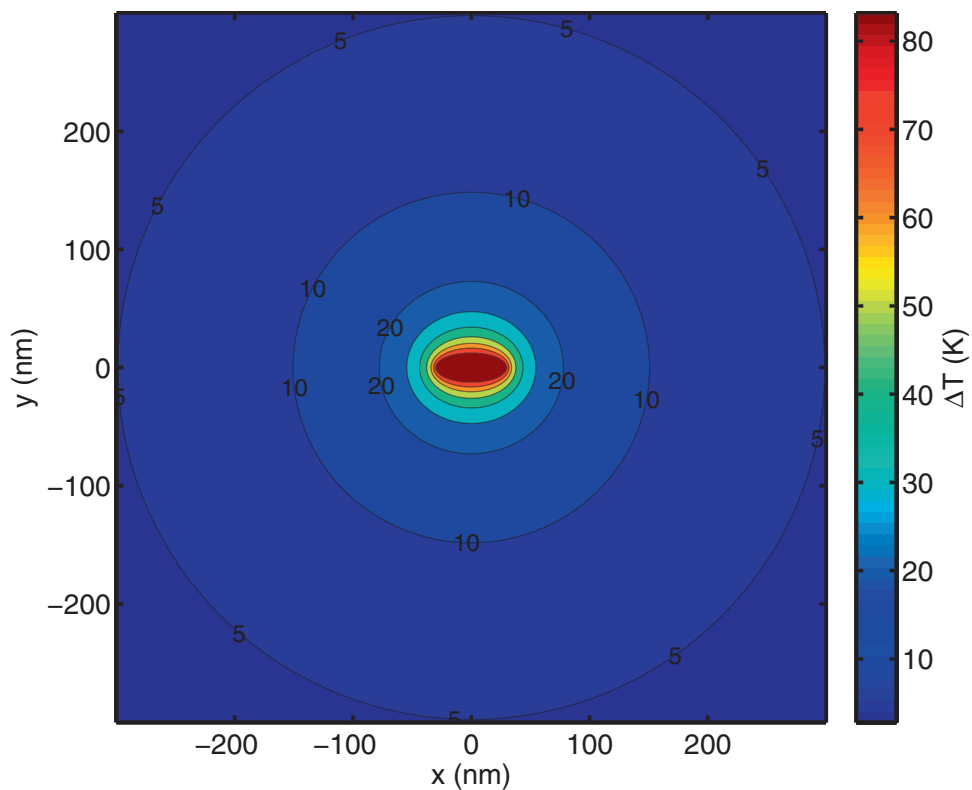


Figure G.2: Distribution of temperature around an ellipsoidal gold nanoparticle in water, 25x60 nm. Intensity $2.385 \cdot 10^{11} \text{ W/m}^2$, $\sigma_{\text{abs}} = 4.398 \cdot 10^{-17} \text{ m}^2$, $\Delta T_p = 83 \text{ K}$

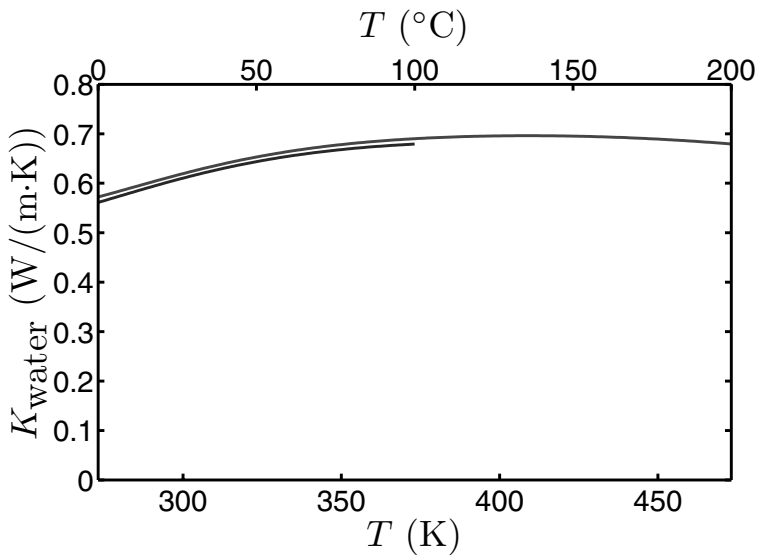


Figure G.3: Thermal conductivity of water as function of temperature, at 1 Atm. (bottom curve) and 200 Atm. (top curve). Data from NIST Chemistry Webbook.²¹⁸

Model of temperature dependent dynamics in the optical trap

In this appendix we provide an overview of the model of the temperature dependent dynamics of gold nanorods in the optical trap as presented in Chapter 4, and discuss the assumptions made. We apply the model to measurements on three individual nanorods, the nanorod from Figure 4.3 in Chapter 4, as well as two additional rods.

Assumptions in the model

The model used to fit all experimental data in Chapter 4 in a consistent way involves a fair number of assumptions. The most important ones are listed hereafter.

1. **Point-spread-function of the trap intensity** – As discussed in Chapter 3, the local intensity in the trap was consistent with an effective numerical aperture $NA = 1.0$. We took the intensity at the focus of a Gaussian beam with this NA to calculate the local intensity acting on the rod, neglecting the shift along the axis and further aberrations of the beam.
2. **Absorption cross-section of rod** – This was calculated in the dipole approximation for an ellipsoid. This neglects shape deviations of the

actual rod, which, to a good approximation, is a cylinder capped with two hemispheres. Moreover, we tuned the ellipsoid's aspect ratio to match the longitudinal plasmon frequency found in the experiment. In addition, we introduced corrections for spontaneous emission, and for electron scattering at the rod's surfaces. With this model, we found a good agreement of the spectrum, including the width. This broadening of the plasmon may be induced by temperature, or by thiol-PEG groups. The absorption cross-section found in this model was 30%-50% too large to account for the observed temperature rise.

3. **Radiation pressure** – The weak absorption of trap photons by the nanorod gives rise to a recoil force that shifts the nanorod from the trap's center by some 200-300 nm. This effect was neglected in the calculation of the local intensity and of the restoring forces, as well as any photophoretic effect caused by an inhomogeneous temperature profile within the nanorod.
4. **Friction coefficients** – The translational and rotational damping of the rod was calculated with Perrin's formulas²²⁵ for an ellipsoid, not for the cylindrical shape of the rod.
5. **Heat conduction around the rod** – We neglected the variation of the heat conductivity of water with temperature. Furthermore, we also neglected the effect of the PEG capping on heat conduction.
6. **Hot Brownian motion** – The effective viscosity for translation motion in the trap was taken as the one for free translational diffusion calculated by Rings et al.⁹⁰ This is a good approximation because the translational movement in the trap is slow, of the order of 100 μ s.
7. **Effective rotational viscosity** – To fit the measured dependence of rotational times on translational times (see Fig. 3 in the main text), we had to introduce an effective viscosity for rotation which was lower than the previous one for translation. Whereas this viscosity cannot be smaller than the viscosity of water at the temperature of the nanorod, we found that this minimum viscosity reproduces well the measured vibrational damping. Therefore, we kept this effective viscosity without further justification.
8. **Polarization inhomogeneity in the focus** – Although the trap light at the center of the focus is linearly polarized in the focal plane along the

polarization of the trap laser, the polarization state seen by the nanorod changes when it moves around. We have neglected all depolarization effects induced by the motion of the nanorod, assuming the position of the rod to be very close to the focus. The deviation from linear polarization of the trap light will induce slight orientational deviations of the rod, which do not follow Boltzmann's statistics. However, the correlation time of these fluctuations should be that of the translational diffusion, much longer than that of the rotational diffusion. Such orientational effects were not considered in the analysis of the translational correlation. Similarly, deviations from the center of the trap give rise to depolarization of the scattered light which was neglected.

9. **Gold heating** – The temperature change in the trap leads to a change of the optical response of gold. According to the literature,¹²³ this effect is small and was neglected.
10. **Polymer conformational changes** – All effects related to the temperature dependence of the polymer brush on the nanoparticles have been neglected. The only effect of the polymer we consider is the introduction of a temperature-independent change of hydrodynamic volume compared to that of the bare nanorod.

Trap characteristics for three nanorods

Here we discuss the results of the combined measurement of the spectral intensity ratio and the correlation times on a single particle. We performed the measurements on a set of three individual nanorods from the same sample under identical parameters of the optical trap. The nanorods have slightly different aspect ratios, as we can conclude from the measured scattering spectra with resonances at 617 nm, 624 nm and 636nm.

The results are shown in Fig. H.1, with the same series of measurements on each rod organized in vertical columns. The measurements in the first column are on the same nanorod as in Fig. 1 of Chapter 4, the second and third column display the results on two additional rods. Row (a-f-k) displays the measured spectral intensity ratios. The rotational trap stiffness κ_r deduced from this ratio using eq. E.6 is shown in row (b-g-l). The bottom three rows display the measured rotation and translation correlation times, and their ratio. All three nanorods display qualitatively the same behavior.

H Model of temperature dependent dynamics in the optical trap

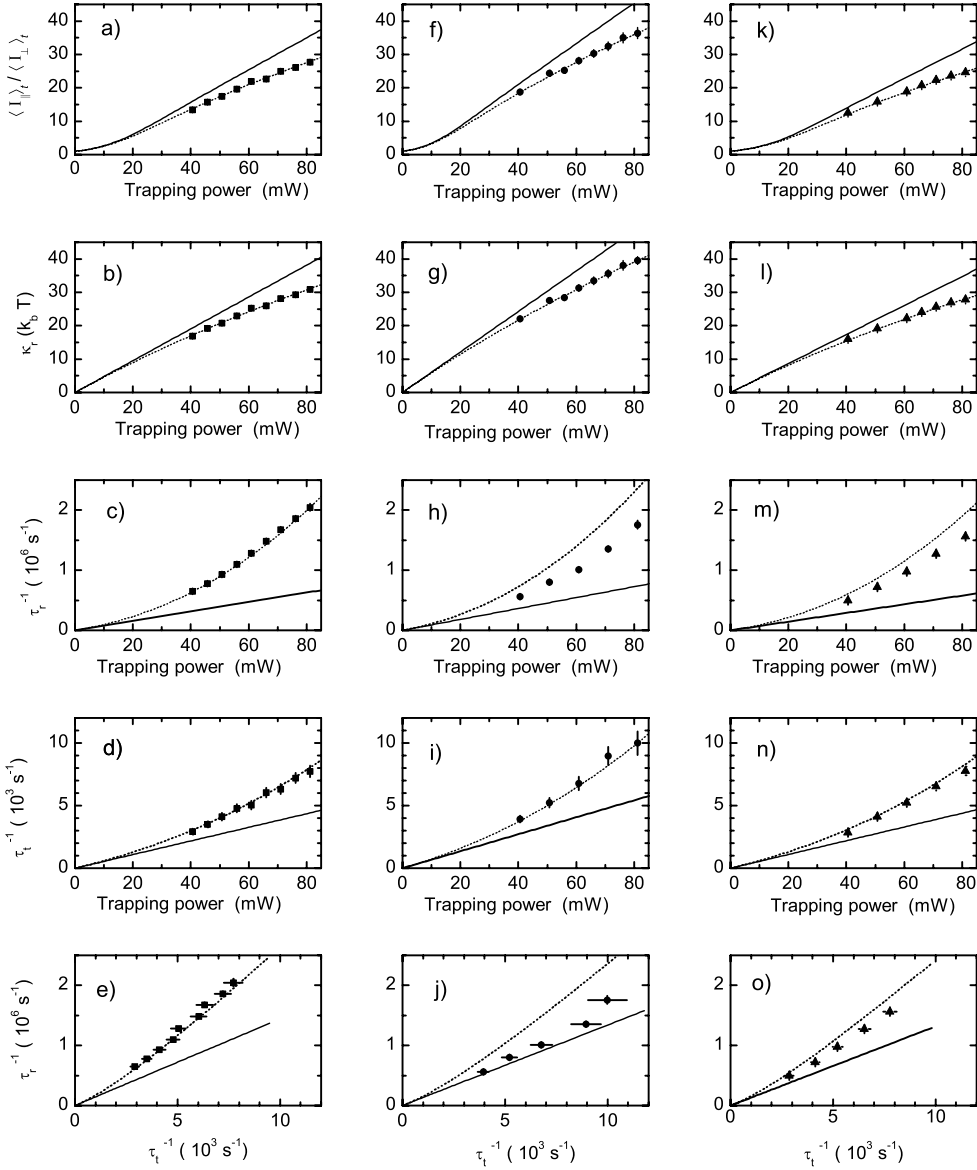


Figure H.1: Trap characteristics as functions of trapping power, for 3 individual gold nanorods, with resonance wavelength 624 nm (Column a-e, rod 1, the nanorod from Chapter 4), 636 nm (Column f-j, rod 2) and 617 nm (Column k-o, rod 3). See text for further details.

λ_L (nm)	κ_r ($k_B \widetilde{T}_B$)	V_p (10^4 nm^3)	κ_t ($10^{-6} \text{ pN nm}^{-1} \text{ mW}^{-1}$)	ΔT_p (K mW^{-1})
624 ± 1	30.9 ± 0.6	2.1 ± 0.1	8.8 ± 0.5	0.89 ± 0.1
636 ± 1	39.5 ± 1.0	2.5 ± 0.1	11.7 ± 1.0	0.89 ± 0.1
617 ± 1	27.8 ± 1.0	2.2 ± 0.1	8.8 ± 0.5	0.93 ± 0.1

Table H.1: Trapping parameters for the three nanorods of Fig. H.1. The wavelength of the longitudinal plasmon resonance λ_L is determined experimentally. The rotational trap stiffness κ_r is directly computed from the experimentally measured spectral intensity ratio $\langle I_{\parallel} \rangle_t / \langle I_{\perp} \rangle_t$ via equation E.6. The values for the particle volume V_p and the transverse trap stiffness κ_t are determined from the fitting procedure. The value of the intensity at the trap focus at an incident trapping power of 80 mW was taken for all three particles as $I_0 = 2.12 \cdot 10^{11} \text{ W/m}^2$. The hydrodynamic thickness of the PEG capping layer of the gold nanorods was fitted to 5 nm.

Overview of the fitting procedure

The vertical display sequence of the measurements in Fig. H.1 follows the procedure that was used to make a global fit of our model with an effective temperature \widetilde{T}_B and two effective viscosities η_r and η_t . In the model, the fitting parameters are the individual volumes of the three nanorods, the intensity of the trap laser, the effective hydrodynamic thickness of the capping layer of the rods and the transverse trap stiffness. For a given incident trap power, the measurements were fitted with a single intensity at the trap focus for all three particles. The hydrodynamic thickness of the capping layer was also kept the same for all three particles, independent of trapping power. The parameters determined from the fit are summarized in Table H.1.

Here we outline the sequence of steps in the procedure used to fit the parameters in the model.

1. The volume of the nanorods V_p and the intensity I_0 at the trap focus were fitted from the measurement of the spectral intensity ratio (row a-f-k). Via eq. E.6 this spectral intensity ratio can be directly related to the rotational trap stiffness κ_r , in units of $k_B T$ (row b-g-l). Since the rotational trap stiffness is proportional to both the trap intensity and the rod volume ($Re \{ \Delta \alpha \} \propto V_p$), the product of these two quantities can be fitted by matching the slope of the plot of κ_r versus trap power. The value for the intensity at the trap power can be fixed by demanding that the particle volume lies within the distribution of particle volumes measured from electron microscopy on the sample. Here, we still allow the volume of each of the three nanorods to be different, keeping the

H Model of temperature dependent dynamics in the optical trap

average volume equal to the ensemble volume.

2. The effective temperature \widetilde{T}_B for the orientation distribution can be found by fitting the observed curvature in the plot of κ_r versus trap power using a thermal energy that increases with trap power. Specifically, we evaluate the thermal energy as $k_B \widetilde{T}_B = k_B(T_0 + \Delta \widetilde{T}_B)$, where T_0 is the bath temperature and the effective temperature increase $\Delta \widetilde{T}_B$ is proportional to the trap intensity. As the effective temperature increases, the plot of κ_r vs trap power becomes sublinear.
3. Step 1 and 2 are optimized recursively until satisfactory agreement is obtained. The values for the intensity of the trap I_0 , the particle volume V_p and the effective temperature \widetilde{T}_B are now fixed.
4. With the trap intensity and particle volume determined, the model is adjusted to the measured correlation times in row c-h-m. The rotation times are given as $\tau_r = \zeta_r / (2\kappa_r)$. In the fit, we allow for an effective hydrodynamic volume V_{hyd} in the rotation friction coefficient ζ_r of the rod: $\zeta_r = \widetilde{\eta}_r V_{\text{hyd}} C_r$, with C_r a geometrical factor. The geometrical factor is taken as the one calculated for an ellipsoid (see Appendix D). In combination with the previously determined particle volume, the effective hydrodynamic volume determines the thickness of the capping layer. We adjust the hydrodynamic volumes of the three individual rod such that the thickness of the capping layer is the same for all three nanorods.
5. We find an effective rotational viscosity $\widetilde{\eta}_r$ as function of temperature by matching the observed curvature in the plot of rotation times versus trap power, using the known temperature dependence of the viscosity of water (Appendix D). Specifically, we evaluate the viscosity as $\widetilde{\eta}_r = \eta(T_0 + \Delta \widetilde{T}_r)$, where η is the viscosity of water and the effective temperature increase $\Delta \widetilde{T}_r$ is proportional to the trap intensity.
6. Step 4 and 5 are optimized recursively until satisfactory agreement is obtained. The values for the hydrodynamic thickness and the effective rotational viscosity η_r are now fixed.
7. We fit the transverse trap stiffness κ_t from the measured translation correlation times τ_t (row d-i-n) using the relation $\tau_t = \zeta_t / (2\kappa_t)$, where ζ_t is the friction coefficient for translations along the long axis of the rod. For the friction coefficient we use the value calculated for an ellipsoid

(Appendix D), taking into account the determined particle volume and the hydrodynamic thickness of the capping layer.

8. We find an effective translation viscosity η_t by matching the observed curvature in the plot of translation times versus power, using the known temperature dependence of the viscosity of water. Here we assume again that the increase of the particle temperature scales linearly with trapping power. However, in contrast to step 5, we evaluate the effective viscosities for translations as $\eta_t = \eta_{HBM}$, providing values for the effective temperature for Hot Brownian Motion T_{HBM} and the particle temperature T_p .
9. We interpret the values found for effective temperature \widetilde{T}_B and effective viscosities $\widetilde{\eta}_r$ and $\widetilde{\eta}_t$ in terms of a corresponding particle temperature T_p . This particle temperature can be compared to a temperature calculated independently from the absorption cross section calculated for a gold nanorod with the fitted volume and measured aspect ratio, and the fitted trap intensity (see Appendix G).

The measurements on all three nanorods are well described by our model, when we take the effective viscosity for rotations $\widetilde{\eta}_r$ as the viscosity at the particle temperature, and the effective temperature \widetilde{T}_B equal to the particle temperature. For simplicity, we have chosen to fit all three nanorods with the same hydrodynamic thickness of the PEG capping layer. The quality of the global fit could possibly be further improved by allowing for a variation of this parameter for the individual nanorods. This would be reasonable as the amount of PEG molecules may vary from rod to rod.

Bibliography

Bibliography

- [1] F. E. Wagner, S. Haslbeck, L. Stievano, S. Calogero, Q. A. Pankhurst, and K.-P. Martinek, "Before striking gold in gold-ruby glass," *Nature* **407**, 691–692 (2000).
- [2] M. Kerker, "The optics of colloidal silver: something old and something new," *J. Colloid Interface Sci.* **105**, 297–314 (1985).
- [3] M. Faraday, "The Bakerian lecture: experimental relations of gold (and other metals) to light," *Phil. Trans. R. Soc. London* **147**, 145–181 (1857).
- [4] G. Mie, "Beiträge zur optik trüber medien, speziell kolloidaler metallösungen," *Ann. Physik* **330**, 377–442 (1908).
- [5] U. Kreibig and M. Vollmer, *Optical Properties of Metal Clusters*, vol. 25 of *Springer Series in Materials Science* (Springer, Berlin, 1995).
- [6] C. F. Bohren and D. R. Huffman, *Absorption and Scattering of Light by Small Particles* (Wiley, 1998).
- [7] M. Kerker, *The scattering of light and other electromagnetic radiation* (Academic Press, Inc., London, 1969).
- [8] J. Yguerabide and E. E. Yguerabide, "Light-scattering submicroscopic particles as highly fluorescent analogs and their use as tracer labels in clinical and biological applications: II. Experimental characterization," *Anal. Biochem.* **262**, 157–176 (1998).
- [9] N. L. Rosi and C. A. Mirkin, "Nanostructures in biodiagnostics," *Chem. Rev.* **105**, 1547–1562 (2005).
- [10] S. Schultz, D. R. Smith, J. J. Mock, and D. A. Schultz, "Single-target molecule detection with nonbleaching multicolor optical immunolabels," *Proc. Natl. Acad. Sci. U. S. A.* **97**, 996–1001 (2000).

BIBLIOGRAPHY

- [11] G. Raschke, S. Kowarik, T. Franzl, C. Sönnichsen, T. A. Klar, J. Feldmann, A. Nichtl, and K. Kürzinger, "Biomolecular recognition based on single gold nanoparticle light scattering," *Nano Lett.* **3**, 935–938 (2003).
- [12] D. Spetzler, J. York, D. Daniel, R. Fromme, D. Lowry, and W. D. Frasch, "Microsecond time scale rotation measurements of single F₁-ATPase molecules," *Biochemistry* **45**, 3117–3124 (2006).
- [13] A. R. Dunn and J. A. Spudich, "Dynamics of the unbound head during myosin V processive translocation," *Nat. Struct. Mol. Biol.* **14**, 246–248 (2007).
- [14] X. Nan, P. A. Sims, and X. S. Xie, "Organelle tracking in a living cell with microsecond time resolution and nanometer spatial resolution," *Chem. Phys. Chem.* **9**, 707–712 (2008).
- [15] G. Louit, T. Asahi, G. Tanaka, T. Uwada, and H. Masuhara, "Spectral and 3-dimensional tracking of single gold nanoparticles in living cells studied by Rayleigh light scattering microscopy," *J. Phys. Chem. C* **113**, 11766–11772 (2009).
- [16] R. Ishmukhametov, T. Hornung, D. Spetzler, and W. D. Frasch, "Direct observation of stepped proteolipid ring rotation in *E. coli* F₀F₁ATPase," *EMBO J.* **29**, 3911–3923 (2010).
- [17] X. Huang, I. H. El-Sayed, W. Qian, and M. A. El-Sayed, "Cancer cell imaging and photothermal therapy in the near-infrared region by using gold nanorods," *J. Am. Chem. Soc.* **128**, 2115–2120 (2006).
- [18] A. D. McFarland and R. P. Van Duyne, "Single silver nanoparticles as real-time optical sensors with zeptomole sensitivity," *Nano Lett.* **3**, 1057–1062 (2003).
- [19] J. N. Anker, W. P. Hall, O. Lyandres, N. C. Shah, J. Zhao, and R. P. Van Duyne, "Biosensing with plasmonic biosensors," *Nature Mater.* **7**, 442–453 (2008).
- [20] P. J. Schuck, D. P. Fromm, A. Sundaramurthy, G. S. Kino, and W. E. Moerner, "Improving the mismatch between light and nanoscale objects with gold bowtie nanoantennas," *Phys. Rev. Lett.* **94**, 017402 (2005).

- [21] M. Fleischmann, P. J. Hendra, and A. J. McQuillan, "Raman spectra of pyridine adsorbed at a silver electrode," *Chem. Phys. Lett.* **26**, 163–166 (1974).
- [22] D. L. Jeanmaire and R. P. Van Duyne, "Surface Raman spectroelectrochemistry part I. Heterocyclic, aromatic, and aliphatic amines adsorbed on the anodized silver electrode," *J. Electroanal. Chem.* **84**, 1–20 (1977).
- [23] X.-M. Qian and S. M. Nie, "Single-molecule and single-nanoparticle SERS: from fundamental mechanisms to biomedical applications," *Chem. Soc. Rev.* **37**, 912–920 (2008).
- [24] P. Anger, P. Bharadwaj, and L. Novotny, "Enhancement and quenching of single-molecule fluorescence," *Phys. Rev. Lett.* **96**, 113002 (2006).
- [25] S. Kühn, U. Håkanson, L. Rogobete, and V. Sandoghdar, "Enhancement of single-molecule fluorescence using a gold nanoparticle as an optical nanoantenna," *Phys. Rev. Lett.* **97**, 017402 (2006).
- [26] A. Kinkhabwala, Z. Yu, S. Fan, Y. Avlasevich, K. Müllen, and W. E. Moerner, "Large single-molecule fluorescence enhancements produced by a bowtie nanoantenna," *Nature Photon.* **3**, 654–657 (2009).
- [27] A. G. Curto, G. Volpe, T. Taminiau, M. P. Kreuzer, R. Quidant, and N. F. van Hulst, "Unidirectional emission of a quantum dot coupled to a nanoantenna," *Science* **329**, 930–933 (2010).
- [28] A. Henglein, "Small-particle research: physicochemical properties of extremely small colloidal metal and semiconductor particles," *Chem. Rev.* **89**, 1861–1873 (1989).
- [29] A. Henglein, "Physicochemical properties of small metal particles in solution: "microelectrode" reactions, chemisorption, composite metal particles, and the atom-to-metal transition," *J. Phys. Chem.* **97**, 5457–5471 (1993).
- [30] G. Schmid and L. F. Chi, "Metal clusters and colloids," *Adv. Mater.* **10**, 515–526 (1998).
- [31] S. Link and M. A. El-Sayed, "Spectral properties and relaxation dynamics of surface plasmon electronic oscillations in gold and silver nanodots and nanorods," *J. Phys. Chem. B* **103**, 8410–8426 (1999).

BIBLIOGRAPHY

- [32] S. Link and M. A. El-Sayed, "Size and temperature dependence of the plasmon absorption of colloidal gold nanoparticles," *J. Phys. Chem. B* **103**, 4212–4217 (1999).
- [33] S. Link and M. A. El-Sayed, "Shape and size dependence of radiative, non-radiative and photothermal properties of gold nanocrystals," *Int. Rev. Phys. Chem.* **19**, 409–453 (2000).
- [34] C. Burda, X. Chen, R. Narayanan, and M. A. El-Sayed, "Chemistry and properties of nanocrystals of different shapes," *Chem. Rev.* **105**, 1025–1102 (2005).
- [35] P. K. Jain, X. Huang, I. H. El-Sayed, and M. A. El-Sayed, "Noble metals on the nanoscale: optical and photothermal properties and some applications in imaging, sensing, biology, and medicine," *Acc. Chem. Res.* **41**, 1578–1586 (2008).
- [36] G. V. Hartland, "Coherent excitation of vibrational modes in metallic nanoparticles," *Annu. Rev. Phys. Chem.* **57**, 403–430 (2006).
- [37] L. M. Liz-Marzán, "Tailoring surface plasmons through the morphology and assembly of metal nanoparticles," *Langmuir* **22**, 32–41 (2006).
- [38] J. Pérez-Juste, I. Pastoriza-Santos, L. M. Liz-Marzán, and P. Mulvaney, "Gold nanorods: synthesis, characterization, and applications," *Coord. Chem. Rev.* **249**, 1870–1901 (2005).
- [39] G. V. Hartland, "Optical studies of dynamics in noble metal nanostructures," *Chem. Rev.* **111**, 3858–3887 (2011).
- [40] T. Klar, M. Perner, S. Grosse, G. von Plessen, W. Spirkl, and J. Feldmann, "Surface plasmon resonances in single metallic nanoparticles," *Phys. Rev. Lett.* **80**, 4249–4252 (1998).
- [41] K. Mawatari, T. Kitomori, and T. Sawada, "Individual detection of single nanometer-sized particles in liquid by photothermal microscope," *Anal. Chem.* **70**, 5037–5041 (1998).
- [42] C. Sönnichsen, S. Geier, N. E. Hecker, G. von Plessen, J. Feldmann, H. Ditlbacher, B. Lamprecht, J. R. Krenn, F. R. Aussenegg, V. Z.-H. Chan, J. P. Spatz, and M. Möller, "Spectroscopy of single metallic nanoparticles using total internal reflection microscopy," *Appl. Phys. Lett.* **77**, 2949–2951 (2000).

- [43] D. Boyer, P. Tamarat, A. Maali, B. Lounis, and M. Orrit, "Photothermal imaging of nanometer-sized metal particles among scatterers," *Science* **297**, 1160–1163 (2002).
- [44] S. Berciaud, L. Cognet, G. A. Blab, and B. Lounis, "Photothermal heterodyne imaging of individual nonfluorescent nanoclusters and nanocrystals," *Phys. Rev. Lett.* **93**, 257402 (2004).
- [45] A. Arbouet, D. Christofilos, N. Del Fatti, F. Vallée, J. R. Huntzinger, L. Arnaud, P. Billaud, and M. Broyer, "Direct measurement of the single-metal-cluster optical absorption," *Phys. Rev. Lett.* **93**, 127401 (2004).
- [46] K. Lindfors, T. Kalkbrenner, P. Stoller, and V. Sandoghdar, "Detection and spectroscopy of gold nanoparticles using supercontinuum white light confocal microscopy," *Phys. Rev. Lett.* **93**, 037401 (2004).
- [47] M. Lippitz, M. A. van Dijk, and M. Orrit, "Third-harmonic generation from single gold nanoparticles," *Nano Lett.* **5**, 799802 (2005).
- [48] M. A. van Dijk, M. Lippitz, and M. Orrit, "Far-field optical microscopy of single metal nanoparticles," *Acc. Chem. Res.* **38**, 594–601 (2005).
- [49] M. A. van Dijk, A. L. Tchegotareva, M. Orrit, M. Lippitz, S. Berciaud, D. Lasne, L. Cognet, and B. Lounis, "Absorption and scattering microscopy of single metal nanoparticles," *Phys. Chem. Chem. Phys.* **8**, 3486–3495 (2006).
- [50] M. Pelton, J. Aizpurua, and G. Bryant, "Metal-nanoparticle plasmonics," *Laser Photonics Rev.* **2**, 136–159 (2008).
- [51] P. Zijlstra and M. Orrit, "Single metal nanoparticles: optical detection, spectroscopy and applications," *Rep. Prog. Phys.* **74**, 106401 (2011).
- [52] H. Lamb, "On the vibrations of an elastic sphere," *Proc. Lon. Mat. Soc.* **13**, 189–212 (1882).
- [53] V. A. Dubrovskiy and V. S. Morozhnik, "Natural vibrations of a spherical inhomogeneity in an elastic medium," *Izv. Earth Phys.* **17**, 494–504 (1981).
- [54] H. C. Berg, "How to track bacteria," *Rev. Sci. Instrum.* **42**, 868–871 (1971).

BIBLIOGRAPHY

- [55] J. Enderlein, "Tracking of fluorescent molecules diffusing within membranes," *Appl. Phys. B* **71**, 773–777 (2000).
- [56] H. Cang, C. M. Wong, C. S. Xu, A. H. Rizvi, and H. Yang, "Confocal three dimensional tracking of a single nanoparticle with concurrent spectroscopic readouts," *Appl. Phys. Lett.* **88**, 223901 (2006).
- [57] H. Cang, C. S. Xu, D. Montiel, and H. Yang, "Guiding a confocal microscope by single fluorescent nanoparticles," *Opt. Lett.* **32**, 2729–2731 (2007).
- [58] H. Cang, C. S. Xu, and H. Yang, "Progress in single-molecule tracking spectroscopy," *Chem. Phys. Lett.* **457**, 285–291 (2008).
- [59] D. Montiel and H. Yang, "Real-time three-dimensional single-particle tracking spectroscopy for complex systems," *Laser Photonics Rev.* **3**, 374–385 (2010).
- [60] A. E. Cohen and W. E. Moerner, "Method for trapping and manipulating nanoscale objects in solution," *App. Phys. Lett.* **86**, 093109 (2005).
- [61] A. E. Cohen, "Control of nanoparticles with arbitrary two-dimensional force fields," *Phys. Rev. Lett.* **94**, 118102 (2005).
- [62] A. E. Cohen and W. E. Moerner, "Suppressing Brownian motion of individual biomolecules in solution," *Proc. Natl. Acad. Sci. U. S. A.* **103**, 4362–4365 (2006).
- [63] A. P. Fields and A. E. Cohen, "Electrokinetic trapping at the one nanometer limit," *Proc. Natl. Acad. Sci. U. S. A.* **108**, 8937–8942 (2011).
- [64] M. Krishnan, N. Mojarad, P. Kukura, and V. Sandoghdar, "Geometry-induced electrostatic trapping of nanometric objects in a fluid," *Nature* **467**, 692–695 (2010).
- [65] A. Ashkin, "Application of laser radiation pressure," *Science* **210**, 1081–1088 (1980).
- [66] A. Ashkin, J. M. Dziedzic, J. E. Bjorkholm, and S. Chu, "Observation of a single-beam gradient force optical trap for dielectric particles," *Opt. Lett.* **11**, 288–290 (1986).
- [67] K. Svoboda and S. M. Block, "Biological applications of optical forces," *Annu. Rev. Biophys. Biomol. Struct.* **23**, 247–285 (1994).

- [68] C. Bustamante, Y. R. Chemla, N. R. Forde, and D. Izhaky, "Mechanical processes in biochemistry," *Annu. Rev. Biochem.* **73**, 705–748 (2004).
- [69] J. R. Moffitt, Y. R. Chemla, S. B. Smith, and C. Bustamante, "Recent advances in optical tweezers," *Annu. Rev. Biochem.* **77**, 19 (2008).
- [70] K. C. Neuman and A. Nagy, "Single-molecule force spectroscopy: optical tweezers, magnetic tweezers and atomic force microscopy," *Nature Methods* **5**, 491–505 (2008).
- [71] D. G. Grier, "A revolution in optical manipulation," *Nature* **424**, 810 (2003).
- [72] K. Dholakia, P. Reece, and M. Gu, "Optical micromanipulation," *Chem. Soc. Rev.* **37**, 42–55 (2008).
- [73] C. Veigel and C. F. Schmidt, "Moving into the cell: single-molecule studies of molecular motors in complex environments," *Nat. Rev. Mol. Cell Biol.* **12**, 163–176 (2011).
- [74] K. Svoboda and S. M. Block, "Optical trapping of metallic Rayleigh particles," *Opt. Lett.* **19**, 930–932 (1994).
- [75] P. M. Hansen, V. K. Bhatia, N. Harrit, and L. Oddershede, "Expanding the optical trapping range of gold nanoparticles," *Nano Lett.* **5**, 1937–1942 (2005).
- [76] F. Hajizadeh and S. N. S. Reihani, "Optimized optical trapping of gold nanoparticles," *Opt. Express* **18**, 551–559 (2010).
- [77] Y. Seol, A. E. Carpenter, and T. T. Perkins, "Gold nanoparticles: enhanced optical trapping and sensitivity coupled with significant heating," *Opt. Lett.* **31**, 2429–2431 (2006).
- [78] L. Bosanac, T. Aabo, P. Bendix, and L. Oddershede, "Efficient optical trapping and visualization of silver nanoparticles," *Nano Lett.* **8**, 1486–1491 (2008).
- [79] C. Selhuber-Unkel, I. Zins, O. Schubert, C. Sönnichsen, and L. B. Oddershede, "Quantitative optical trapping of single gold nanorods," *Nano Lett.* **8**, 2998–3003 (2008).

BIBLIOGRAPHY

- [80] M. Pelton, M. Liu, H. Y. Kim, G. Smith, P. Guyot-Sionnest, and N. F. Scherer, "Optical trapping and alignment of single gold nanorods by using plasmon resonances," *Opt. Lett.* **31**, 2075–2077 (2006).
- [81] K. C. Toussaint, M. Liu, M. Pelton, J. Pesic, M. J. Guffey, P. Guyot-Sionnest, and N. F. Scherer, "Plasmon resonance-based optical trapping of single and multiple Au nanoparticles," *Opt. Express* **15**, 12017–12029 (2007).
- [82] M. Dienerowitz, M. Mazilu, P. J. Reece, T. J. Krauss, and K. Dholakia, "Optical vortex trap for resonant confinement of metal nanoparticles," *Opt. Express* **16**, 4991–4999 (2008).
- [83] Y. Jiang, T. Narushima, and H. Okamoto, "Nonlinear optical effects in trapping nanoparticles with femtosecond pulses," *Nature Phys.* **6**, 1005–1009 (2010).
- [84] L. Tong, V. D. Miljković, and M. Käll, "Alignment, rotation, and spinning of single plasmonic nanoparticles and nanowires using polarization dependent optical forces," *Nano Lett.* **10**, 268–273 (2010).
- [85] L. Tong, V. D. Miljković, P. Johansson, and M. Käll, "Plasmon hybridization reveals the interaction between individual colloidal gold nanoparticles confined in an optical potential well," *Nano Lett.* **11**, 4505–4508 (2011).
- [86] J. Prikulis, F. Svedberg, and M. Käll, "Optical spectroscopy of single trapped metal nanoparticles in solution," *Nano Lett.* **4**, 115–118 (2004).
- [87] M. Dienerowitz, M. Mazilu, and K. Dholakia, "Optical manipulation of nanoparticles: a review," *J. Nanophotonics* **2**, 021875 (2008).
- [88] P. M. Bendix, S. N. S. Reihani, and L. B. Oddershede, "Direct measurements of heating by electromagnetically trapped gold nanoparticles on supported lipid bilayers," *ACS NANO* **4**, 2256–2262 (2010).
- [89] A. Kyrsting, P. M. Bendix, D. G. Stamou, and L. B. Oddershede, "Heat profiling of three-dimensionally optically trapped gold nanoparticles using vesicle cargo release," *Nano Lett.* **11**, 888–892 (2011).
- [90] D. Rings, R. Schachoff, M. Selmke, F. Cichos, and K. Kroy, "Hot Brownian motion," *Phys. Rev. Lett.* **105**, 090604 (2010).

- [91] D. Rings, M. Selmke, F. Cichos, and K. Kroy, "Theory of hot Brownian motion," *Soft Matter* **7**, 3441–3452 (2011).
- [92] D. Chakraborty, M. V. Gnann, D. Rings, J. Glaser, O. Otto, F. Cichos, and K. Kroy, "Generalized Einstein relation for hot Brownian motion," *Europhys. Lett.* **96**, 60009 (2011).
- [93] M. Terazima, N. Hirota, S. E. Braslavsky, A. Mandelis, S. E. Bialkowski, G. J. Diebold, R. J. D. Miller, D. Fournier, A. R. Palmer, and A. Tam, "Quantities, terminology, and symbols in photothermal and related spectroscopies," *Pure Appl. Chem.* **76**, 1083–1118 (2004).
- [94] S. E. Bialkowski, *Photothermal spectroscopy methods for chemical analysis* (Wiley, New York, 1996).
- [95] M. Tokeshi, M. Uchida, A. Hibara, T. Sawada, and T. Kitamori, "Determination of subyoctomole amount of nonfluorescent molecules using a thermal lens microscope: subsingle-molecule determination," *Anal. Chem.* **73**, 2112–2116 (2001).
- [96] D. Boyer, P. Tamarat, A. Maali, M. Orrit, and B. Lounis, "Imaging single metal nanoparticles in scattering media by photothermal interference contrast," *Physica E* **17**, 537–540 (2003).
- [97] S. Berciaud, L. Cognet, P. Tamarat, and B. Lounis, "Observation of intrinsic size effects in the optical response of individual gold nanoparticles," *Nano Lett.* **5**, 515–518 (2005).
- [98] S. Berciaud, L. Cognet, and B. Lounis, "Photothermal absorption spectroscopy of individual semiconductor nanocrystals," *Nano Lett.* **5**, 2160–2163 (2005).
- [99] S. Berciaud, L. Cognet, P. Poulin, R. B. Weisman, and B. Lounis, "Absorption spectroscopy of individual single walled carbon nanotubes," *Nano Lett.* **7**, 1203–1207 (2007).
- [100] S. Berciaud, D. Lasne, G. A. Blab, L. Cognet, and B. Lounis, "Photothermal heterodyne imaging of individual metallic nanoparticles : Theory versus experiment," *Phys. Rev. B* **73**, 045424 (2006).
- [101] L. Cognet, S. Berciaud, D. Lasne, I. Alexandre, D. Husar, J. Remacle, and B. Lounis, "Photothermal methods for single nonluminescent nano-objects," *Anal. Chem.* **80**, 2288–2294 (2008).

BIBLIOGRAPHY

- [102] G. A. Blab, L. Cognet, S. Berciaud, I. Alexandre, D. Husar, J. Remacle, and B. Lounis, "Optical readout of gold nanoparticles-based DNA microarrays without silver enhancement," *Biophys. J.* **90**, L13–L15 (2006).
- [103] L. Cognet, C. Tardin, D. Boyer, D. Choquet, P. Tamarat, and B. Lounis, "Single metallic nanoparticle imaging for protein detection in cells," *Proc. Natl. Acad. Sci. U. S. A.* **100**, 11350–11355 (2003).
- [104] D. Lasne, G. A. Blab, S. Berciaud, M. Heine, L. Groc, D. Choquet, L. Cognet, and B. Lounis, "Single nanoparticle photothermal tracking (SNaPT) of 5-nm gold beads in live cells," *Biophys. J.* **91**, 4598–4604 (2006).
- [105] F. Kulzer, N. Laurens, J. Besser, T. Schmidt, and M. Orrit, "Photothermal detection of individual gold nanoparticles: perspectives for high-throughput screening," *ChemPhysChem* **9**, 1761–1766 (2008).
- [106] P. M. R. Paulo, A. Gaiduk, F. Kulzer, S. F. G. Krens, H. P. Spaink, and T. Schmidt, "Photothermal correlation spectroscopy of gold nanoparticles in solution," *J. Phys. Chem. C* **113**, 11451–11457 (2009).
- [107] R. Radunz, D. Rings, K. Kroy, and F. Cichos, "Hot Brownian particles and photothermal correlation spectroscopy," *J. Phys. Chem. A* **113**, 1674–1677 (2009).
- [108] V. Oceau, L. Cognet, L. Dushesne, D. Lasne, N. Schaeffer, D. G. Fernig, and B. Lounis, "Photothermal absorption correlation spectroscopy," *ACS NANO* **3**, 345–350 (2009).
- [109] D. Lasne, G. A. Blab, F. De Giorgi, F. Ichas, B. Lounis, and L. Cognet, "Label-free optical imaging of mitochondria in live cells," *Opt. Express* **15**, 14181–14193 (2007).
- [110] W.-S. Chang, J. W. Ha, L. S. Slaughter, and S. Link, "Plasmonic nanorod absorbers as orientation sensors," *Proc. Natl. Acad. Sci. U. S. A.* **107**, 2781–2786 (2010).
- [111] M. Atlan, M. Gross, P. Desbiolles, E. Absil, G. Tessier, and M. Coppey-Moisan, "Heterodyne holographic microscopy of gold particles," *Opt. Lett.* **33**, 500–502 (2008).

- [112] E. Absil, G. Tessier, M. Gross, M. Atlan, N. Warnasooriya, S. Suck, M. Coppey-Moisan, and D. Fournier, "Photothermal heterodyne holography of gold nanoparticles," *Opt. Express* **18**, 780–786 (2010).
- [113] P. B. Johnson and R. W. Christy, "Optical constants of the noble metals," *Phys. Rev. B* **6**, 4370–4379 (1972).
- [114] S. Link and M. A. El-Sayed, "Spectroscopic determination of the melting energy of a gold nanorod," *J. Chem. Phys.* **114**, 2362–2368 (2001).
- [115] P. Zijlstra, J. W. M. Chon, and M. Gu, "White light scattering spectroscopy and electron microscopy of laser induced melting in single gold nanorods," *Phys. Chem. Chem. Phys.* **11**, 5915–5921 (2009).
- [116] R. Dorn, S. Quabis, and G. Leuchs, "Sharper focus for a radially polarized light beam," *Phys. Rev. Lett.* **91**, 233901 (2003).
- [117] S. Moehl, H. Zhao, B. Dal Don, S. Wachter, and H. Kalt, "Solid immersion lens-enhanced nano-photoluminescence: principle and applications," *J. Appl. Phys.* **93**, 6265–6272 (2003).
- [118] S. N. S. Reihani, M. A. Charsooghi, H. R. Khalesifard, and R. Golestian, "Efficient in-depth trapping with an oil-immersion objective lens," *Opt. Lett.* **31**, 766–768 (2006).
- [119] B. Nikoobakht and M. A. El-Sayed, "Preparation and growth mechanism of gold nanorods (NRs) using seed-mediated growth method," *Chem. Mater.* **15**, 1957–1962 (2003).
- [120] C. Fernández-López, C. Mateo-Mateo, R. A. Álvarez Puebla, J. Pérez-Juste, I. Pastoriza-Santos, and L. M. Liz-Marzán, "Highly controlled silica coating of PEG-capped metal nanoparticles and preparation of SERS-encoded particles," *Langmuir* **25**, 13894–13899 (2009).
- [121] C. Novo, D. Gomez, J. Pérez-Juste, Z. Zhang, H. Petrova, M. Reismann, P. Mulvaney, and G. V. Hartland, "Contributions from radiation damping and surface scattering to the linewidth of the longitudinal plasmon band of gold nanorods: a single particle study," *Phys. Chem. Chem. Phys.* **8**, 3540–3546 (2006).
- [122] M. A. Garcia, J. de la Venta, P. Crespo, J. Llopis, S. Penadés, A. Fernández, and A. Hernando, "Surface plasmon resonance of capped Au nanoparticles," *Phys. Rev. B* **72**, 241403 (2005).

BIBLIOGRAPHY

- [123] M. Liu, M. Pelton, and P. Guyot-Sionnest, "Reduced damping of surface plasmons at low temperatures," *Phys. Rev. B* **79**, 035418 (2009).
- [124] P. C. Chaumet and M. Nieto-Vesperinas, "Time-averaged total force on a dipolar sphere in an electromagnetic field," *Opt. Lett.* **25**, 1065 (2000).
- [125] H. Petrova, J. Perez Juste, I. Pastoriza-Santos, G. V. Hartland, L. M. Liz-Marzán, and P. Mulvaney, "On the temperature stability of gold nanorods: comparison between thermal and ultrafast laser-induced heating," *Phys. Chem. Chem. Phys.* **8**, 814–821 (2006).
- [126] K. C. Neuman and S. M. Block, "Optical trapping," *Rev. Sci. Instrum.* **75**, 2787–2809 (2004).
- [127] F. Perrin, "Mouvement brownien d'un ellipsoïde (I). Dispersion diélectrique pour des molécules ellipsoïdales," *J. Phys. Radium* **VII**, 497–511 (1934).
- [128] M. M. Tirado and J. G. D. L. Torre, "Translational friction coefficients of rigid, symmetric top macromolecules. application to circular cylinders," *J. Chem. Phys.* **71**, 2581–2587 (1979).
- [129] M. M. Tirado and J. G. de la Torre, "Rotational dynamics of rigid, symmetric top macromolecules. Application to circular cylinders," *J. Chem. Phys.* **73**, 1986 (1980).
- [130] R. Bar-Ziv, A. Meller, T. Tlusty, E. Moses, J. Stavans, and S. A. Safran, "Localized dynamic light scattering: probing single particle dynamics at the nanoscale," *Phys. Rev. Lett.* **79**, 154–157 (1997).
- [131] A. Meller, R. Bar-Ziv, T. Tlusty, E. Moses, J. Stavans, and S. A. Safran, "Localized dynamic light scattering: a new approach to dynamic measurements in optical microscopy," *Biophys. J.* **74**, 1541–1548 (1998).
- [132] B. M. I. van der Zande, J. K. G. Dhont, M. R. Böhmer, and A. P. Philipse, "Colloidal dispersions of gold rods characterized by dynamic light scattering and electrophoresis," *Langmuir* **16**, 459–464 (2000).
- [133] J. Rodríguez-Fernández, J. Pérez-Juste, L. M. Liz-Marzán, and P. R. Lang, "Dynamic light scattering of short Au rods with low aspect ratios," *J. Phys. Chem. C* **111**, 5020–5025 (2007).

- [134] M. E. J. Friese, T. A. Nieminen, N. R. Heckenberg, and H. Rubinsztein-Dunlop, "Optical alignment and spinning of laser-trapped microscopic particles," *Nature* **394**, 348–350 (1998).
- [135] A. I. Bishop, T. A. Nieminen, N. R. Heckenberg, and H. Rubinsztein-Dunlop, "Optical microrheology using rotating laser-trapped particles," *Phys. Rev. Lett.* **92**, 198184 (2004).
- [136] A. La Porta and M. D. Wang, "Optical torque wrench: Angular trapping, rotation, and torque detection of quartz microparticles," *Phys. Rev. Lett.* **92**, 190801 (2004).
- [137] C. Deufel, S. Forth, C. R. Simmons, S. Dejgosh, and M. D. Wang, "Nanofabricated quartz cylinders for angular trapping: DNA supercoiling torque detection," *Nat. Methods* **4**, 223–225 (2007).
- [138] C. Sönnichsen, T. Franzl, T. Wilk, G. von Plessen, J. Feldmann, O. Wilson, and P. Mulvaney, "Drastic reduction of plasmon damping in gold nanorods," *Phys. Rev. Lett.* **88**, 077402 (2002).
- [139] S. Li, K. Zhang, J. M. Yang, L. Lin, and H. Yang, "Single quantum dots as local temperature markers," *Nano Lett.* **7**, 3102–3105 (2007).
- [140] G. Baffou, M. P. Kreuzer, F. Kulzer, and R. Quidant, "Temperature mapping near plasmonic nanostructures using fluorescence polarization anisotropy," *Opt. Express* **17**, 3291–3298 (2009).
- [141] J. M. Yang, H. Yang, and L. Lin, "Quantum dot nano thermometers reveal heterogeneous local thermogenesis in living cells," *ACS NANO* **5**, 5067–5071 (2011).
- [142] E. J. G. Peterman, F. Gittes, and C. Schmidt, "Laser-induced heating in optical traps," *Biophys. J.* **84**, 1308–1316 (2003).
- [143] L. M. Liz-Marzán, M. Giersig, and P. Mulvaney, "Synthesis of nano-sized gold–silica core–shell particles," *Langmuir* **12**, 4329–4335 (1996).
- [144] J. A. McKay and J. A. Rayne, "Temperature dependence of the infrared absorptivity of the noble metals," *Phys. Rev. B* **13**, 673–685 (1976).
- [145] P. Winsemius, "Temperature dependence of the optical properties of Au and Ag," Ph.D. thesis, Leiden University (1973).

BIBLIOGRAPHY

- [146] J. N. Hodgson, "The optical properties of gold," *J. Phys. Chem. Solids* **29**, 2175–2181 (1968).
- [147] G. P. Pells and M. Shiga, "The optical properties of copper and gold as a function of temperature," *J. Phys. C* **2**, 1835–1846 (1969).
- [148] M.-L. Thève, "Investigation of the optical properties of Au by means of thin semitransparent films," *Phys. Rev. B* **2**, 3060–3078 (1970).
- [149] O. Hunderi, "Influence of grain boundaries and lattice defects on the optical properties of some metals," *Phys. Rev. B* **7**, 3419–3429 (1973).
- [150] P. Winsemius, M. Guerrisi, and R. Rosei, "Splitting of the absorption edge in Au: temperature dependence," *Phys. Rev. B* **12**, 4570–4572 (1975).
- [151] S. N. S. Reihani and L. B. Oddershede, "Optimizing immersion media refractive index improves optical trapping by compensating spherical aberrations," *Opt. Lett.* **32**, 1998–2000 (2007).
- [152] H. Portales, N. Goubet, L. Saviot, S. Adichtchev, D. B. Murray, A. Mermet, E. Duval, and M. P. Pileni, "Probing atomic ordering and multiple twinning in metal nanocrystals through their vibrations," *Proc. Natl. Acad. Sci. U. S. A.* **105**, 14784–14789 (2008).
- [153] M. Fujii, T. Nagareda, S. Hayashi, and K. Yamamoto, "Low-frequency Raman scattering from small silver particles embedded in SiO₂ thin films," *Phys. Rev. B* **44**, 6243–6248 (1991).
- [154] M. Nisoli, S. De Silvestri, A. Cavalleri, A. M. Malvezzi, A. Stella, G. Lanzani, P. Cheyssac, and R. Kofman, "Coherent acoustic oscillations in metallic nanoparticles generated with femtosecond optical pulses," *Phys. Rev. B* **55**, R13424–R13427 (1997).
- [155] J. H. Hodak, I. Martini, and G. V. Hartland, "Observation of acoustic quantum beats in nanometer sized Au particles," *J. Chem. Phys.* **108**, 9210–9213 (1998).
- [156] N. Del Fatti, C. Voisin, F. Chevy, F. Vallée, and C. Flytzanis, "Coherent acoustic mode oscillation and damping in silver nanoparticles," *J. Chem. Phys.* **110**, 11484–11487 (1999).

- [157] V. Juvé, A. Crut, P. Maioli, M. Pellarin, M. Broyer, N. Del Fatti, and F. Vallée, "Probing elasticity at the nanoscale: Terahertz acoustic vibration of small metal nanoparticles," *Nano Lett.* **10**, 1853–1858 (2010).
- [158] Y. T. Yang, C. Callegari, X. L. Feng, K. L. Ekinici, and M. L. Roukes, "Zeptogram-scale nanomechanical mass sensing," *Nano Lett.* **6**, 583–586 (2006).
- [159] S. S. Verbridge, L. M. Bellan, J. M. Parpia, and H. G. Craighead, "Optically driven resonance of nanoscale flexural oscillators in liquid," *Nano Lett.* **6**, 2109–2114 (2006).
- [160] J. L. Arlett and M. L. Roukes, "Ultimate and practical limits of fluid-based mass detection with suspended microchannel resonators," *J. Appl. Phys.* **108**, 084701 (2010).
- [161] Q. P. Unterreithmeier, T. Faust, and J. P. Kotthaus, "Damping of nanomechanical resonators," *Phys. Rev. Lett.* **105**, 027205 (2010).
- [162] C. Voisin, D. Christofilos, N. Del Fatti, and F. Vallée, "Environment effect on the acoustic vibration of metal nanoparticles," *Physica B* **316**, 89–94 (2002).
- [163] M. Pelton, J. E. Sader, J. Burgin, M. Liu, P. Guyot-Sionnest, and D. Gosztola, "Damping of acoustic vibrations in gold nanoparticles," *Nat. Nanotechnol.* **4**, 492–495 (2009).
- [164] M. A. van Dijk, M. Lippitz, and M. Orrit, "Detection of acoustic oscillations of single gold nanospheres by time-resolved interferometry," *Phys. Rev. Lett.* **95**, 267406 (2005).
- [165] M. A. van Dijk, "Non-linear optical studies of single gold nanoparticles," Ph.D. thesis, Leiden University, Leiden (2007).
- [166] P. Zijlstra, A. L. Tchegotareva, J. W. M. Chon, M. Gu, and M. Orrit, "Acoustic oscillations and elastic moduli of single gold nanorods," *Nano Lett.* **8**, 3493–3497 (2008).
- [167] H. Staleva and G. V. Hartland, "Transient absorption studies of single silver nanocubes," *J. Phys. Chem. C* **112**, 7537–7539 (2008).
- [168] H. Staleva and G. V. Hartland, "Vibrational dynamics of silver nanocubes and nanowires studied by single-particle transient absorption spectroscopy," *Adv. Funct. Mater.* **18**, 3809–3817 (2008).

BIBLIOGRAPHY

- [169] J. Burgin, P. Langot, N. Del Fatti, F. Vallée, W. Huang, and M. A. El-Sayed, "Time-resolved investigation of the acoustic vibration of a single gold nanoprisma pair," *J. Phys. Chem. C* **112**, 11231–11235 (2008).
- [170] A. L. Tchebotareva, M. A. van Dijk, P. V. Ruijgrok, V. Fokkema, M. H. S. Hesselberth, and M. Orrit, "Acoustic and optical modes of single dumbbells of gold nanoparticles," *ChemPhysChem* **10**, 114–114 (2009).
- [171] A. L. Tchebotareva, P. V. Ruijgrok, P. Zijlstra, and M. Orrit, "Probing the acoustic vibrations of single metal nanoparticles by ultrashort laser pulses," *Laser Photonics Rev.* **4**, 581–597 (2010).
- [172] T. Schumacher, K. Kratzer, D. Molnar, M. Hentschel, H. Giessen, and M. Lippitz, "Nanoantenna-enhanced ultrafast nonlinear spectroscopy of a single gold nanoparticle," *Nat. Commun.* **2**, 333 (2011).
- [173] R. Marty, A. Arbouet, A. Girard, C. Mlayah, V. Paillard, V. K. Lin, S. L. Teo, and S. Tripathy, "Damping of the acoustic vibrations of individual gold nanoparticles," *Nano Lett.* **11**, 3301–3306 (2011).
- [174] P. V. Ruijgrok, N. R. Verhart, P. Zijlstra, A. L. Tchebotareva, and M. Orrit, "Brownian fluctuations and heating of an optically aligned gold nanorod," *Phys. Rev. Lett.* **107**, 037401 (2011).
- [175] L. Saviot and D. B. Murray, "Long lived acoustic vibrational modes of an embedded nanoparticle," *Phys. Rev. Lett.* **93**, 055506 (2004).
- [176] D. B. Murray and L. Saviot, "Phonons in an inhomogeneous continuum: Vibrations of an embedded nanoparticle," *Phys. Rev. B* **69**, 094305 (2004).
- [177] D. B. Murray and L. Saviot, "Acoustic vibrations of embedded spherical nanoparticles," *Physica E* **26**, 417–421 (2005).
- [178] L. Saviot, C. H. Netting, and D. B. Murray, "Damping by bulk and shear viscosity of confined acoustic phonons for nanostructures in aqueous solution," *J. Phys. Chem. B* **111**, 7457–7461 (2007).
- [179] M. Perner, S. Gresillon, J. Marz, G. von Plessen, J. Feldmann, J. Porstendorfer, K. J. Berg, and G. Berg, "Observation of hot-electron pressure in the vibration dynamics of metal nanoparticles," *Phys. Rev. Lett.* **85**, 792–795 (2000).

- [180] L. Saviot, B. Champagnon, E. Duval, I. A. Kudriavtsev, and A. I. Eki-mov, "Size dependence of acoustic and optical vibrational modes of CdSe nanocrystals in glasses," *J. Non-Cryst. Solids* **197**, 238–246 (1996).
- [181] V. Juvé, M. Scardamaglia, P. Maioli, A. Crut, S. Merabia, L. Joly, N. Del Fatti, and F. Vallée, "Cooling dynamics and thermal interface resistance of glass embedded metal nanoparticles," *Phys. Rev. B* **80**, 195406 (2010).
- [182] A. Plech, V. Kotaidis, S. Grésillon, S. Dahmen, and G. von Plessen, "Laser-induced heating and melting of gold nanoparticles studied by time resolved x-ray scattering," *Phys. Rev. B* **70**, 195423 (2004).
- [183] F. Cooper, "Heat transfer from a sphere to an infinite medium," *Int. J. Heat Mass Transfer.* **20**, 991–993 (1977).
- [184] G. Woan, *The Cambridge Handbook of physics formulas* (Cambridge University Press, Cambridge, 2000).
- [185] L. D. Marks, "Experimental studies of small particle structures," *Rep. Prog. Phys.* **57**, 603–649 (1994).
- [186] Z. L. Wang, "Transmission electron microscopy of shape-controlled nanocrystals and their assemblies," *J. Phys. Chem. B* **104**, 1153–1175 (2000).
- [187] J. Kimling, M. Maier, V. Okenve, V. Kotaidis, H. Ballot, and A. Plech, "Turkevitch method for gold nanoparticle synthesis revisited," *J. Phys. Chem. B* **110**, 15700–15707 (2006).
- [188] Z. L. Wang, R. P. Gao, B. Nikoobakht, and M. A. El-Sayed, "Surface reconstruction of the unstable {110} surface in gold nanorods," *J. Phys. Chem. B* **104**, 5415–4420 (2000).
- [189] H. Katz-Boon, C. J. Rossouw, M. Weyland, A. M. Funston, P. Mulvaney, and J. Etheridge, "Three-dimensional morphology and crystallography of gold nanorods," *Nano Lett.* **11**, 273–278 (2011).
- [190] E. Carbó-Argibay, B. Rodríguez-González, S. Gómez-Graña, A. Guerrero-Martínez, I. Pastoriza-Santos, J. Pérez Juste, and L. M. Liz-Marzán, "The crystalline structure of gold nanorods revisited: evidence for higher-index lateral facets," *Angew. Chem.* **122**, 9587–9590 (2010).

BIBLIOGRAPHY

- [191] M. Hu, X. Wang, G. V. Hartland, P. Mulvaney, J. Pérez Juste, and J. E. Sader, "Vibrational response of nanorods to ultrafast laser induced heating: Theoretical and experimental analysis," *J. Am. Chem. Soc.* **125**, 14925–14933 (2003).
- [192] C. J. Orendorff and C. J. Murphy, "Quantification of metal content in the silver-assisted growth of gold nanorods," *J. Phys. Chem. B* **110**, 3990–3994 (2006).
- [193] A. S. Nowick and B. S. Berry, *Anelastic relaxation in crystalline solids* (Academic Press, New York, 1972).
- [194] F. W. Beil, R. H. Blick, A. Wixforth, W. Wegschneider, D. Schuh, and M. Bichler, "Observation of single-defect relaxation in a freely suspended nano-resonator," *Europhys. Lett.* **76**, 1207–1213 (2006).
- [195] A. Venkatesan, K. Lulla, M. J. Patton, A. D. Armour, C. J. Mellor, and J. R. Owers-Bradley, "Dissipation due to two-level systems in gold nanomechanical resonators," *Phys. Rev. B* **81**, 073410 (2010).
- [196] J. W. Tucker and V. W. Rampton, *Microwave ultrasonics in solid state physics* (North-Holland Publishing company, Amsterdam, 1972).
- [197] R. Truell, C. Elbaum, and B. B. Chick, *Ultrasonic methods in solid state physics* (Academic Press, New York, 1969).
- [198] D. Rings, D. Chakraborty, and K. Kroy, "Rotational hot Brownian motion," arXiv:1203.3221v1 (2012).
- [199] M. J. Guffey, R. L. Miller, S. K. Gray, and N. F. Scherer, "Plasmon-driven selective deposition of Au bipyramidal nanoparticles," *Nano Lett.* **11**, 4058–4066 (2011).
- [200] A. S. Urban, A. A. Lutich, F. D. Stefani, and J. Feldmann, "Laser printing single gold nanoparticles," *Nano Lett.* **10**, 4794–4798 (2010).
- [201] I. M. Vellekoop and A. P. Mosk, "Focusing coherent light through opaque strongly scattering media," *Opt. Lett.* **32**, 2309–2311 (2007).
- [202] I. M. Vellekoop, A. Lagendijk, and A. P. Mosk, "Exploiting disorder for perfect focusing," *Nature Photon.* **4**, 320–322 (2010).

- [203] T. Čižmár, M. Mazilu, and K. Dholakia, "In situ wavefront correction and its application to micromanipulation," *Nature Photon.* **4**, 388–394 (2010).
- [204] B. Richards and E. Wolf, "Electromagnetic diffraction in optical systems II. Structure of the image field in an aplanatic system," *Proc. R. Soc. A* **253**, 358–379 (1959).
- [205] Q. Zhan, "Cylindrical vector beams: from mathematical concepts to applications," *Adv. Opt. Photon.* **1**, 1–57 (2009).
- [206] Q. Zhan, "Trapping metallic Rayleigh particles with radial polarization," *Opt. Express* **12**, 3377–3382 (2004).
- [207] O. M. Wilson, X. Hu, D. G. Cahill, and P. V. Braun, "Colloidal metal particles as probes of nanoscale thermal transport in fluids," *Phys. Rev. B* **66**, 224301 (2002).
- [208] Z. Ge, Y. Kang, A. Taton, P. V. Braun, and D. G. Cahill, "Thermal transport in Au-core polymer-shell nanoparticles," *Nano Lett.* **5**, 531–535 (2005).
- [209] S. Merabia, P. Keblinski, L. Joly, L. J. Lewis, and J. L. Barrat, "Critical heat flux around strongly heated nanoparticles," *Phys. Rev. E* **79**, 021404 (2009).
- [210] J. Alper and K. Hamad-Schifferli, "Effect of ligands on thermal dissipation from gold nanorods," *Langmuir* **26**, 3786–3789 (2010).
- [211] V. Kotaidis and A. Plech, "Cavitation dynamics on the nanoscale," *App. Phys. Lett.* **87**, 213102 (2005).
- [212] D. Lapotko, "Optical excitation and detection of vapor bubbles around plasmonic nanoparticles," *Opt. Express* **4**, 2538–2556 (2009).
- [213] D. Lapotko, E. Lukianova, M. Potapnev, O. Aleinikova, and A. Oraevsky, "Method of laser activated nano-thermolysis for elimination of tumor cells," *Cancer Lett.* **239**, 36–45 (2006).
- [214] M. Haruta, N. Yamada, T. Kobayashi, and I. S., "Gold catalysts prepared by coprecipitation for low-temperature oxidation of hydrogen and of carbon monoxide," *J. Catal.* **115**, 301–309 (1989).

BIBLIOGRAPHY

- [215] M. Haruta, "Gold as a novel catalyst in the 21st century: preparation, working mechanism and applications," *Gold. Bull.* **37**, 27–36 (2004).
- [216] R. M. Crooks, M. Zhao, L. Sun, V. Chechik, and L. K. Yeung, "Dendrimer-encapsulated metal nanoparticles: synthesis, characterization, and applications to catalysis," *Acc. Chem. Res.* **34**, 181–190 (2001).
- [217] M. M. Tirado, C. L. Martínez, and J. G. de la Torre, "Comparison of theories for the translational and rotational diffusion coefficients of rod-like macromolecules. Application to short DNA fragments," *J. Chem. Phys.* **81**, 2047 (1984).
- [218] NIST, "Nist Chemistry Webbook," <http://webbook.nist.gov/chemistry/fluid/>.
- [219] C. T. O'Konski, K. Yoshioka, and W. H. Orrtung, "Electric properties of macromolecules. IV. Determination of electric and optical parameters from saturation of electric birefringence in solution," *J. Phys. Chem.* **63**, 1558 (1959).
- [220] G. E. Uhlenbeck and L. Ornstein, "On the theory of Brownian motion," *Phys. Rev.* **36**, 823–841 (1930).
- [221] M. C. Wang and G. E. Uhlenbeck, "On the theory of the Brownian motion II," *Rev. Mod. Phys.* **17**, 323–342 (1945).
- [222] L. Edman, "Theory of fluorescence correlation spectroscopy on single molecules," *J. Phys. Chem. A* **104**, 6165 – 6170 (2000).
- [223] J. H. Lienhard IV and J. H. Lienhard V, *A heat transfer textbook* (Phlogiston Press, Cambridge, Massachusetts, 2008).
- [224] J. A. Stratton, *Electromagnetic theory* (McGraw-Hill Book company Inc., 1941).
- [225] F. Perrin, "Mouvement brownien d'un ellipsoïde (II). Rotation libre et dépolarisation des fluorescences. Translation et diffusion de molécules ellipsoïdales," *J. Phys. Radium* **VII**, 1–11 (1936).

Samenvatting

Optische manipulatie en studie van individuele gouden nanodeeltjes in oplossing

In dit proefschrift onderzoeken we gouden nanodeeltjes gevat in een optisch pincet, zowel als een nieuwe benadering om individuele nanodeeltjes te bestuderen in oplossing, als een methode om de deeltjes te gebruiken als een ultra-klein stuk gereedschap voor mechanische manipulatie op nanometer schaal.

Inleiding

Gouden nanodeeltjes – Gouden nanodeeltjes zijn kleine stukjes goud met afmetingen van ongeveer 1 tot 100 nanometer. Deze nanodeeltjes hebben een aantal bijzondere eigenschappen die ze tot interessante objecten maakt voor zowel fundamenteel onderzoek als voor een breed scala aan praktische toepassingen.

In de eerste plaats hebben gouden nanodeeltjes speciale optische eigenschappen. Licht brengt de vrije elektronen in het metalen deeltje in trilling, als een gezamenlijke oscillatie van de electronenwolk ten opzichte van de positieve atoomkernen. Deze oscillatie is bijzonder sterk voor bepaalde golflengtes, de plasmon resonanties van het deeltje. De golflengte van deze resonantie hangt af van de vorm en grootte van de deeltjes, en van de brekingsindex van de omgeving. Voor bolvormige gouddeeltjes in water of glas ligt de resonantie rond de golflengte van groen licht. Door sterke absorptie bij deze golflengtes verkrijgen oplossingen van deze deeltjes een karakteristieke rode kleur. De sterke absorptie en verstrooiing van licht door gouden nanodeeltjes wordt bijvoorbeeld veel gebruikt in biochemisch onderzoek, waar gouddeeltjes specifiek worden bevestigd aan bepaalde die eiwitten zo op een

eenvoudige manier waargenomen kunnen worden. Voor gouden nanostaafjes kan de resonantie golflengte helemaal naar de golflengte van infra-rood licht verschoven worden door de lengte-breedte verhouding aan te passen. Deze eigenschap kan worden gebruikt om staafjes te kiezen die een optimale golflengte hebben voor de beschikbare lichtbronnen, of het beste voldoen aan andere randvoorwaarden in een experiment. De gevoeligheid van de resonantie voor de brekingsindex van de omgeving kan bijvoorbeeld worden gebruikt om lokaal de brekingsindex in een materiaal te meten.

Vanwege hun kleine afmetingen hebben nanodeeltjes een zeer hoge oppervlakte-volume verhouding. Daarnaast kunnen deeltjes gemaakt worden met specifieke kristalvlakken. Samen met de chemische stabiliteit van goud maakt dit dat gouden nanodeeltjes bijvoorbeeld kunnen worden gebruikt als efficiënte katalysatoren voor chemische reacties. Hoewel het proces van katalyse zelf niets met licht te maken heeft, kunnen katalytische processen wel met optische technieken bestudeerd worden, via de gevoeligheid van de optische eigenschappen van het deeltje voor een verandering van vorm, grootte of omgeving. Dit intieme samenspel van deeltjes-geometrie en optische eigenschappen biedt veel toepassingsmogelijkheden.

Individuele deeltjes en ensembles – Een groot deel van de studies aan gouden nanodeeltjes wordt gedaan aan suspensies van nanodeeltjes in een oplossing. De onderliggende reden voor deze populariteit is dat suspensies de basis vormen van tal van experimenten, en dat met eenvoudige optische apparatuur –aanwezig in vrijwel ieder natuurkundig, scheikundig of biologisch laboratorium– veel informatie verkregen kan worden.

Sinds het begin van deze eeuw is het mogelijk geworden om individuele metalen nanodeeltjes te bestuderen in een optische microscoop. De meerwaarde van studies aan individuele deeltjes vindt zijn oorsprong in het feit dat geen twee nanodeeltjes gelijk zijn. In suspensies hebben de deeltjes altijd een iets onderling verschillende vorm en grootte, hoe zorgvuldig men de synthese-reacties ook heeft kunnen controleren. Omdat de eigenschappen van de deeltjes sterk afhangen van hun vorm en grootte, ziet men in experimenten aan ensembles van deeltjes altijd een gemiddelde waarde van de eigenschappen van de deeltjes.

In studies van individuele deeltjes kunnen verschillende eigenschappen aan hetzelfde deeltje gemeten worden, en kan men direct de correlatie tussen deze eigenschappen bepalen. Ook kan men bestuderen hoe de eigenschappen van een deeltje van een bepaalde vorm en grootte worden beïnvloed door externe verstoringen, zonder de noodzaak om processen te synchroni-

seren voor een groot aantal deeltjes. Deze eigenschap is bijzonder waardevol voor de studie van processen die intrinsiek willekeurig zijn. Ook kunnen individuele deeltjes worden toegepast om zeer lokaal de eigenschappen van inhomogene materialen te onderzoeken.

In de laatste jaren zijn er veel ontdekkingen gedaan aan, of met behulp van, deze individuele gouden nanodeeltjes. Om processen op het deeltje als functie van tijd te kunnen volgen, is het noodzakelijk dat het lang genoeg in het focus van een microscoop objectief verblijft. Tot nu toe is in de meeste experimenten aan individuele deeltjes aan deze voorwaarde voldaan door de gouddeeltjes te deponeren op een microscoopglasje, waar ze vast blijven plakken. Hoewel in deze geometrie interessante ontdekkingen zijn gedaan, geeft de nabijheid van het glasoppervlak ook een verstoring, die de interpretatie van de experimentele resultaten en vergelijking met theorie bemoeilijkt.

In oplossing is studie aan individuele deeltjes veel moeilijker; door de Brownse beweging diffundeert het nanodeeltje uit het focus, meestal op een tijdschaal in de orde van milliseconden. Deze tijdschaal is te kort om veel interessante processen te kunnen volgen.

Objecten vasthouden in het focus van een lichtbundel – Licht heeft impuls, en kan dit overdragen op materie. In het dagelijks leven merken we niet veel van de krachten die licht uitoefent, omdat het impuls per foton maar heel klein is. Met de hoge licht intensiteiten zoals die met lasers bereikt kunnen worden, kunnen echter gemakkelijk microscopische objecten bijvoorbeeld tegen de zwaartekracht omhooggehouden worden. In een gefocusseerde laserbundel kunnen deeltjes –afhankelijk van hun eigenschappen– naar het focus toe worden getrokken of daarvan worden afgestoten. In het eerste geval kunnen objecten in het focus van een lichtbundel worden vastgehouden, en deze techniek is dan ook bekend onder de naam ‘optisch pincet’.

Ook metalen nanodeeltjes kunnen worden gevangen met een optisch pincet. Omdat metalen een sterkere wisselwerking met licht hebben dan diëlektrische materialen, kunnen de gouden nanodeeltjes worden gevangen tot veel kleinere afmetingen, tot aan enkele tientallen nanometers in diameter.

Het optisch vangen van gouddeeltjes is al in 1994 voor het eerst gedemonstreerd. Sinds die tijd zijn er wel vorderingen geboekt, maar behalve demonstraties van het stabiel vangen van metalen nanodeeltjes van verschillende grootte en vorm hebben de gevangen gouden deeltjes niet echt bijgedragen aan grote wetenschappelijke doorbraken.

Een gouddeeltje in een optische val: een nieuwe benadering om enkele deeltjes te bestuderen in oplossing

Hierboven hebben we beargumenteerd dat het nuttig is om nanodeeltjes stuk voor stuk te bestuderen. Daarnaast is het nuttig om experimenten in oplossing te verrichten, met gouden nanodeeltjes in een homogene vloeistof omgeving. In dit proefschrift onderzoeken we een nieuwe experimentele benadering om deze beide eisen te combineren, door gebruik te maken van een optische val. We laten zien dat op deze manier enkele deeltjes gedurende vrijwel onbeperkt lange tijden (we hebben experimenten van enkele uren op hetzelfde deeltje uitgevoerd) kunnen worden bestudeerd in de oplossing.

Een gouddeeltje in een optische val: een nieuw gereedschap voor het uitvoeren van mechanische manipulaties op nanometerschaal

Een tweede motivatie voor het gebruik van de optische val is het mogelijk toepassen van de gouden nanodeeltjes als een zeer klein stuk mechanisch gereedschap om krachten en momenten uit te oefenen op nanometerschaal. De krachten die op gouddeeltjes kunnen worden uitgeoefend met een lichtbundel zijn niet bijzonder groot, in de orde van enkele piconewtons. Echter, deze krachten zijn precies in het juiste bereik om een belangrijke klasse van individuele (bio-)moleculen en andere zachte (biologische) materie te vervormen, en op die manier hun mechanische eigenschappen te bepalen. Aangezien de werking van de biomoleculen in belangrijke mate bepaald wordt door hun mechanische eigenschappen, kan een directe meting van hun mechanische eigenschappen veel waardevolle informatie opleveren.

In de laatste 20 jaar zijn er veel studies aan individuele biomoleculen verricht met behulp van het optisch pincet. Deze studies zijn dan uitgevoerd met glazen of plastic bolletjes in de val, en zijn verricht aan individuele moleculen in een bufferoplossing. De meest gebruikte bolletjes zijn groter dan 1 micrometer in diameter. Het kleine formaat van de optisch gevangen gouddeeltjes levert mogelijk nieuwe toepassingen, in systemen waar beperkte ruimte is. Een voorbeeld van zo'n systeem is een levende cel, typisch enkele tot enkele tientallen micrometers groot. Een cel zit boordevol met verschillende onderdelen, en om die te kunnen onderzoeken moet het stuk gereedschap klein genoeg zijn. De gouden nanodeeltjes maken het wellicht mogelijk om me-

chanische metingen te verrichten aan individuele macro-moleculen in hun natuurlijke omgeving, de levende cel.

Resultaten uit dit proefschrift

De belangrijkste resultaten beschreven in dit proefschrift kunnen als volgt worden samengevat.

1. De signaal-ruis-verhouding in foto-thermische detectie van absorberende nano-objecten kan worden verhoogd door een juiste keuze van het medium rond het deeltje, het gebruik van een detectie laser met een golflengte buiten het absorptie spectrum van het deeltje en een zo hoog mogelijke intensiteit, en thermische isolatie van het nano-object ten opzichte van het substraat.

In hoofdstuk 2 van dit proefschrift beschrijven we hoe we de gevoeligheid kunnen verbeteren van een methode om individuele gouddeeltjes te detecteren. In de methode detecteren wij de warmte die in de omgeving van het deeltje wordt gedissipeerd als gevolg van de absorptie van licht, via detectie van een veranderde brekingsindex van de omgeving van het deeltje. In de methode worden twee laserbundels gebruikt; één bundel wordt geabsorbeerd door het deeltje, en wordt gemoduleerd in intensiteit zodat een periodiek warmteprofiel ontstaat rond het deeltje. De transmissie of reflectie van een tweede laser die gefocuseerd wordt op het deeltje verandert periodiek een heel klein beetje. Via lock-in detectietechnieken kan deze verandering worden gedetecteerd. In het hoofdstuk laten we zien dat de signaal-ruis-verhouding van deze meetmethode op drie manieren kan worden vergroot: i) de golflengte van de detectie laser kan worden gekozen in een bereik waar het sample niet absorbeert. Een gevolg van deze keuze is dat de intensiteit van de bundel vrijwel onbeperkt groot kan worden gemaakt. Hiermee wordt de relatieve bijdrage van de hagelruis als gevolg van het deeltjeskarakter van licht verminderd; ii) de vloeistof rond het deeltje kan worden gekozen op basis van een zo groot mogelijke brekingsindex, een zo groot mogelijke verandering van de brekingsindex bij verandering van de temperatuur, en een zo laag mogelijke warmtecapaciteit; iii) het te detecteren deeltje kan thermisch worden geïsoleerd van het glasoppervlak, zodat een zo groot mogelijk deel van de geabsorbeerde warmte terecht komt in de vloeistof, waar de verandering van temperatuur het meest gevoelig gedetecteerd kan worden.

De resultaten in hoofdstuk 2 zijn verkregen aan individuele gouddeeltjes die zijn neergelegd op een glasoppervlak. Daarmee lijken deze resultaten niet direct gerelateerd aan het thema van dit proefschrift, het bestuderen van enkele gouden deeltjes vrij in oplossing. Echter, aanwezigheid van een glasoppervlak is geen noodzakelijke voorwaarde van deze meetmethode, en deze methode kan met een aangepaste geometrie direct worden toegepast voor detectie van deeltjes in oplossing. Daarmee is deze methode een veelbelovend alternatief voor de detectie-methoden zoals we die in de rest van het proefschrift gebruiken. Een interessant aspect is dat we voor deeltjes in oplossing optimaal gebruik kunnen maken van de grote foto-thermische gevoeligheid van vloeistoffen, omdat alle warmte bijdraagt aan het signaal.

2. Goudstaafjes in een optische val kunnen dienen als ultra-kleine overdragers van krachten en momenten, die groot genoeg zijn om relevante (bio-)moleculen te vervormen

In hoofdstuk 4 van dit proefschrift laten we zien dat op goudstaafjes van 25 nanometer diameter and 60 nanometer lengte een optisch moment (koppel) kan worden uitgeoefend van rond de 100 piconewton nanometer, in het juiste bereik om relevante biomoleculen –zoals bijvoorbeeld een DNA molecuul–mechanisch te kunnen vervormen.

Het optische moment op de goudstaafjes lijnt de staafjes uit met hun lange as langs de polarisatie van laser die de optische val vormt. Via metingen aan de resterende Brownse bewegingen van het gevangen deeltje rondom de evenwichtsoriëntatie waren we in staat om dit optische moment nauwkeurig te bepalen. Bovendien konden we uit de schaling van het gemeten moment als functie van het vermogen van de laser een nauwkeurige schatting maken van de temperatuur van de gouddeeltjes in de optische val.

Naast optische momenten worden op de staafjes ook optische krachten uitgeoefend. Dit zijn precies de krachten die het deeltje 'vangen' en dwingen om een bepaalde positie in het focus van de laserbundel aan te nemen en naar terug te keren, als het deeltje van deze positie vandaan bewogen wordt. Een nieuw aspect van de optisch gevangen goudstaafjes zoals beschreven in dit proefschrift is dat ze het mogelijk maken zowel momenten als krachten uit te oefenen met hetzelfde object, en dat dit object bijzonder klein is. Dit kleine formaat biedt wellicht mogelijkheden om de goudstaafjes te gebruiken als instrument in omgevingen waar de ruimte zeer beperkt is. Een spannend voorbeeld van zo'n omgeving is een levende cel.

3. De translationele and rotationele Brownse beweging van een heet nanodeeltje worden beschreven door verschillende effectieve temperaturen.

De studie van de optische krachten en momenten in Hoofdstuk 4 leverde verrassende vindingen op over de Brownse beweging van een nanodeeltje met een hogere temperatuur dan zijn omgeving.

De resultaten verkregen uit de enkele gouden nanostaafjes in de optische val vormden een experimentele bevestiging van een recent ontwikkelde theorie voor de translationele diffusie van een heet deeltje, door theoretisch natuurkundigen uit Leipzig. Deze theorie voorspelt dat de translationele beweging beschreven kan worden met een temperatuur dicht bij het gemiddelde van de deeltjestemperatuur en de omgevingstemperatuur.

Daarnaast laten onze experimenten zien dat de rotationele diffusie van het deeltje beschreven moet worden met een hogere temperatuur, dichterbij van de oppervlaktetemperatuur van het deeltje. Hoewel wij in hoofdstuk 4 enkele mogelijke verklaringen voor dit effect hebben geopperd, begrepen wij nog niet precies waarom dit het geval was. Na publicatie van onze experiment zijn collega's uit Leipzig direct aan de slag gegaan om onze verrassende resultaten te begrijpen. Zeer recent is er voor onze experimentele bevindingen een volledig analytisch uitgewerkte theorie ontwikkeld, die laat zien dat ons resultaat inderdaad heel algemeen geldt voor de Brownse beweging, voor zowel bolvormige deeltjes als staafjes. De reden dat de rotationele beweging beschreven moet worden door een andere temperatuur dan de translationele beweging is dat het snelheidsprofiel van de vloeistof rondom het deeltje verschillend is voor de beide bewegingen. Het snelheidsprofiel bij de rotationele beweging valt ruimtelijk sneller af dan voor translationele beweging, en is gevoelig voor de eigenschappen van de vloeistof dicht bij het deeltje. Omdat dicht bij het deeltje de temperatuur hoger is, is de effectieve temperatuur voor rotationele beweging hoger.

4. De demping van mechanische trillingen van gouden nanodeeltjes wordt bepaald zowel door afstraling van trillingen naar de omgeving als door interne dissipatie in het nanodeeltje

In hoofdstuk 6 beschrijven we hoe we met zeer korte optische pulsen een akoestische trilling kunnen aanslaan en detecteren in een enkel gouden nanodeeltje dat gevangen is in een optische val in water.

Een verrassend resultaat van dit experiment is dat de trillingen van het

deeltje relatief snel gedempt worden, twee- tot driemaal sneller dan op basis van de gangbare theorie voorspeld werd. Daarnaast namen we een grote spreiding waar in de dempingstijden van verschillende individuele deeltjes uit hetzelfde monster. Dit was een onverwacht resultaat, omdat de deeltjes zich allemaal in precies dezelfde omgeving bevonden, volledig omgeven door water, en allemaal dezelfde uitdovingstijd zouden moeten vertonen. Ons resultaat was dus verrassend, maar we merkten op dat de theorie voor demping van trillingen in het geval van nanodeeltjes eigenlijk nog nooit goed getest was. Onze resultaten vormden de eerste directe metingen van de uitdovingstijd van deze trillingen, en daarmee de eerste goede test van de theorie.

Tot op heden werd het overgrote deel van studies van deze trillingen verricht in metingen waar een zeer groot aantal deeltjes tegelijkertijd bestudeerd werd. In dit soort metingen wordt de gemeten dempingstijd gedomineerd door het uit fase raken van de trillingen van een groot aantal deeltjes dat trilt met iets verschillende frequenties, als gevolg van de onvermijdelijke spreiding van grootte and vorm van de deeltjes in het monster. De uitdovingstijd van de trilling van een enkel deeltje is daardoor niet goed meetbaar.

Sinds enkele jaren is het mogelijk om de trillingen te bestuderen aan individuele deeltjes, waar de uitdovingstijd wel direct gemeten kan worden, en een werkelijke maat is voor het verlies van trillingsenergie naar de omgeving. Echter, deze metingen zijn voorheen verricht aan nanodeeltjes die zijn gedeponneerd op een glazen oppervlak. In deze geometrie is de demping van de trillingen door straling naar de omgeving moeilijk te quantificeren, omdat ze kan afhangen van de exacte geometrie van het contactoppervlak tussen het nanodeeltje en het substraat, iets wat zeer lastig te meten en theoretisch te modelleren is.

In dit proefschrift konden we voor het eerst de trillingen bestuderen van een enkel nanodeeltje in een homogene omgeving, en de resultaten met theorie vergelijken. Aangezien de gemeten dempingstijd veel korter is dan de theorie voorspelde, moeten we concluderen dat de trillingen niet alleen gedempt worden door verlies van trillingsenergie naar de omgeving. Nu denken we dat interne dissipatiemechanismen in het metaal een belangrijke bijdrage aan de demping leveren. Achteraf gezien is de demping van trillingen in het metaal misschien niet zo verwonderlijk. Voor metalen op macroscopische schaal is veel onderzoek gedaan naar de mechanismen van demping van akoestische trillingen, omdat hieruit veel informatie over het materiaal verkregen kan worden. In het bijzonder is bekend dat bij kamertemperatuur en daarboven en bij trillingsfrequenties van enkele tientallen GHz de demping

zeer hoog is, zo hoog dat deze zeer moeilijk te bepalen is. Onze metingen aan de nanodeeltjes bieden een mogelijkheid om deze dissipatiemechanismen op nanoschaal te onderzoeken.

Onze huidige hypothese is dat defecten in het kristalrooster van goud een belangrijke bijdrage leveren aan de demping van de trillingen. Verschillen in kristalstructuur en het aantal defecten per deeltje zouden de gemeten spreiding van de dempingstijden kunnen verklaren.

Curriculum Vitae

of Paul Victor Ruijgrok, born in Ubbergen (The Netherlands) on February 8, 1981.

From 1995 to 1999 I obtained my secondary education at the Karel de Grote College in Nijmegen. In 2000 I obtained my pre-university degree from the Regionaal Opleidingen Centrum (ROC) in Nijmegen. After a year of traveling and voluntary work in South-East Asia, I started the study of Aerospace Engineering at Delft University of Technology in September 2001. After one year, I switched fields and enrolled at Leiden University to study physics. At the end of my Bachelor studies I performed a junior research project in the group of Prof. Joost W. M. Frenken; I conducted an analysis of the role of surface stress on the thermal stability of vacancy islands on a metal surface, based on scanning tunneling microscopy measurements on Cu [100]. I obtained my Bachelor degree in Physics in February 2006.

During my MSc study at Leiden University, I was selected to attend the CERN summer student program on elementary particle physics in 2006 in Geneva (Switzerland). In Leiden, I did a MSc project in the group of Prof. Michel Orrit, where I used an ultra-fast optical pump-probe technique to study the melting transition of single gold nanoparticles. I also carried out a MSc project in the group of Prof. Vahid Sandoghdar at the Eidgenössische Technische Hochschule (ETH) in Zürich (Switzerland), where I measured the fluorescence decay rate of nitrogen-vacancy centers in single diamond nanocrystals to probe the local photonic structure in strongly scattering random media. In December 2007 I obtained my MSc diploma in Physics with distinction (*cum laude*) at Leiden University. In January and February 2008 I worked at the ETH Zürich to continue the work of my MSc research project theme.

In March 2008 I started a PhD project at the Leiden Institute of Physics

in the group of Prof. Michel Orrit, on the optical trapping of single gold nanoparticles. The results obtained during the following four years are described in this thesis. During the PhD project, I contributed to the teaching at the Physics Department by assisting with the first year Physics laboratory course and with a first year course on Optics. I also supervised a MSc student project, organized the regular bi-weekly seminars of the Biological and Molecular Physics section, and was a member of the Institute council. I presented my work at several summer schools and international conferences. For the poster presentation at the Nanometa conference on Nanophotonics and Metamaterials in Seefeld (Austria) in 2011 I received a best poster prize.

From June 2012 onward, I will work as a postdoctoral researcher in the group of Prof. Zev Bryant at Stanford University in the United States of America.

List of Publications

1. A. L. Tchebotareva, M. A. van Dijk, P. V. Ruijgrok, V. Fokkema, M. H. S.Hesselberth, M. Lippitz, and M. Orrit,
“Acoustic and Optical Modes of Single Dumbbells of Gold Nanoparticles”,
Chem. Phys. Chem. **10**, 111–114 (2009).
2. P. V. Ruijgrok, R. Wüest, A. A. Rebane, A. Renn, and V. Sandoghdar,
“Spontaneous emission of a nanoscopic emitter in a strongly scattering disordered medium”,
Opt. Express **18**, 6360–6365 (2010).
3. A. L. Tchebotareva, P. V. Ruijgrok, P. Zijlstra, and M. Orrit,
“Probing the acoustic vibrations of single metal nanoparticles by ultra-short laser pulses”,
Laser Photonics Rev. **4**, 581–597 (2010).
4. A. Gaiduk, P. V. Ruijgrok, M. Yorulmaz and M. Orrit,
“Detection limits in photothermal microscopy”,
Chem. Sci. **1**, 343-350 (2010).
Chapter 2 of this thesis
5. A. Gaiduk, M. Yorulmaz, P. V. Ruijgrok and M. Orrit,
“Room-temperature detection of a single molecule’s absorption by photothermal contrast”,
Science **330**, 353–356 (2010).

6. A. Gaiduk, P. V. Ruijgrok, M. Yorulmaz, and M. Orrit,
“Making gold nanoparticles fluorescent for simultaneous absorption and fluorescence detection on the single particle level”,
Phys. Chem. Chem. Phys. **13**, 149-153 (2011).
7. P. V. Ruijgrok, N. R. Verhart, P. Zijlstra, A. L. Tchebotareva and M. Orrit,
“Brownian fluctuations and heating of an optically aligned gold nanorod”,
Phys. Rev. Lett. **107**, 037401 (2011).
Chapter 4 of this thesis
8. P. V. Ruijgrok, P. Zijlstra, A. L. Tchebotareva and M. Orrit,
“Damping of acoustic vibrations of single gold nanoparticles optically trapped in water”,
Nano Lett. **12**, 1063–1069 (2012).
Chapter 6 of this thesis
9. P. V. Ruijgrok, et al. ,
“Optical trapping of single gold nanorods: manipulating forces, torques and heat on the nanoscale”,
in preparation for publication,
based on Chapter 3 of this thesis.
10. P. V. Ruijgrok, et al.,
“On the temperature dependence of the plasmon width and its use to measure the temperature of a single gold nanoparticle”,
in preparation for publication,
based on Chapter 5 of this thesis.

Acknowledgments

Although the cover on this thesis bears only my name, many people have contributed to the work in this thesis. I gladly acknowledge their contributions here.

Without high-quality technical support most science would never be brought to a successful end. I am grateful to Harmen van der Meer, who designed and constructed the optical microscope and essential mechanical components of the experimental setup, and to Mirthe Bergman, who fabricated structures in glass coverslips, essential parts in one of several projects that I have regrettably not yet been able to bring to completion. Jos Disselhorst taught me some of the craftsmanship in the making of fine-mechanical instruments and, in doing so, made many small technical improvements to the experimental setup and the temperature-controlled sample chamber of Chapter 5. I thank Arno van Amersfoort, Raymond Koehler, Ruud Kuyvenhoven, René Overgaw, Ton Tampung, Peter van Veldhuizen, for their contributions to the electronic parts of the experimental setup, and the maintenance of the computers and computer network. I am grateful to Henriëtte van Leeuwen, for her swift and adequate support in all administrative matters.

During my PhD I have had the pleasure of working together with three postdoctoral researchers, dr. Anna L. Tchegotareva, dr. Alexander Gaiduk and dr. Peter Zijlstra. They have contributed greatly to shaping this thesis. I thank Prof. Lene B. Oddershede for a very valuable visit to her lab in Copenhagen at the start of the PhD project, and her continued support and advice. I am indebted to Nico Verhart, whose work during his MSc project has greatly contributed to Chapter 4.

